Chapter 6

Results for Oscillating Cylinder

6.1 Introduction

The purpose of the experiments conducted with forced cylinder oscillation was to examine the influence of imposed cross flow motion on the lift forces which acted on the cylinder. There is evidence that imposed motion, below the amplitude required for lock-in, can still affect lift forces. As was pointed out in chapter 1, comparatively low amplitudes of motion ($\alpha < 5\%$) are important from the point of view of structural design, since strength considerations determine that structural oscillations must generally be restricted to low amplitudes.

The objectives were to see if imposition of motion affected lift force, and to examine the characteristics both of forces which were correlated with cylinder motion and those which were not. Before the tests were conducted, it was thought that cylinder oscillation might be able to re-establish vortex shedding in the supercritical regime, at least in the smooth flow and for the lower turbulence intensities (configs. 1 & 2). This possibility was suggested by the tests conducted by Wootton (1968, 1969), who deduced the re-establishment of vortex shedding with $St \simeq 0.21$ on a model of a lightly-damped circular stack in smooth supercritical flow, as discussed in § 1.4.1.

In most previous experiments in which motion-correlated forces have been investigated, the characteristics of the residual forces after the removal of motion correlated forces have not been studied. As an underlying assumption of one of the major models for prediction of the amplitude of structural vibration response is that the residual forces are independent of motion-correlated forces, this investigation is obviously important. In addition, the characteristics of lift forces which act on an oscillating cylinder in smooth subcritical flow were examined in an effort to understand the physical processes involved.

In general terms, the imposition of cylinder oscillation did not produce marked changes in the values of σ_{C_l}, and the spectra of lift were very similar to those observed for the case of the stationary cylinder, except that small spectral peaks were observed at the frequency of cylinder oscillation, indicating that some proportion of lift force was correlated with cylinder motion.

The outline of the chapter is as follows. After commencing with an explanation of

the range of experimental parameters which were examined, the computation of motion-correlated forces and force coefficients is discussed. The general characteristics of lift forces with imposed cross flow motion are examined, and it is shown by comparison with results recorded with the cylinder fixed that the portion of lift forces which were uncorrelated with motion were little affected by imposition of motion. Next, force coefficients derived from motion-correlated forces are presented and discussed. Finally, attention is given to a detailed examination of the characteristics of lift forces on the cylinder oscillating in smooth subcritical flows, since these provided the clearest indication of the influence of cylinder motion on lift.

6.2 Range of Parameters

In this set of tests, the cylinder was forced to oscillate cross flow, and lift forces acting on the six transducer stations were measured. In addition to the dimensionless groups Re, I_u and LSR relevant to the study of the fixed cylinder, two more arise as a consequence of the oscillation; the dimensionless amplitude $\alpha = y/D$ and the reduced velocity $V_r = U/fD$.

The way in which the equipment was designed meant that it was possible to vary the Reynolds number and reduced velocity independently, by fixing the flow speed and adjusting the oscillation frequency. In order to reduce the number of experimental variables to manageable proportions, it was decided to employ a restricted set of Reynolds numbers. Two Reynolds numbers at the extremes of the range of capability ($\simeq 1.5 \times 10^5$ and $\simeq 5 \times 10^5$) were employed. This meant that data could be obtained for the smooth subcritical flows, enabling comparison with other experimental data, while at higher Reynolds numbers and turbulence intensities, interaction with re-established vortex shedding could be studied. Also, it was of interest to see if imposition of motion could re-establish vortex shedding in low turbulence supercritical flows, as mentioned in § 6.1.

The maximum amplitude of oscillation was determined by the capability of the electromagnetic shaker which had a maximum stroke of ±6 mm, giving $\alpha_{\max} = 6/200 = 3\%$. Accordingly, it was decided to carry out investigations for three amplitudes: nominally $\alpha = 1\%$, 2% and 3%. However, due to limitations in the force capacity of the electromagnetic shaker, it was not always possible to achieve the 3% amplitude at high frequencies ($\sim$ 50 Hz) and consequently only results for $\alpha_{\text{nom}} = 1\%$ and 2% are presented for the higher Reynolds numbers.

Approximately nine different frequencies (values of V_r) were used for each Re–α–flow configuration combination. The turbulence configurations introduced in chapter 3 and used in chapter 5 were retained.

6.3 Computation of Motion-Correlated Forces

The first section of results to be described here are concerned with motion-correlated forces, and the decomposition of lift force into components correlated with cylinder

acceleration and velocity, together with residual, uncorrelated force. As pointed out in chapter 1, there are several ways of computing motion-correlated forces, all essentially equivalent. The approach adopted here was to compute forces correlated with motion on a least-squares basis, using preprocessed timeseries of coefficient of lift, cylinder cross flow acceleration and velocity.

Note that while it was possible to compute the magnitude of forces correlated with motion, this does not imply the existence of deterministic forces, linearly related to the motion of the cylinder in each cycle of oscillation. In cases where both motion-correlated and uncorrelated forces occur, it seems unlikely that this can be due to a summation of a deterministic and a random, uncorrelated force, as proposed for example by Basu (1982) and Vickery and Basu (1983 a, 1983 b, 1983 c). Since the forces are caused by discrete events—formation and shedding of vortices—it is more likely that sometimes vortices are correlated with motion, and sometimes not. This kind of shedding has been observed by Stansby (1976) and (albeit in shear flow) by Woo, Peterka and Cermak (1983, see § 1.4.1). Despite this, magnitudes of long-time-average motion-correlated forces indicate the degree to which imposed cylinder motion is able to re-organize vortex shedding. From the structural designer's viewpoint, velocity-correlated forces in particular can give an indication of structural stability with regard to flow-induced oscillations.

6.3.1 Decomposition based on least-squares fitting

The lift forces measured at each cylinder transducer station were decomposed into components correlated with cylinder acceleration and cylinder velocity, leaving an uncorrelated residual. The basis of the decomposition was to assume a linear relationship between lift and cylinder acceleration or velocity.

For example, assume that the timeseries $C_l(k)$ and $\ddot{y}(k)$ of the zero-mean processes of lift coefficient $C_l(t)$ and cylinder acceleration $\ddot{y}(t)$ are available. Then, by assumption

$$C_l(k) = A\ddot{y}(k) + e(k) \,, \tag{6.1}$$

where $e(k)$ is the timeseries of the residual process (error) and A is a constant. Let $\mathcal{E}$ be the sum of squared errors over the N records of the timeseries:

$$\mathcal{E} = \sum_{i=1}^{N} e^2(i) = \sum_{i=1}^{N} [C_l(i) - A\ddot{y}(i)]^2 \,. \tag{6.2}$$

By the usual means of setting $\partial\mathcal{E}/\partial A = 0$,

$$A = \frac{\sum_{i=1}^{N} \ddot{y}(i) C_l(i)}{\sum_{i=1}^{N} \ddot{y}^2(i)} \,. \tag{6.3}$$

The magnitudes of the coefficient of lift correlated with cylinder acceleration, C_{la}, can then be computed. Say $\ddot{y}(t) = B\cos 2\pi ft$. Then $C_{la} = A \cdot B$ and an equivalent process $C_{la}(t)$ is

$$C_{la}(t) = A\ddot{y}(t) = AB\cos 2\pi ft \,. \tag{6.4}$$

In the actual computation, the standard deviation of the acceleration process was estimated, instead of directly fitting the coefficient B in $\ddot{y}(t) = B\cos 2\pi ft$, so that

$$C_{la} = A \cdot \sqrt{2} \cdot \sigma_{\ddot{y}} \; . \tag{6.5}$$

The same method as that just described was used to find the coefficient of lift correlated with cylinder velocity, C_{lv}. Since for a periodic motion the acceleration and velocity are not correlated with each other, the acceleration- and velocity-correlated lift processes are uncorrelated also. The residual lift C_{lr}

$$C_{lr}(k) = C_l(k) - C_{la}(k) - C_{lv}(k) \tag{6.6}$$

is uncorrelated with cylinder acceleration and velocity.

6.3.2 Examples of decomposition

As an adjunct to the computations of the coefficients C_{la} and C_{lv}, the timeseries of acceleration- and velocity-correlated coefficients of lift, $C_{la}(k)$ and $C_{lv}(k)$ were estimated and printed out, together with the timeseries of the residual coefficient of lift $C_{lr}(k)$. Two examples of this process are presented here.

Smooth subcritical flow

The first example is for a recording made in the nominally smooth flow ($I_u = 0.6\%$), at at Reynolds number of 1.6×10^5. The reduced velocity was 5.02, and the amplitude of oscillation 2.6% D. Figure 6.1 (a) shows a portion of the timeseries of coefficient of lift recorded from one of the cylinder transducers. The portion amounts to about one-twelfth of the total recording over which the analysis and correlations were performed. The timebase is in the dimensionless form tU/D. It is apparent that the flow was subcritical, since the time trace shows a narrow-band random characteristic.

In figure 6.1 (b), timeseries of acceleration- and velocity-correlated coefficients of lift are presented with the residual after they have been subtracted from the total lift coefficient trace of figure 6.1 (a). In this case, the acceleration-correlated forces were out of phase with acceleration, while the velocity-correlated forces were in phase with velocity. It is apparent that the motion-correlated forces were of a magnitude comparable to the residual forces, and that the acceleration- and velocity-correlated magnitudes were similar to one another. In fact, this particular result exhibited amongst the largest magnitude motion-correlated lift forces of the smooth subcritical flow results, and showed a slight shift of total lift force centre frequency, indicating lock-in.

High Reynolds number turbulent flow

This set of results was recorded at the other extreme of the Reynolds number–turbulence envelope, with Reynolds number of 4.7×10^5 and a turbulence intensity of 18% (config. 4). The reduced velocity was 4.58 and the oscillation amplitude was 2.9% D. The results shown in figure 6.2 correspond to those in figure 6.1. The timeseries of total lift

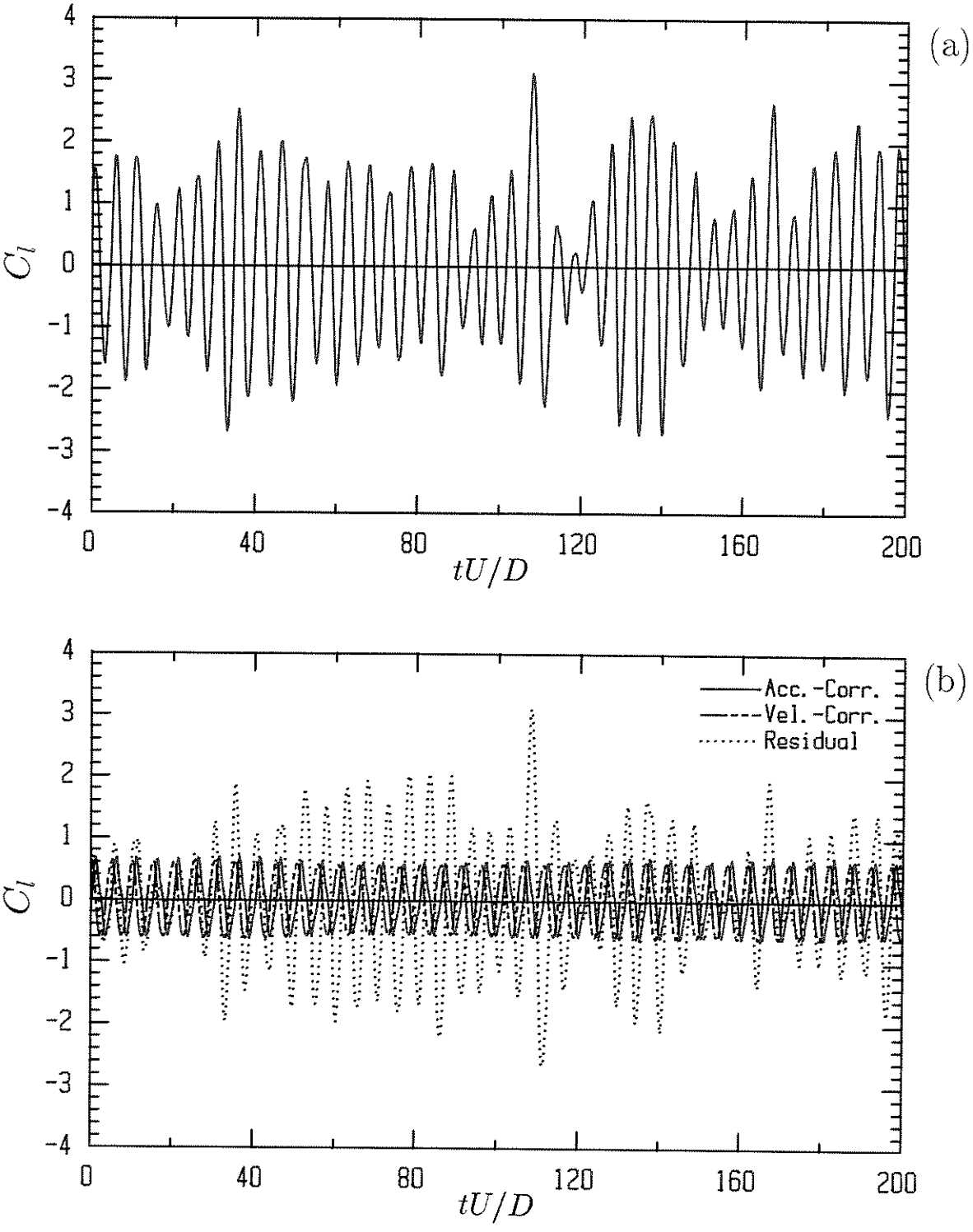

FIGURE 6.1: Timeseries of coefficient of lift measured at one transducer in smooth subcritical flow. (a) Total coefficient of lift. (b) Equivalent timeseries of acceleration- and velocity-correlated coefficients of lift with residual after subtraction from total lift.

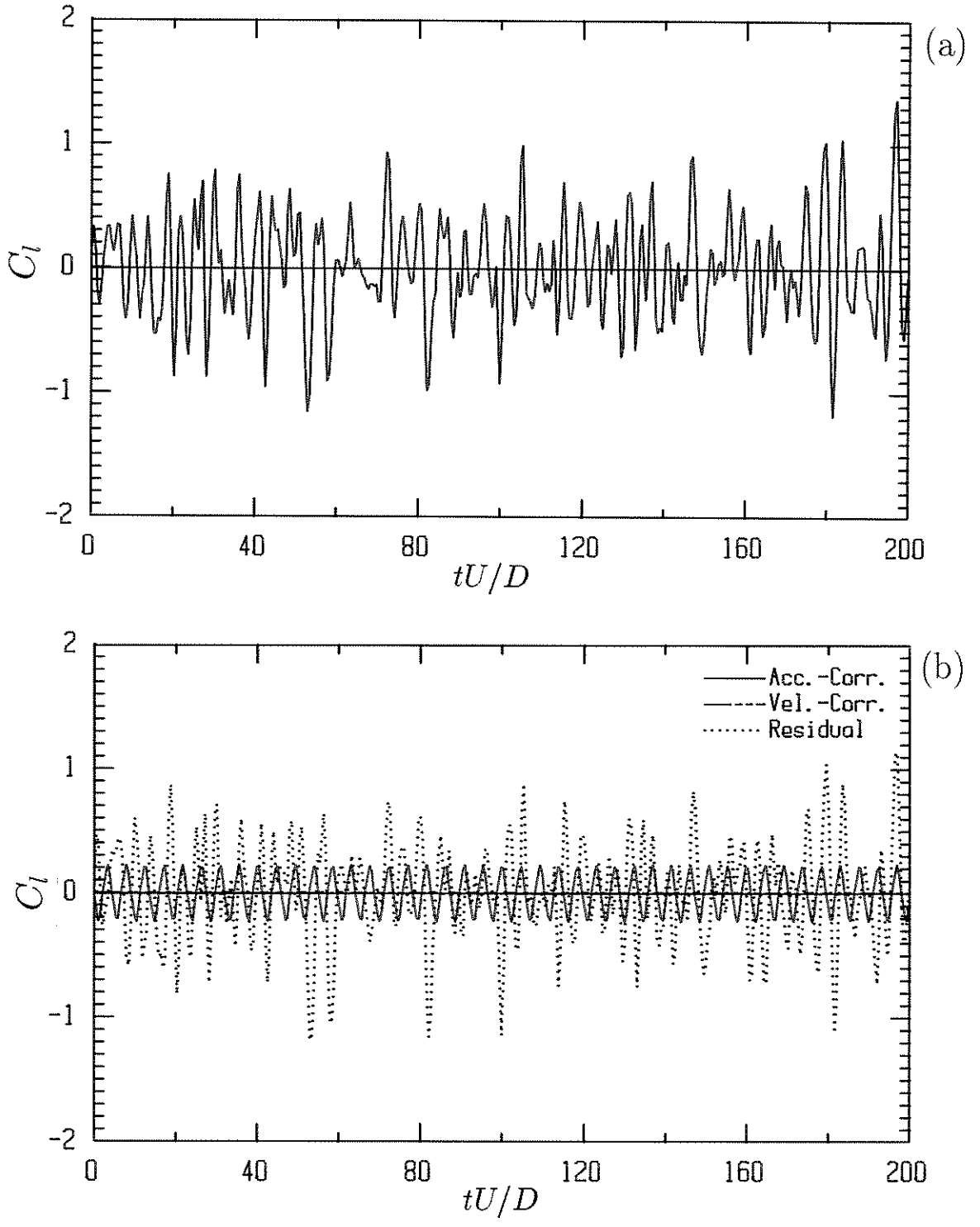

FIGURE 6.2: Timeseries of coefficient of lift measured at one transducer in supercritical turbulent flow ($Re = 4.7 \times 10^5$, turbulence config. 4, $I_u = 18\%$). (a) Total coefficient of lift. (b) Equivalent timeseries of acceleration- and velocity-correlated coefficients of lift with residual after subtraction form total lift.

coefficient of figure 6.2 (a) indicate a less narrow-band process than that of figure 6.1 (a), while the RMS values are comparable.

It can be seen in figure 6.2 (b) that the magnitude of the acceleration-correlated

force was larger than that of the velocity-correlated force (almost imperceptible at the scale of the figure), which was generally true of the supercritical flow results.

6.4 Effect of Imposed Cylinder Motion on Lift

In most cases, imposition of cylinder motion produced only small changes in sectional lift forces. The most obvious effect was that sharp peaks or spikes were introduced into the spectra of lift forces at the cylinder oscillation frequency, and occasionally at its harmonics as well. The shape and areas of the spectra of residual force were not greatly affected, in general being similar to those measured with the cylinder held fixed. The purpose of this section is to support the proposition that the characteristics of the residual forces, after the extraction of the motion-correlated force terms, were similar to those measured with the cylinder fixed in the same flows. This means that the gross characteristics of lift forces on the oscillating cylinder can be described by the information for the fixed cylinder, presented in chapter 5, in combination with the coefficients of motion-correlated forces to be presented in the next section. Some qualification must be added in the case of smooth subcritical flow, where the motion-correlated forces were often similar in magnitude to the residual forces and non-linear interactions occurred.

6.4.1 Standard deviations of total and residual forces

Standard deviations of sectional lift coefficient are shown as functions of reduced velocity for the low Reynolds number flows in figures 6.3 and 6.5, and for the high Reynolds number flows in figure 6.6. In all cases, the values are the average of the sectional values measured on the four most central transducers of the cylinder. The dashed line in each diagram gives the value of σ_{C_l} measured with the cylinder held fixed prior to the commencement of each set of tests.

Overall, the figures indicate that the values of the coefficients of residual lift were independent of the reduced velocity and were very similar to those found with the cylinder fixed. The general trend of the values of coefficient of total lift was for them to decrease monotonically with increased reduced velocity, except in the case of subcritical smooth flow (fig. 6.3). In that case, standard deviations of coefficient of total lift reached maxima at reduced velocities near 5, which corresponded to coincidence of oscillation and vortex shedding frequencies.

Smooth subcritical flow

Figure 6.3 shows standard deviations of total and residual lift forces measured in smooth subcritical flow ($Re \simeq 1.6 \times 10^5$) at nominal amplitudes of motion α_{nom} of 1%, 2% and 3% of diameter.

When figure 6.3 is examined and compared with figures 6.5 and 6.6, it can be seen that there was more scatter in the value of coefficient of residual lift for smooth subcritical flow than was the case for the remainder of the flows. Some of this variation

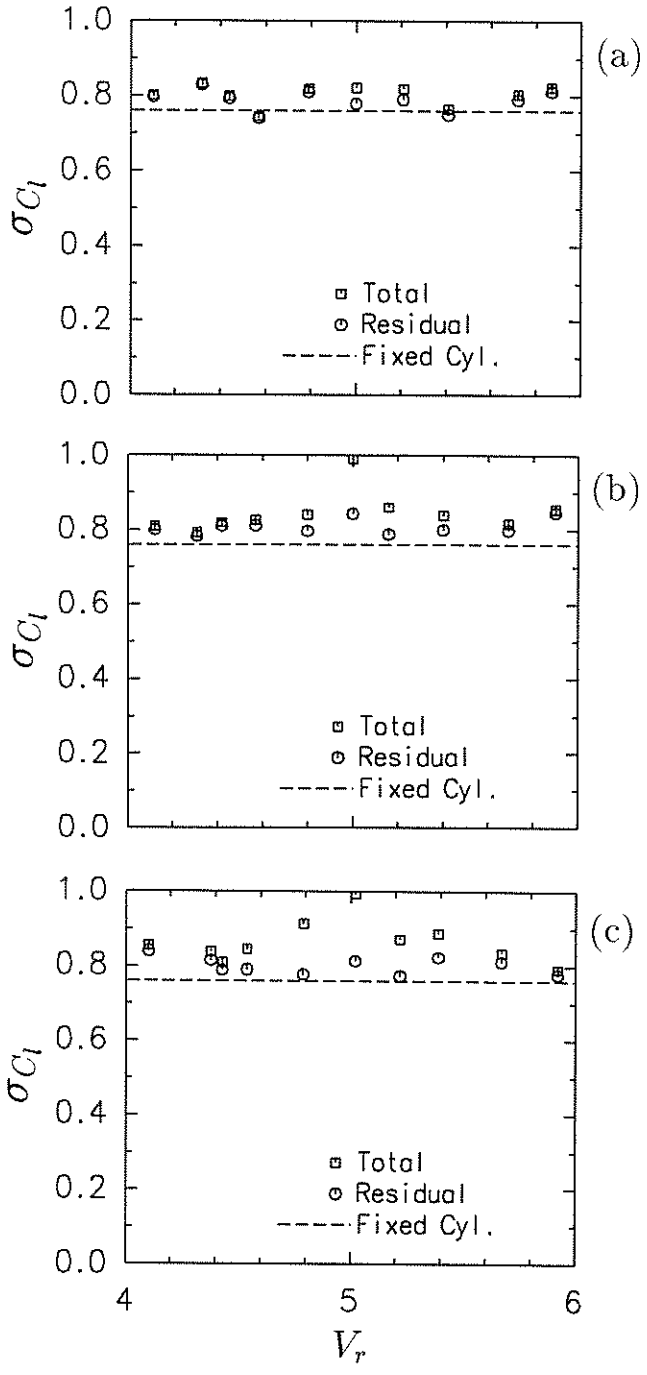

FIGURE 6.3: Standard deviations of total and residual lift force in smooth subcritical flow, $Re \simeq 1.6\times10^5$. Lower dashed line in each graph indicates value of σ_{C_l} with cylinder held fixed at beginning of tests. (a); $\alpha_{\text{nom}} = 1\%$, (b); $\alpha_{\text{nom}} = 2\%$, (c); $\alpha_{\text{nom}} = 3\%$.

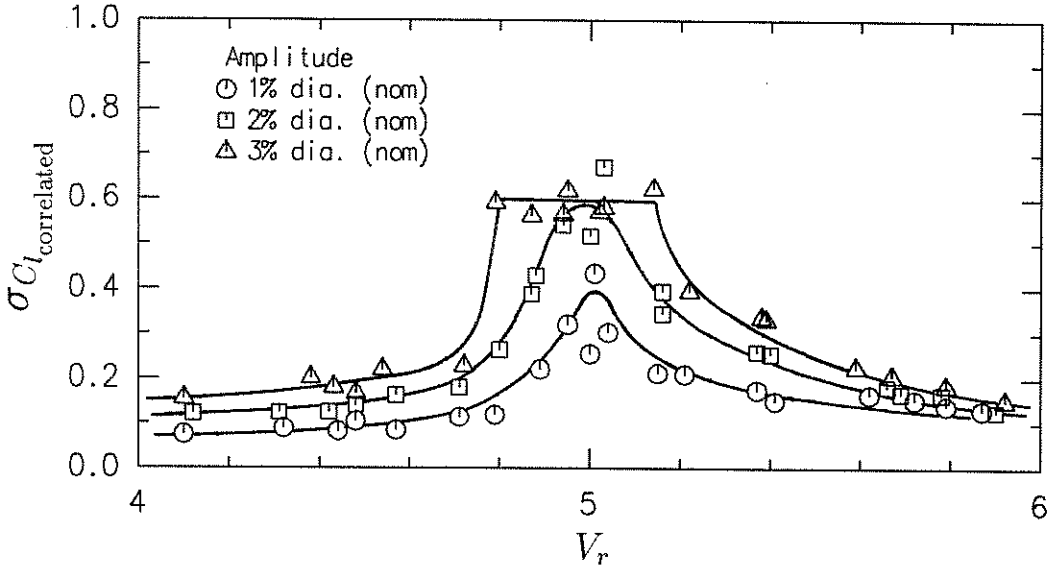

FIGURE 6.4: Values of the differential coefficients $\sigma_{C_{l_{correlated}}}$ of lift (eq. (6.7)) as functions of reduced velocity and amplitude in smooth subcritical flow. The values represent the amount of lift force correlated with cylinder motion.

may be attributed to fluctuation in Reynolds number between one test and the next: while the nominal Reynolds number for figure 6.3 was 1.6×10^5, it actually varied in the range 1.54–1.65×10^5. As was shown in chapter 5 (see figs. 5.14–5), sectional coefficients of lift in this Reynolds regime were sensitive to Reynolds number, tending to reduce with increased Re. When coefficients of residual lift for the smooth subcritical flow were plotted against Reynolds number, evidence of this downward trend could be seen, although it did not account for all the scatter in figure 6.3.

Figure 6.3 indicates that the difference between total and residual lift tended to increase near $V_r = 5$. In order to examine this trend in more detail, while reducing the effect of variability discussed above, the difference between total and residual lift coefficients were computed and plotted in figure 6.4. Since the motion-correlated and uncorrelated forces were by definition uncorrelated components of a random process, the differential coefficients plotted in figure 6.4 are the average values taken over the four central transducers of

$$\sigma_{C_{l_{correlated}}} = \sqrt{\sigma^2_{C_{l_{total}}} - \sigma^2_{C_{l_{residual}}}} \,. \tag{6.7}$$

These coefficients reflect the amount of lift forces which were correlated with cylinder motion. It can be seen that reduced velocity and cylinder amplitude had a definite effect on motion-correlated forces, a point which will be taken up in more detail in §§ 6.5 and 6.6.

Turbulent flows and smooth supercritical flow

Results for smooth supercritical flow are grouped here with those for turbulent flow since there were more similarities between these sets of results than there were between the sub- and supercritical smooth flows. The magnitudes shown are those measured

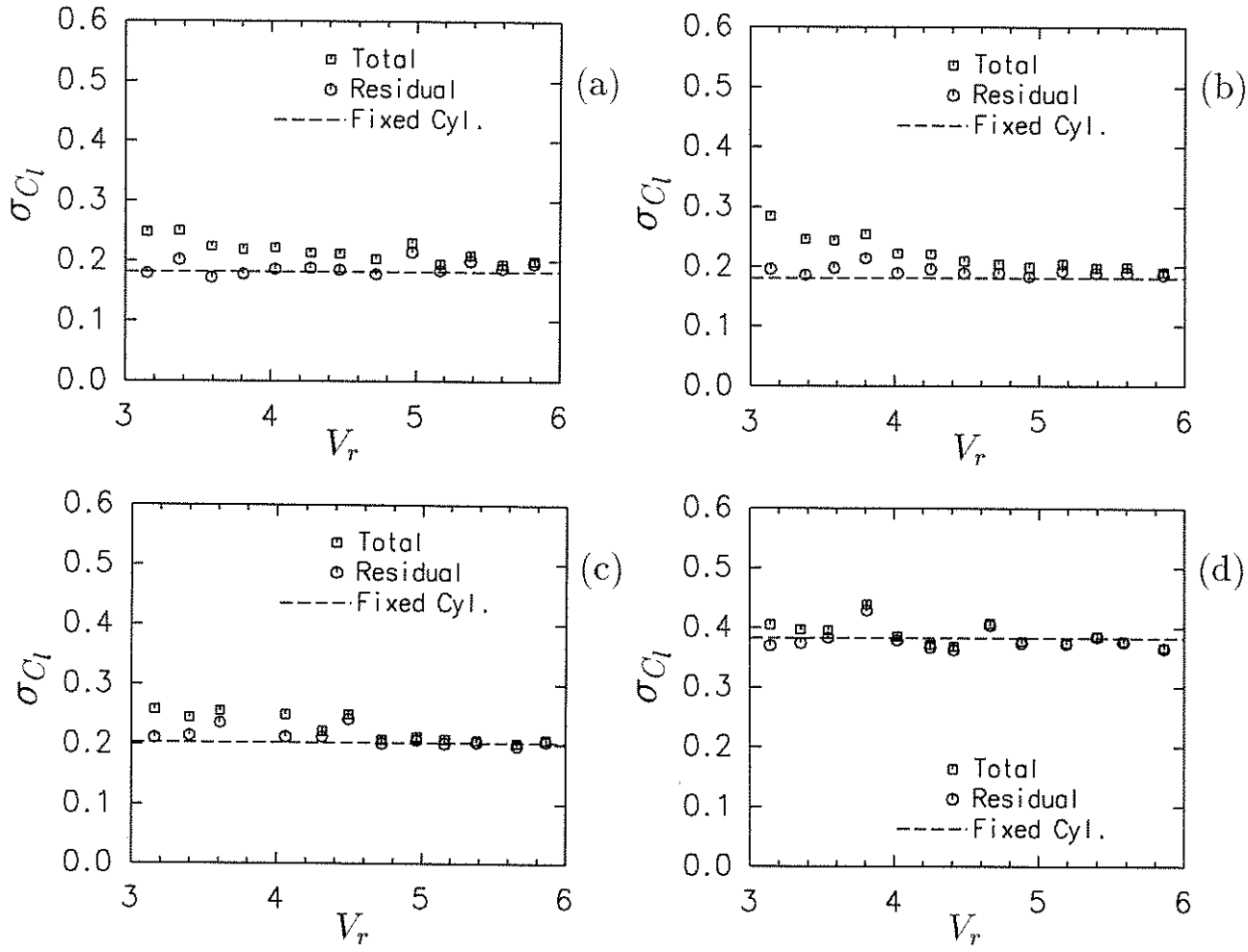

FIGURE 6.5: Standard deviations of total and residual coefficients of lift as functions of reduced velocity for turbulent flows in the low Reynolds number tests. Average values from four central transducers. Dashed lines indicate values measured with cylinder fixed. (a) Config. 1; $I_u = 3.6\%$, $Re \simeq 1.5\times10^5$. (b) Config. 2; $I_u = 4.2\%$, $Re \simeq 1.6\times10^5$. (c) Config. 3; $I_u = 9.6\%$, $Re \simeq 1.5 \times 10^5$. (d) Config. 4; $I_u = 18\%$, $Re \simeq 1.5 \times 10^5$.

at a nominal amplitude $\alpha_{\text{nom}} = 3\%$ in the low Reynolds number flows (fig. 6.5) and at $\alpha_{\text{nom}} = 2\%$ in the high Reynolds number flows (fig. 6.6). The difference between the standard deviations of coefficients of total and residual lift tended to increase with the amplitude of imposed cylinder oscillation and as reduced velocity was reduced (by increasing the frequency of oscillation). It will be shown in § 6.5 that the motion-correlated lift forces in most of the turbulent flow cases were dominated by acceleration-correlated terms.

Comparison with fixed cylinder results

Averages of the residual coefficients of lift taken over the four central transducers and the range of reduced velocities are shown in figure 6.7, where they may be compared with the values measured in the programme of fixed cylinder tests described in the previous chapter (fig. 5.14). The residual values presented are those for the amplitudes used above; $\alpha_{\text{nom}} = 3\%$ for low Reynolds numbers and $\alpha_{\text{nom}} = 2\%$ for high Reynolds

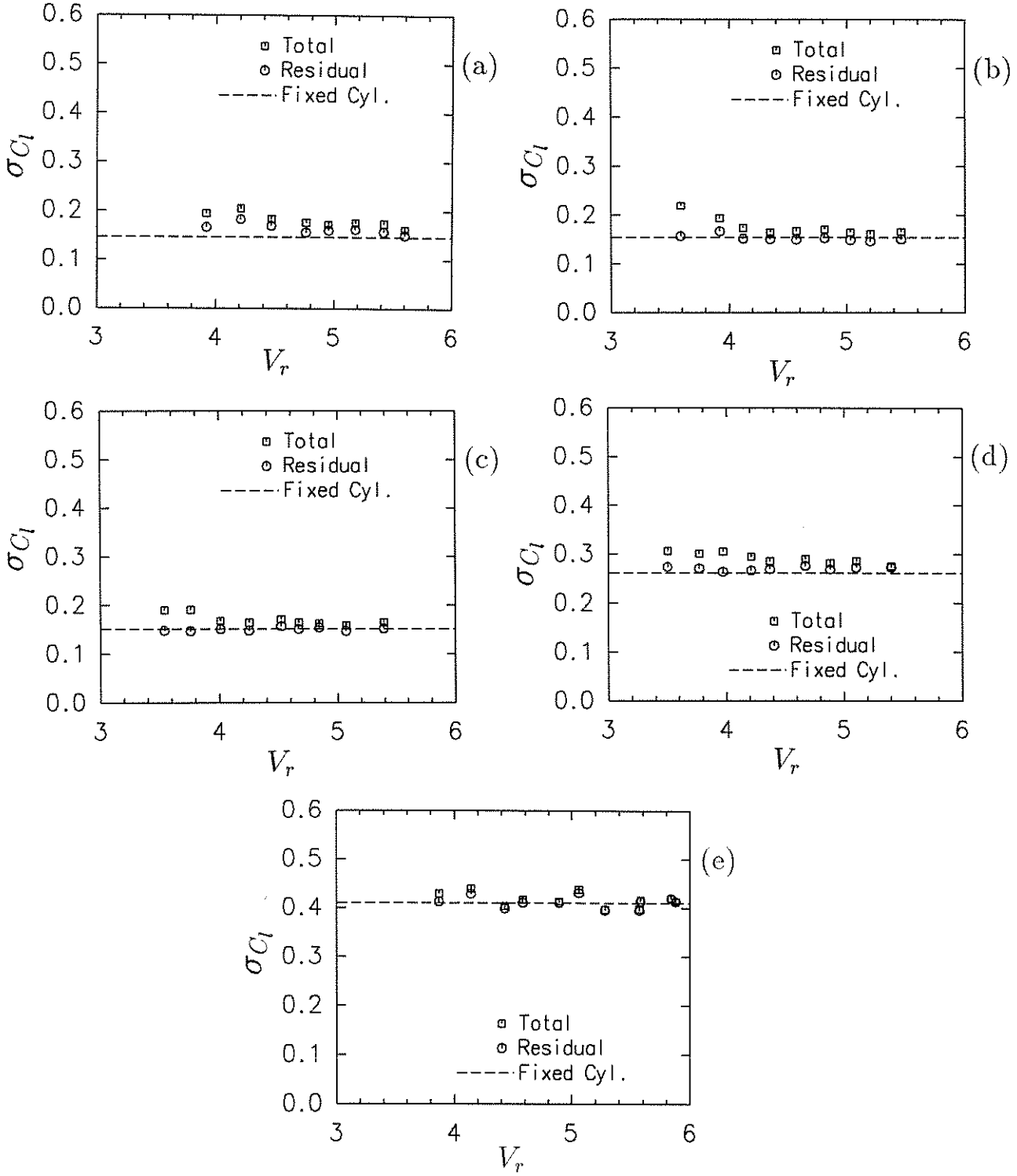

FIGURE 6.6: Standard deviations of total and residual coefficients of lift as functions of reduced velocity for all turbulence configurations in the high Reynolds number tests. Average values from four central transducers. Dashed lines indicate values measured with cylinder fixed. (a) Smooth flow; $I_u = 0.6\%$, $Re \simeq 4.6 \times 10^5$. (b) Config. 1; $I_u = 3.6\%$, $Re \simeq 5.0 \times 10^5$. (c) Config. 2; $I_u = 4.2\%$, $Re \simeq 4.4 \times 10^5$. (d) Config. 3; $I_u = 9.6\%$, $Re \simeq 4.4 \times 10^5$. (e) Config. 4; $I_u = 18\%$, $Re \simeq 4.9 \times 10^5$.

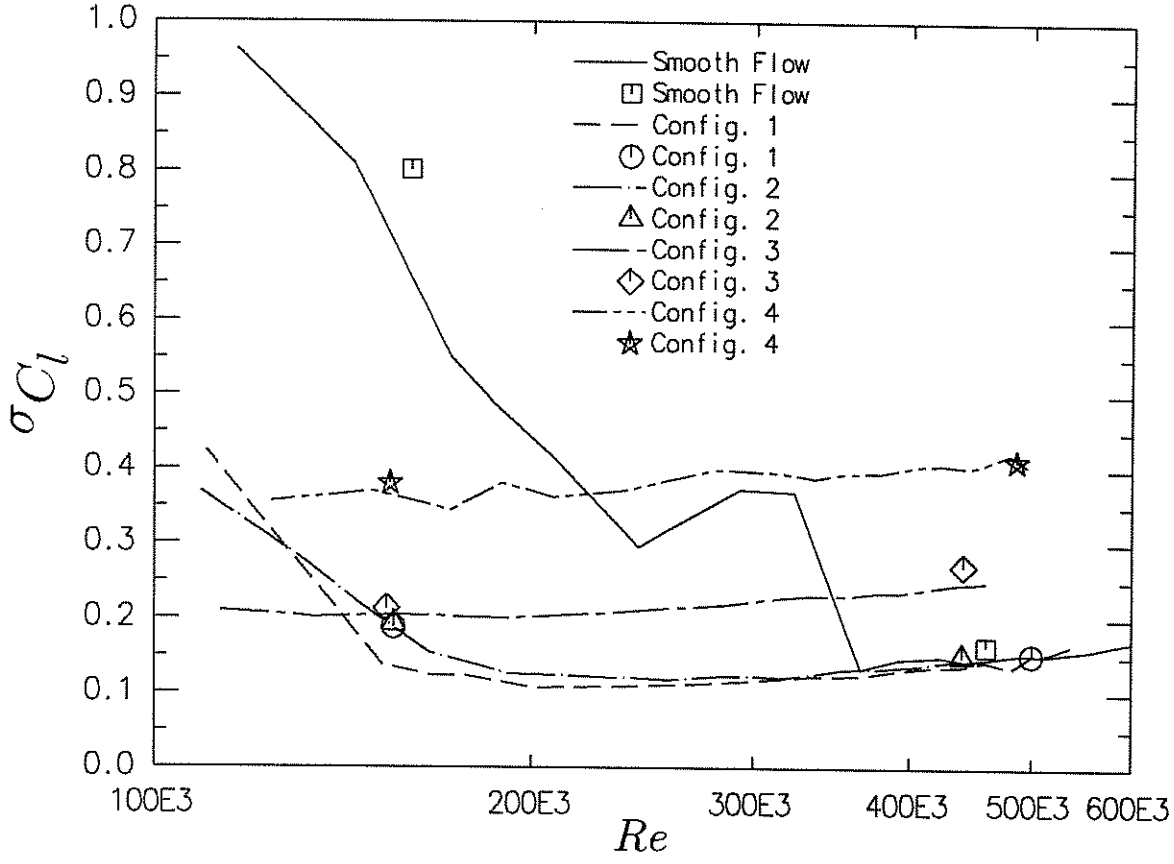

FIGURE 6.7: Average values of standard deviations of coefficient of residual lift compared with results measured with the cylinder fixed.

numbers, but the results for lower amplitudes were similar.

The values are in fair agreement with those obtained from the fixed cylinder. The greatest variation between residual lift and that measured with the cylinder fixed occurred in the smooth subcritical flow.

6.4.2 Spectra of sectional lift forces

As a part of the data processing the spectra of total and residual coefficients of lift were plotted for each transducer and for every set of data collected. As described in § 5.2.1, spectra were prepared using FFT-based techniques, with 30 averages obtained at each frequency point. (Further analysis of the smooth subcritical flow data was carried out using Maximum Entropy Method spectral estimates; see § 6.6 below.)

Representative examples of the spectra of total and residual lift forces will be presented and discussed. As in chapter 5, the spectra are presented with reduced frequency $f_r = fD/U$ as the abscissa, and are normalized so that the area of the spectrum is the variance of coefficient of lift. Dashed vertical lines in the figures indicate the frequency of cylinder oscillation.

Smooth subcritical flow

In figure 6.8 (a) a spectrum of coefficient of total lift in smooth subcritical flow is shown; it is apparent that most of the energy was situated near $f_r = 0.20$, but that there was also energy at the forced oscillation frequency ($f_r = 1/V_r = 0.22$). Figure 6.8 (b) compares the spectrum of residual lift, computed after removal of motion-correlated terms, with that obtained with the cylinder held fixed. While there was some difference in Strouhal number and $\sigma^2_{C_l}$, the spectra were otherwise similar. The spectrum of residual lift was similar to that for total lift force, but with the energy at the cylinder oscillation frequency reduced so that no secondary peak appeared at the cylinder oscillation frequency.

In figure 6.9, a similar comparison is made, but in this case the reduced velocity $V_r = 5.02$ (it will be shown in § 6.6 that lock-in had occurred). It is evident that the total lift force was significantly greater than in figure 6.8 (a) but that the residual lift was again similar to that for the fixed cylinder.

The spectra of residual force presented in figures 6.8 (b) and 6.9 (b) show that some of the energy at the cylinder oscillation frequencies had been removed by the correlation process. In the case of figure 6.8 (b), the peak at the cylinder oscillation frequency has been removed, leaving the remainder of the spectrum unchanged. It is apparent that in both cases not all the energy at the cylinder oscillation frequency has been removed by extraction of motion-correlated force; for example in figure 6.8 (b), sufficient residual energy was left to provide a smooth spectral shape.

Comparison of figures 6.8 (b) and 6.9 (b) shows that the spectrum of residual lift is similar to that for the fixed cylinder. The slight difference in Strouhal numbers between the residual spectra from the oscillating cylinder and the spectra from the fixed cylinder is not regarded as significant, most probably being attributable to errors in measurements of mean flow velocity.

Spectra for smooth subcritical flow present a striking illustration of the progression of spectral peaks at the cylinder oscillation frequencies as the reduced velocity was adjusted, as shown in figure 6.10 (a). It is interesting to compare this with a similar plot, prepared by Szechenyi and Loiseau (1975, see fig. 1.53), which shows a similar progression in the spectra of lift force in transcritical flow past a roughened cylinder. In their experiments, Reynolds number and reduced velocity were varied simultaneously, since variation in reduced velocity was achieved by changing the flow velocity rather than the cylinder oscillation frequency. Figure 6.10 (b) shows the progression of spectra of the residual lift forces prepared from the same data used for figure 6.10 (a). The spectral peaks at the cylinder oscillation frequencies have been removed and, in the range of reduced velocity where the two peaks coalesce in figure 6.10 (a), the areas of the spectra of residual forces in (b) remained nearly constant as reduced velocity was varied.

Turbulent flow

Figure 6.11 repeats the comparison of figure 6.8 but this time in the flow of highest turbulence intensity (Config. 4, $I_u = 18\%$) and at high Reynolds number ($Re = 4.7 \times$

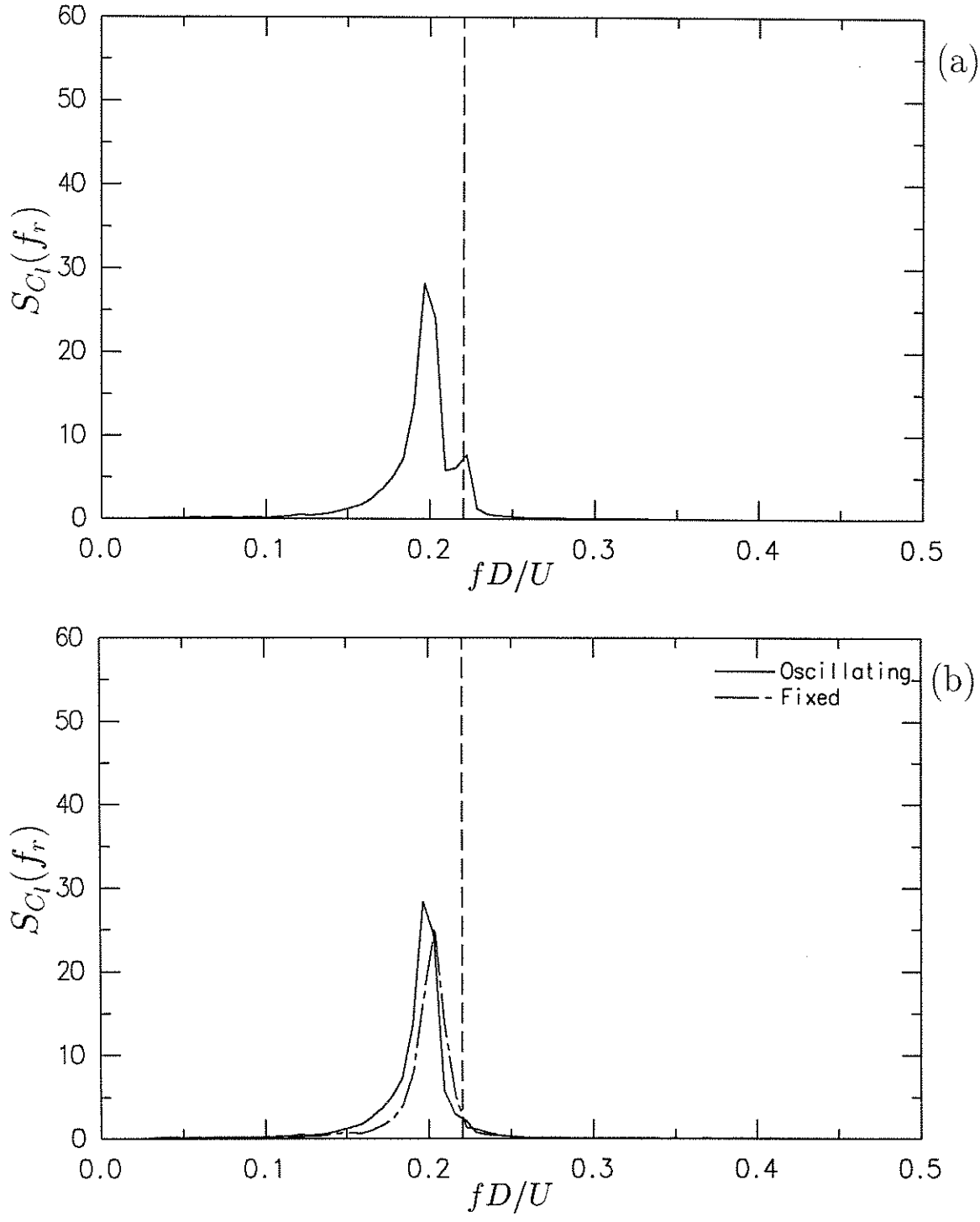

FIGURE 6.8: Spectra of lift of cylinder oscillating in smooth subcritical flow compared with spectrum for stationary cylinder. $V_r = 4.54$, $\alpha_{\text{nom}} = 3\%$. (a) Oscillating cylinder; spectrum of total lift force. (b) Comparison of spectrum prepared from timeseries of residual lift with that obtained with cylinder held fixed.

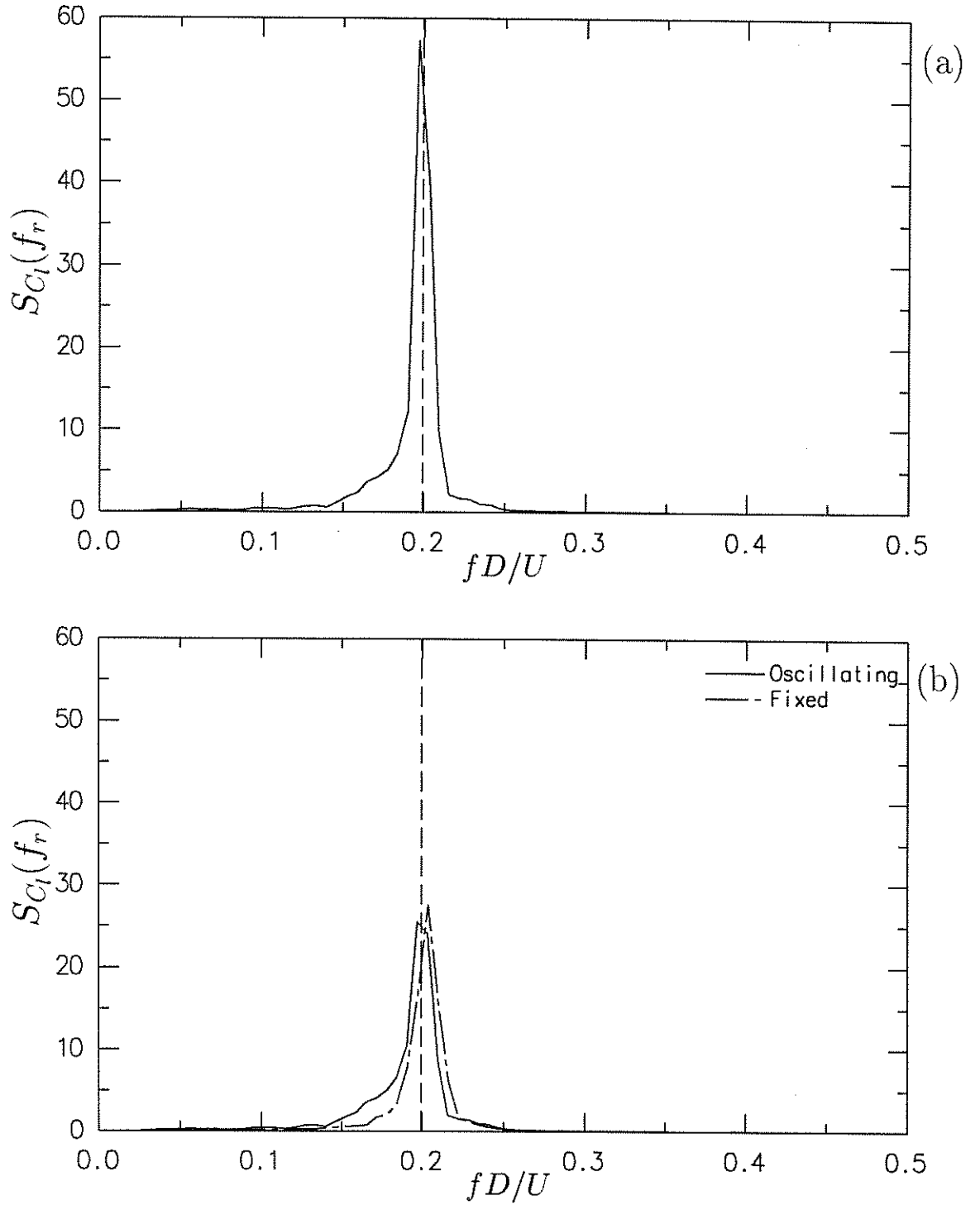

FIGURE 6.9: Spectra of lift of cylinder oscillating in smooth subcritical flow compared with spectrum for stationary cylinder. $V_r = 5.02$, $\alpha_{\text{nom}} = 3\%$. (a) Oscillating cylinder; spectrum of total lift force. (b) Comparison of spectrum prepared from timeseries of residual lift with that obtained with cylinder held fixed.

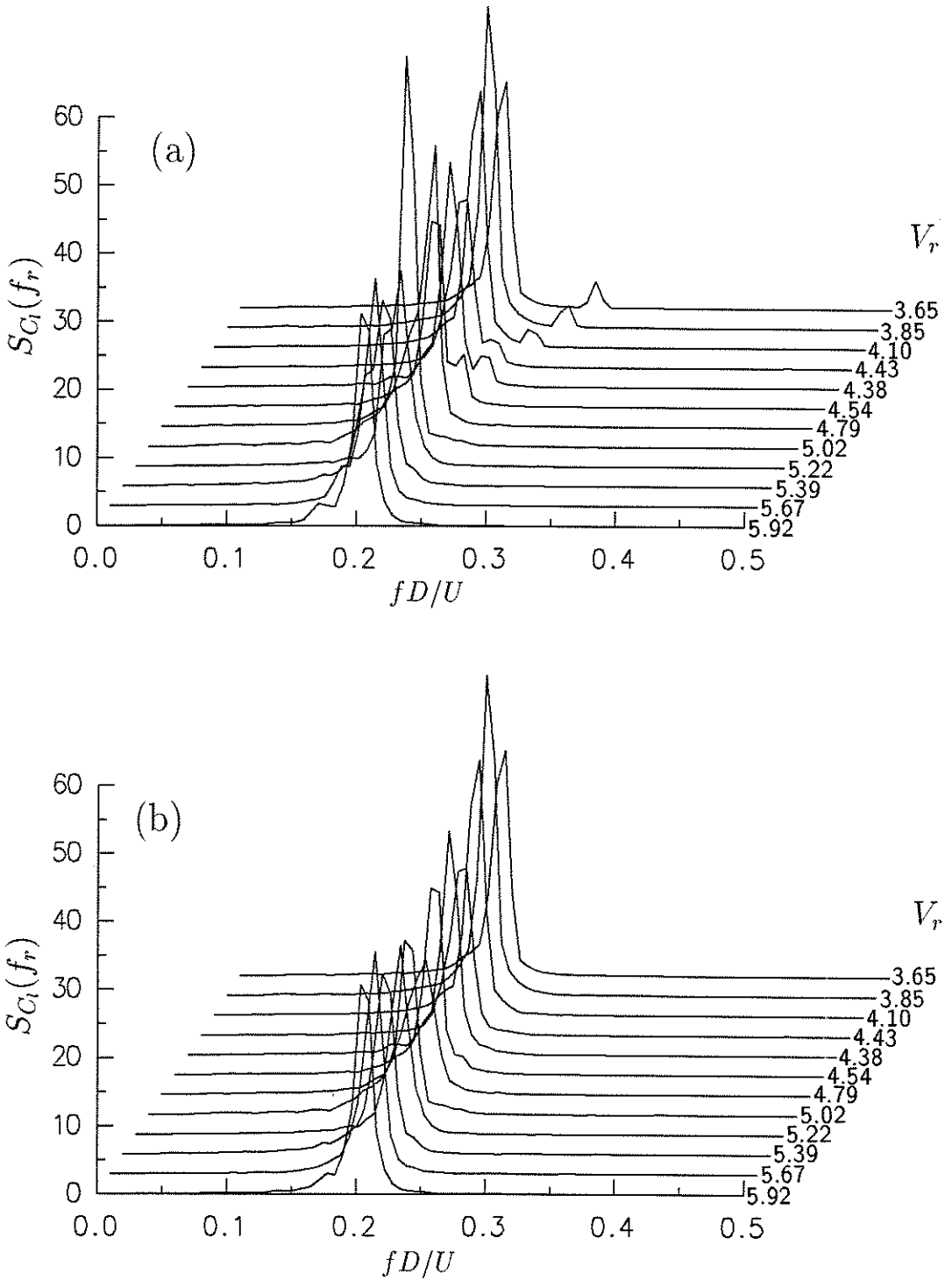

FIGURE 6.10: Waterfall plots of the progression of lift force spectra with reduced velocity in smooth subcritical flow. (a) Spectra of total lift force. (b) Spectra of residual lift force.

10^5). As for figure 6.8 (a), there was a spectral peak at the cylinder oscillation frequency, which was removed when motion-correlated force timeseries were extracted prior to spectral analysis. The spectrum of lift force from the fixed cylinder is again similar to the spectrum of residual force for the oscillating cylinder.

In a final comparison, figure 6.12 shows spectra of lift force from the low turbulence intensity ($I_u = 3.6\%$) low Reynolds number ($Re = 1.5 \times 10^5$) flow. In this case the spectral peak at the cylinder oscillation frequency is quite large by comparison with the background spectral values which reflects the fact that the standard deviation of coefficient of lift was lower in this case than for the two previous figures. Also in this case peaks appeared in the spectra of total and residual lift forces at the second and third harmonics of the cylinder oscillation frequency. They were not removed by the correlation process since different harmonics of sinusoids are orthogonal functions. These higher harmonics were often observed in spectra from the $I_u = 3.6\%$ and $I_u = 4.2\%$ flows and in the others more occasionally.

6.4.3 Spanwise correlation of sectional lift forces

Cross-correlations of sectional total and residual lift forces obtained at different locations along the span were computed, enabling estimates of spanwise correlation lengths to be made using the methods discussed in chapter 5. For all the flows except smooth subcritical, the spanwise correlations of residual forces were indistinguishable from those estimated for forces on the stationary cylinder. In the subcritical flow, there were some indications that correlation lengths of residual forces tended to decrease a little when motion-correlated forces were large, as will be discussed below. The spanwise correlation of total lift forces were greater than for the residual forces, indicating that the motion-correlated forces had greater spanwise correlation than forces which acted on the fixed cylinder (see § 6.5.4). The amount by which the spanwise correlation of total forces was greater than that of residual forces varied with the relative magnitude of the motion-correlated and residual forces. This point will be taken up in greater detail in § 6.5.

Turning first to turbulent flow, some typical examples of spanwise distribution of correlation coefficient are presented in figures 6.13 and 6.14. Figure 6.13 was prepared from data collected in turbulence configuration 1 ($I_u = 3.6\%$), at the low end of the Reynolds number range. Cylinder oscillation amplitude was 3% of diameter. Also presented are correlation coefficients obtained with the cylinder held fixed in the same flow. It can be seen that the coefficients for the lift measured on the fixed cylinder and for the residual lift on the oscillating cylinder were very similar ($\Lambda \simeq 1.25$). The correlation coefficients for the oscillating cylinder were considerably higher, which is a reflection of the fact the the motion-correlated forces were large in relation to the forces on the fixed cylinder (see also fig. 6.12). At the high end of the Reynolds number range, and at the highest turbulence intensity (config. 4, $I_u = 18\%$, $\alpha_{\text{nom}} = 2\%$), figure 6.14 shows that motion-correlated forces did not contribute such a large change in spanwise correlation, this time reflecting that motion-correlated forces were small compared to those on the fixed cylinder. Again, the residual forces showed a similar spanwise distribution of correlation as the forces on the fixed cylinder ($\Lambda \simeq 1.5$).

In the smooth subcritical flow, there was a greater variation of spanwise correlation

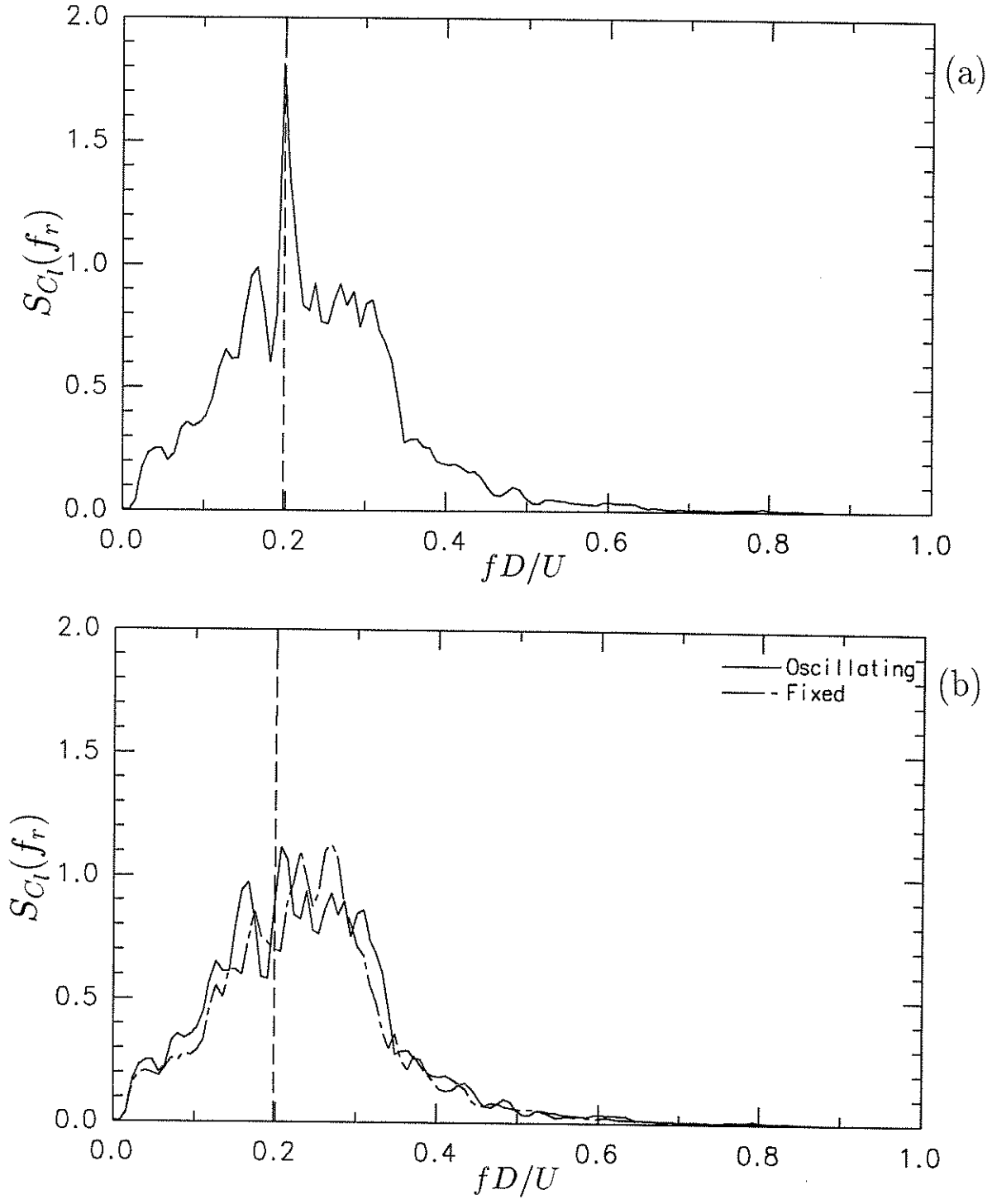

FIGURE 6.11: Spectra of lift of cylinder oscillating in high Reynolds number turbulent flow (Config. 4; $I_u = 18\%$, $Re = 4.7 \times 10^5$, $V_r = 5.06$, $\alpha_{\text{nom}} = 2\%$) compared with spectrum for stationary cylinder at same Re. (a) Oscillating cylinder; spectrum of total lift force. (b) Comparison of spectrum prepared from timeseries of residual lift with that obtained with cylinder held fixed.

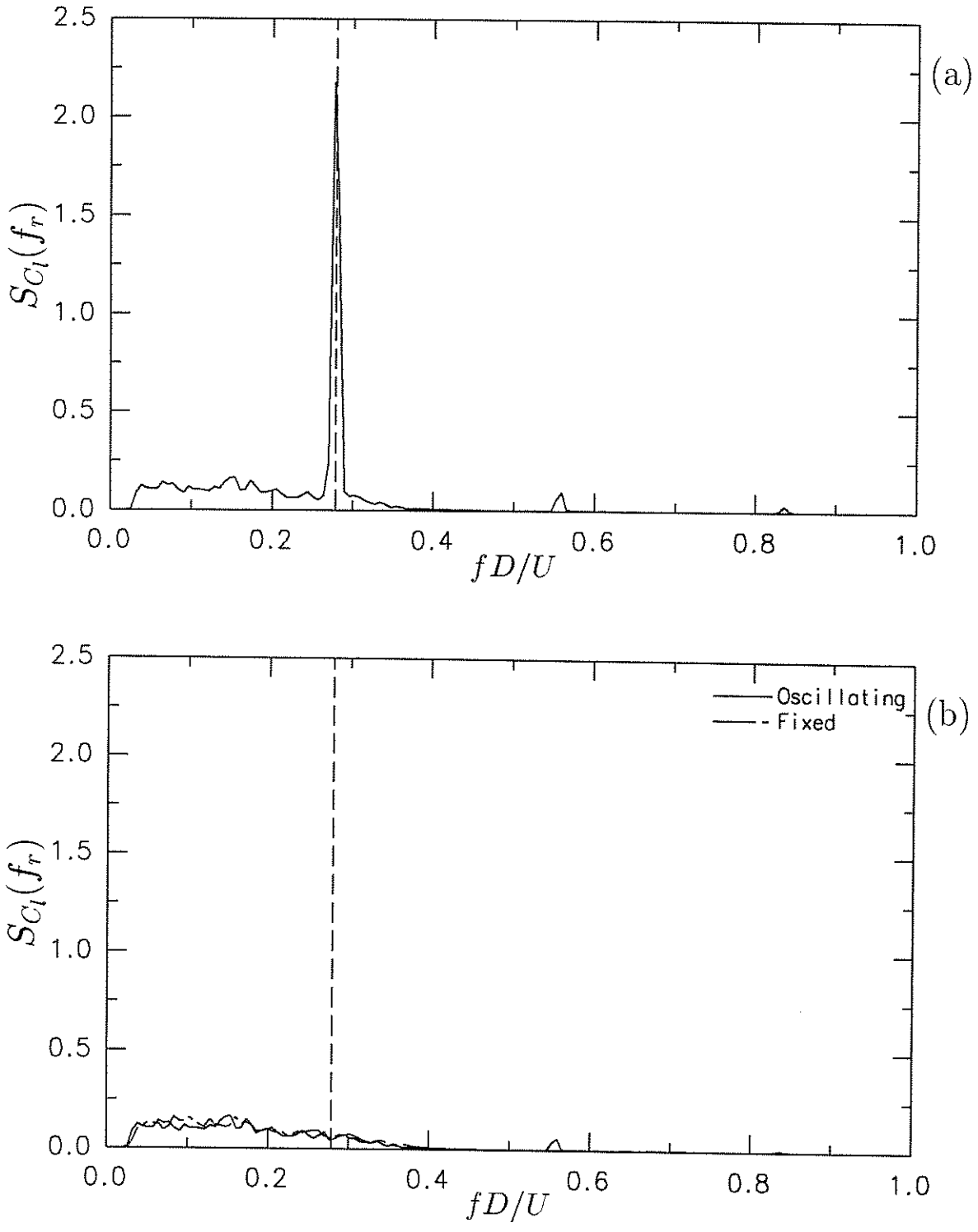

FIGURE 6.12: Spectra of lift of cylinder oscillating in low Reynolds number (Config. 1; $I_u = 3.6\%$, $Re = 1.5 \times 10^5$), $V_r = 3.59$, $\alpha_{\text{nom}} = 3\%$) compared with spectrum for stationary cylinder. (a) Oscillating cylinder; spectrum of total lift force. (b) Comparison of spectrum prepared from timeseries of residual lift with that obtained with cylinder held fixed.

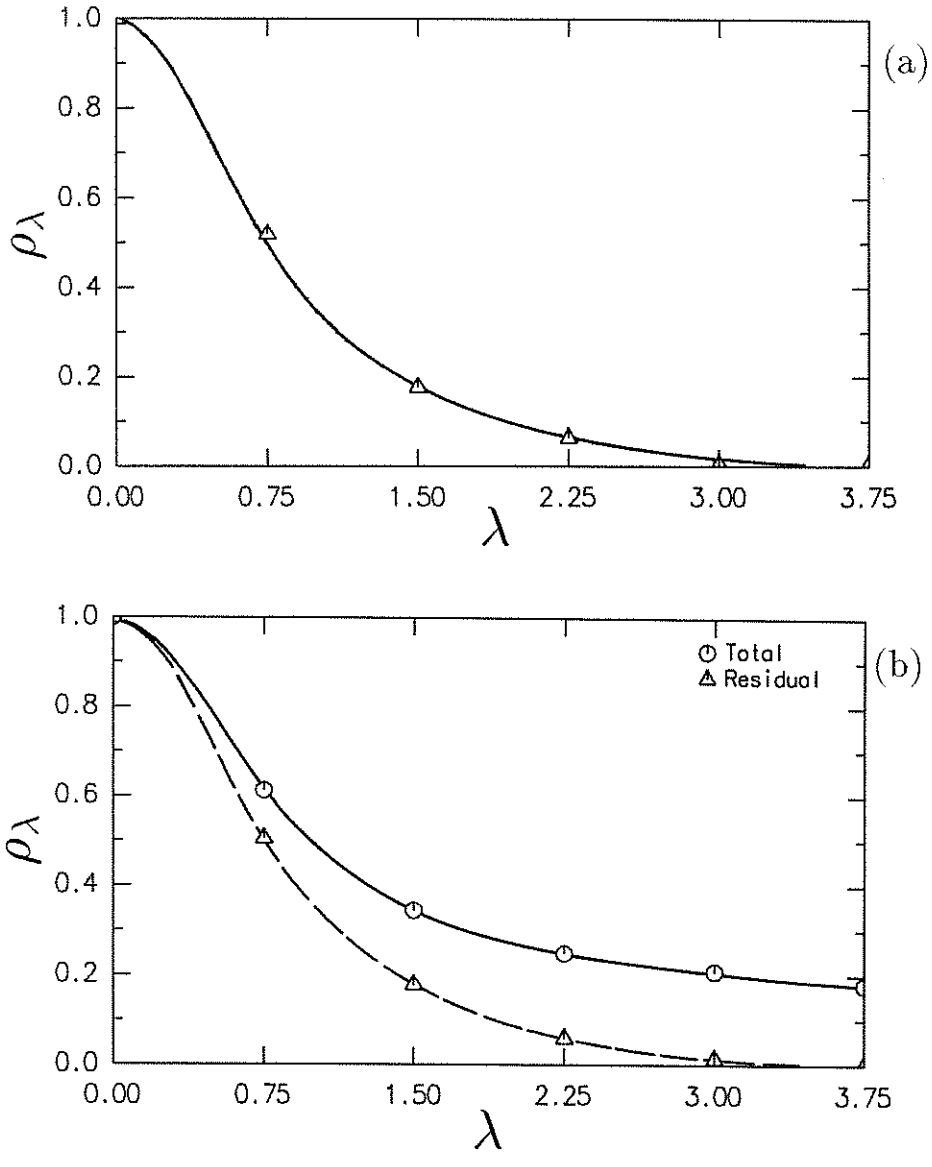

FIGURE 6.13: Correlation coefficient of lift forces as functions of spacing along the span in low Reynolds number (1.5×10^5) turbulent flow (config. 1, $I_u = 3.6\%$). Correlations of total and residual lift are shown and compared with correlations obtained on the fixed cylinder. (a); Cylinder fixed. (b); Oscillating cylinder, correlation of total and residual forces.

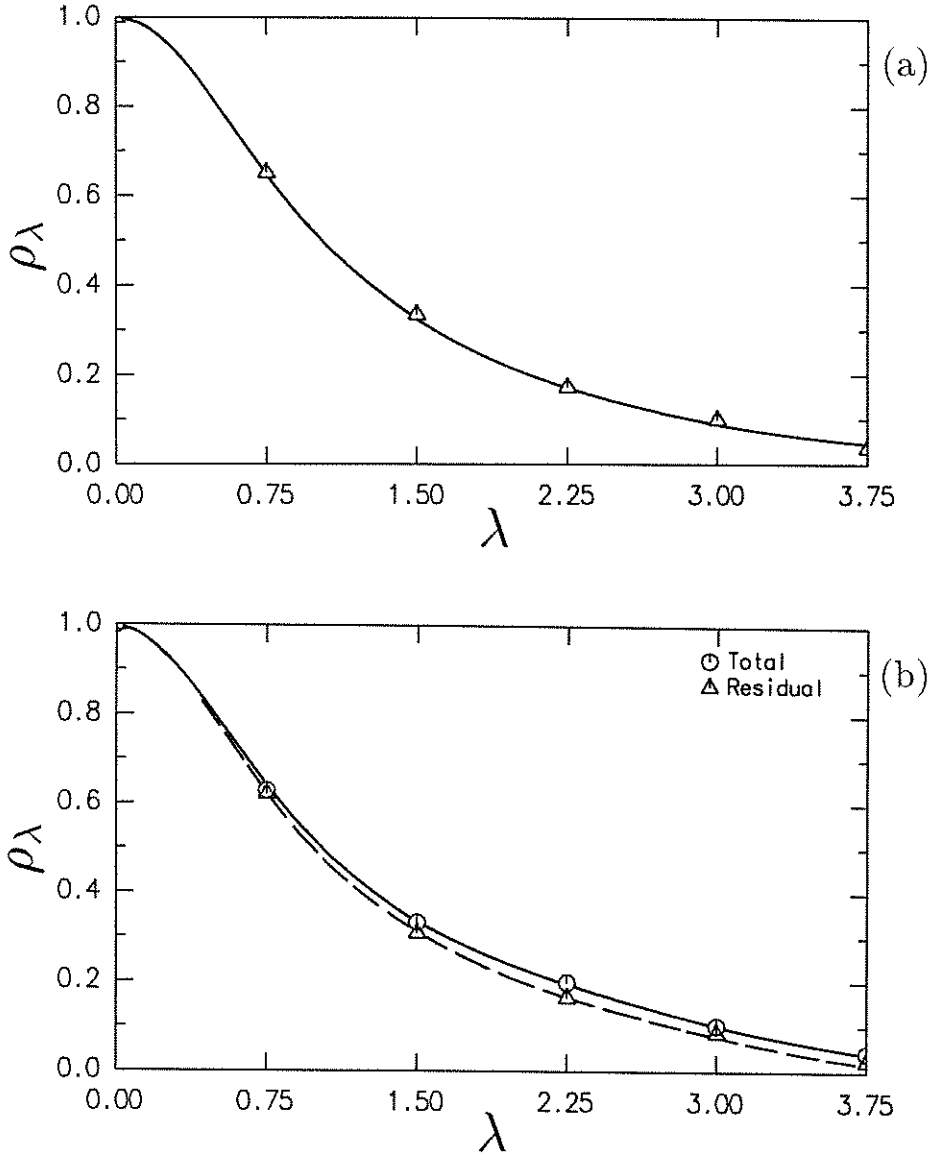

FIGURE 6.14: Correlation coefficient of lift forces as functions of spacing along the span in high Reynolds number (4.6×10^5) turbulent flow (config. 4, $I_u = 18\%$). Correlations of total and residual lift are shown and compared with correlations obtained on the fixed cylinder. (a); Cylinder fixed. (b); Oscillating cylinder, correlation of total and residual forces.

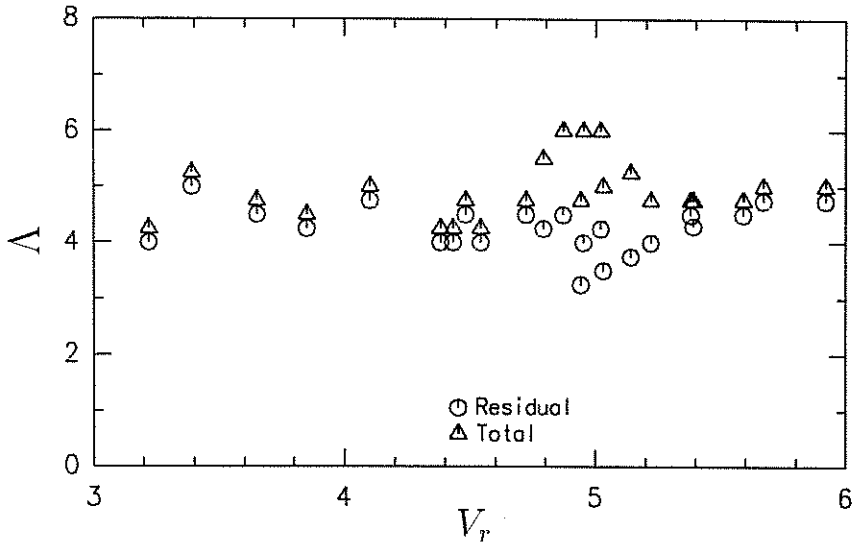

FIGURE 6.15: Spanwise correlation lengths Λ for total and residual lift forces shown as functions of reduced velocity for smooth subcritical flow ($Re \simeq 1.6 \times 10^5$, $\alpha_{\text{nom}} = 3\%$).

of residual forces than for the other flows. This may in part be due to the variability of spanwise correlation which was also found when the cylinder was fixed, as shown for example in the precritical part of figure 5.38. It was found that even with nominally constant Reynolds number and the cylinder held fixed, correlation lengths could vary by up to one cylinder diameter between runs. The difference between correlations of total and residual forces was strongly a function of reduced velocity, as could be inferred by inspection of figures 6.3 and 6.4. These features are demonstrated in figure 6.15, in which correlation lengths obtained by the overlay technique introduced in chapter 5 are shown as functions of reduced velocity for smooth subcritical flow[1]. Inspection of the figure reveals that the spanwise correlation of total lift forces tended to increase near the critical reduced velocity of 5. While the figure shows a fair degree of scatter of correlation length for the residual forces, there is indication that correlation tended to decrease slightly near $V_r = 5$. The effect of reduced velocity on the difference in correlation between total and residual lift illustrated in figure 6.16, which is analogous to figure 6.4.

As an illustration of the effect of imposed cylinder oscillation on correlation coefficients near critical reduced velocity in smooth subcritical flow, figure 6.17 shows how the spanwise correlation of total sectional lift increased with amplitude of motion at $V_r = 5.0$. On average, the spanwise correlation of residual force remained similar to that for the fixed cylinder.

[1]It should be pointed out that if motion-correlated forces are perfectly correlated along the span, then correlation length $\Lambda = \int_0^\infty \rho_\lambda d\lambda$ becomes infinite. The correlation curves discussed in chapter 5 did not provide a particularly good fit to the correlations of total force, and the "correlation lengths" of total force in figures 6.15 and 6.16 only give an indication of the scale of increase in correlation provided by motion of the cylinder.

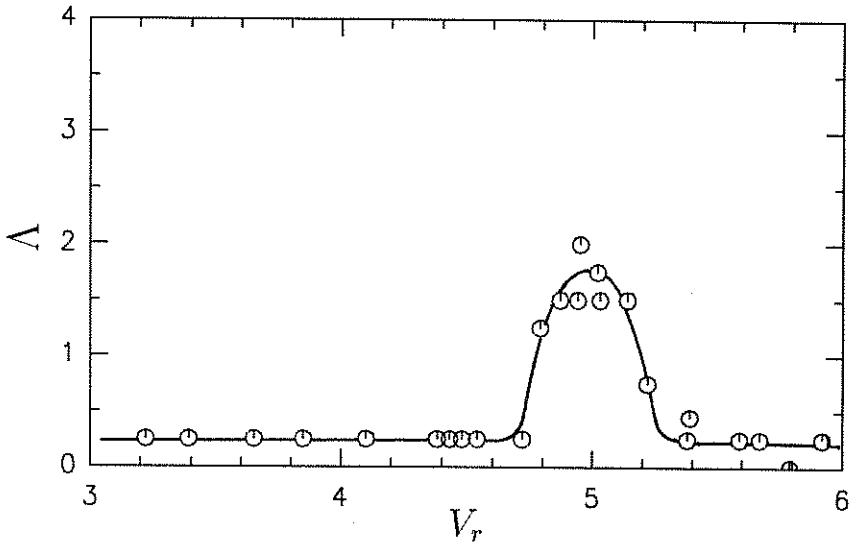

FIGURE 6.16: Difference between correlation lengths of total and residual lift forces as a function of reduced velocity in smooth subcritical flow ($Re \simeq 1.6 \times 10^5$, $\alpha_{\text{nom}} = 3\%$).

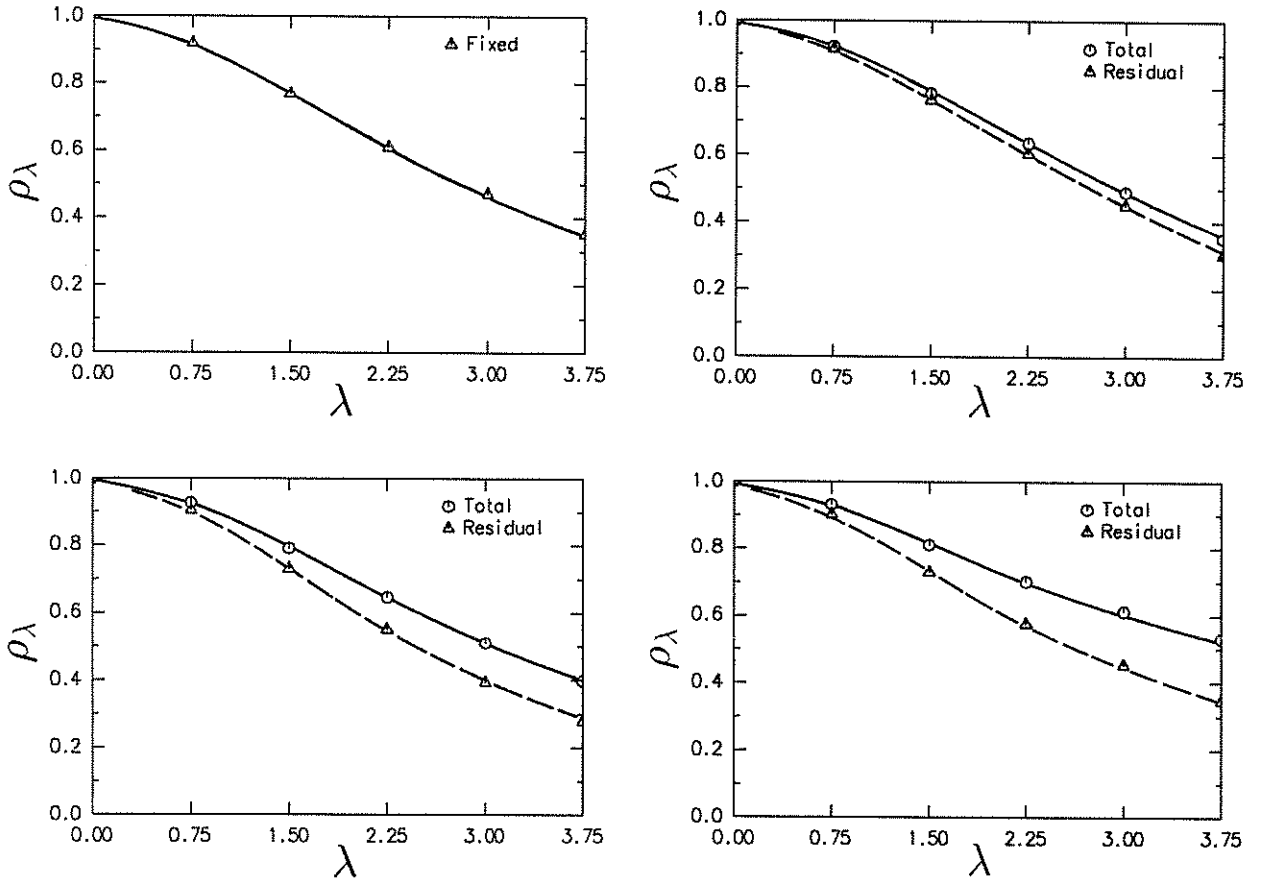

FIGURE 6.17: Effect of cylinder oscillation amplitude on spanwise correlation at $V_r = 5.0$ in smooth subcritical flow. (a) Fixed cylinder. (b) Oscillating; $\alpha = 0.96\%$. (c) Oscillating; $\alpha = 1.88\%$. (d) Oscillating; $\alpha = 2.60\%$.

6.4.4 Probability density of lift force

For all flows except smooth subcritical flow, PDFs of total and residual sectional lift forces were indistinguishable from Gaussian, as were the PDFs of residual force in smooth subcritical flow. In the subcritical smooth flow, the PDFs for total force tended to be more clustered around the mean value than for a Gaussian distribution, providing negative kurtosis. This was due to the contribution of motion-correlated forces.

6.5 Motion-Correlated Force Coefficients

The motion-correlated coefficients of lift, computed by the method described in § 6.3, are presented here in the form of coefficient of added mass, C_a, and aerodynamic damping parameter K_a. As discussed in chapter 1, these coefficients are related to the motion-correlated coefficients of lift, C_{la} and C_{lv} by

$$C_a = -\frac{C_{la} V_r^2}{2\pi^3 \alpha} \tag{6.8}$$

$$K_a = \frac{C_{lv} V_r^2}{16\pi^2 \alpha} \,. \tag{6.9}$$

The choice of C_a and K_a over C_{la} and C_{lv} amounts to adoption of a structural dynamics as against an aerodynamical interpretation, but of course the same forces are described.

Positive values of C_a imply that on average, the acceleration-correlated forces acted on the cylinder in anti-phase to the acceleration, as would be applied by an additional mass attached to the cylinder. A value of unity means that the equivalent additional mass per unit length is the mass of fluid displaced per unit length of the cylinder. This description of the acceleration-correlated forces gives a readily-interpreted physical picture, but it must be remembered that the forces were due to vortex shedding, and are part of the description of the average magnitude and phase relationship of motion-correlated forces.

Positive values of K_a imply that the velocity-correlated forces acted in phase with cylinder velocity, transferring power from the fluid to the oscillating cylinder—positive values of K_a correspond to negative aerodynamic damping. The advantage of describing velocity-correlated forces in this form is that the aerodynamic damping force per unit length is converted to dimensionless form in K_a in the same way that the structural damping force per unit length is in the mass-damping parameter K_s. This means that the values of K_a and K_s may be directly compared. If the values of K_a and K_s are the same, the implication is that on average, an elastically-mounted cylinder oscillating at the appropriate amplitude would have power transferred to it from the fluid at the same rate as it is dissipated to heat by structural damping. In other words, the case where K_a and K_s are the same is a stability boundary for the cylinder.

6.5.1 Error estimates

Reliable estimates of motion-correlated force coefficients were heavily dependent on the accuracy of the cancellation of the inertial component of force transducer signal, as described in chapter 4. It is very difficult to establish a method to gauge the accuracy of this process in practice.

Estimates of errors in values of C_a and K_a can be made on the basis of the observed error in cancellation of inertial signal in the absence of flow (shown in §4.2.1 to be of the order of one analogue-to-digital conversion increment—5 mV). In the estimates that follow, it is assumed that errors in C_a and K_a were dominated by errors in cancellation of inertial signal, and that errors in quantities such as air density and velocity were not significant. If it is assumed that all the error energy lies at the frequency of cylinder oscillation (conservative, as inspection of fig. 4.7 shows), then estimates of error in C_a and K_a can be made on the basis of equations (6.8) and (6.9). At the low Reynolds numbers, a representative value of transducer sensitivity was 0.7 N/V. Then taking $U = 12\,\mathrm{m/s}$, $\rho = 1.2\,\mathrm{kg/m^3}$, $\nu = 15 \times 10^{-6}\,\mathrm{m^2/s}$, $D = 0.2\,\mathrm{m}$, $\Delta L = 0.02\,\mathrm{m}$, the error in estimate of motion-correlated lift standard deviation,

$$\mathcal{E}(\sigma_{C_l}) = \frac{0.7 \cdot 5 \times 10^{-3}}{\frac{1}{2} \cdot 1.2 \cdot 12^2 \cdot 0.2 \cdot 0.02} = 10.1 \times 10^{-3} \tag{6.10}$$

Introducing this value into equations (6.8) and (6.9) gives the estimates of error in table 6.1.

TABLE 6.1: Estimates of error in C_a and K_a at $Re = 1.6 \times 10^5$.

	$V_r = 4$		$V_r = 5$		$V_r = 6$	
α	C_a	K_a	C_a	K_a	C_a	K_a
0.01	0.523	0.103	0.817	0.160	1.176	0.231
0.02	0.261	0.051	0.408	0.080	0.588	0.115
0.03	0.174	0.034	0.272	0.053	0.392	0.077

Likewise, at $Re = 4.7 \times 10^5$, taking a representative transducer sensitivity as 5.0 N/V and $U = 35\,\mathrm{m/s}$ gives the estimates in table 6.2.

TABLE 6.2: Estimates of error in C_a and K_a at $Re = 4.7 \times 10^5$.

	$V_r = 4$		$V_r = 5$		$V_r = 6$	
α	C_a	K_a	C_a	K_a	C_a	K_a
0.01	0.017	0.003	0.027	0.006	0.039	0.007
0.02	0.009	0.001	0.014	0.003	0.020	0.004
0.03	0.006	0.001	0.009	0.001	0.013	0.003

Unfortunately, the estimates just given only provide indication of the magnitude of error, since cancellation carried out in the absence of flow does not fully replicate

experimental conditions, where for example there would be drag loads and additional sources of mechanical vibration applied to the transducers. This leads to the possibility that errors could be somewhat larger in practice. In this case, less direct techniques can be applied, such as estimation of the scatter of results about lines of best fit to the data, or observing the relationship of results recorded at one spanwise station to those at another. Both these methods involve the inherent risk of assumption of the underlying behaviour of experimental data.

6.5.2 Low Reynolds number results

For this set of tests, the Reynolds number was maintained near 1.6×10^5. Measurements were taken with the cylinder oscillating at nominal amplitudes $\alpha = 1\%$, 2% and 3% in the five flow configurations. Reduced velocity was varied (typically between 3 and 6) by changing the frequency of cylinder oscillation in the range 10 Hz to 20 Hz. Results are provided for all six force transducers which were incorporated in the cylinder.

The set of results for smooth subcritical flow—the first to be presented—had the largest motion-correlated force coefficients, and showed the greatest degree of variation with reduced velocity. This is related to the very well-defined frequency of vortex shedding in this flow regime.

Smooth subcritical flow; $\alpha_{\text{nom}} = 1\%$

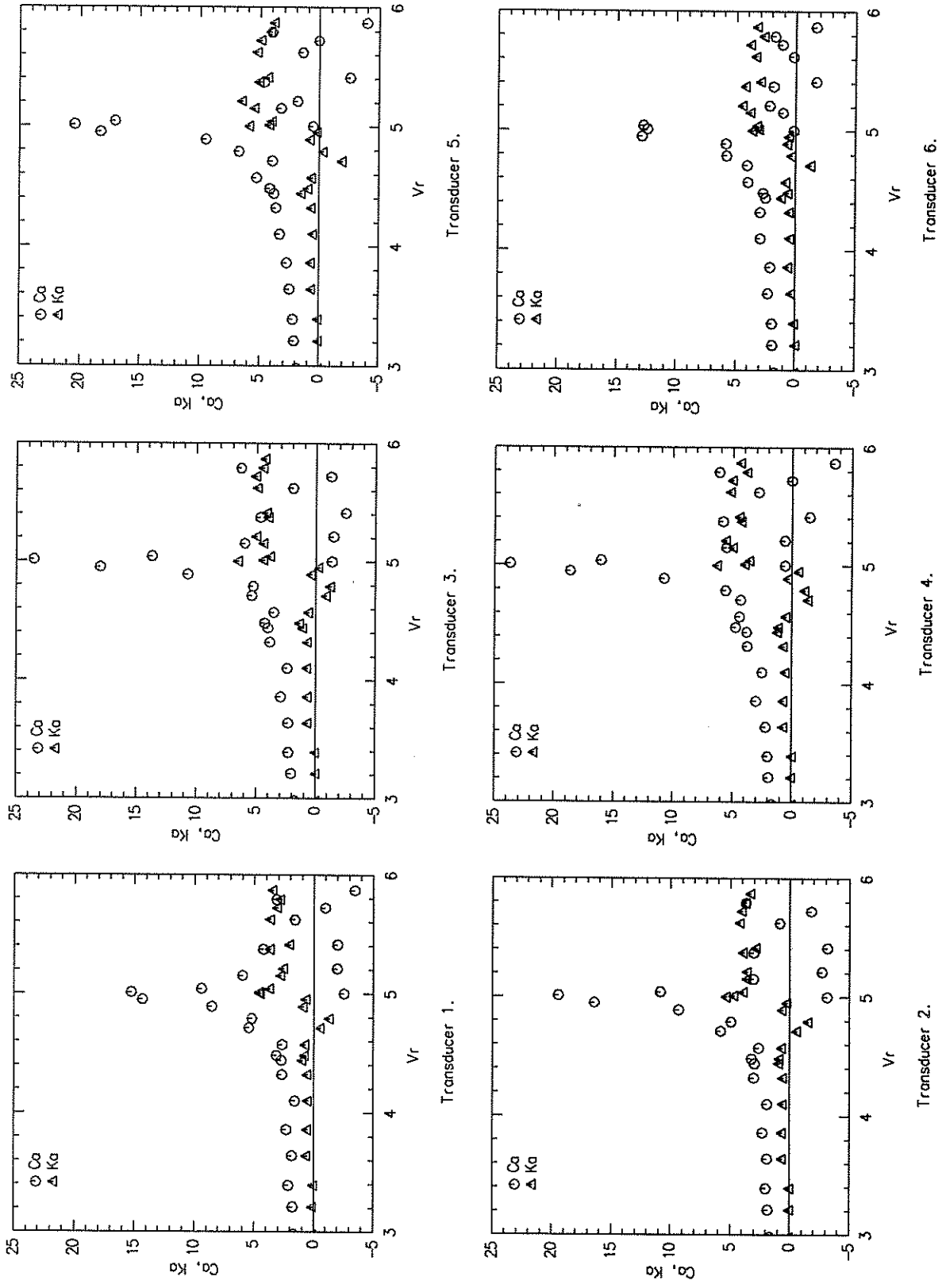

FIGURE 6.18: $\alpha_{\text{nom}} = 1\%$ Values of motion-correlated force parameters C_a and K_a as functions of reduced velocity in smooth subcritical flow. $Re = 1.6 \times 10^5$.

Smooth subcritical flow; $\alpha_{\text{nom}} = 2\%$

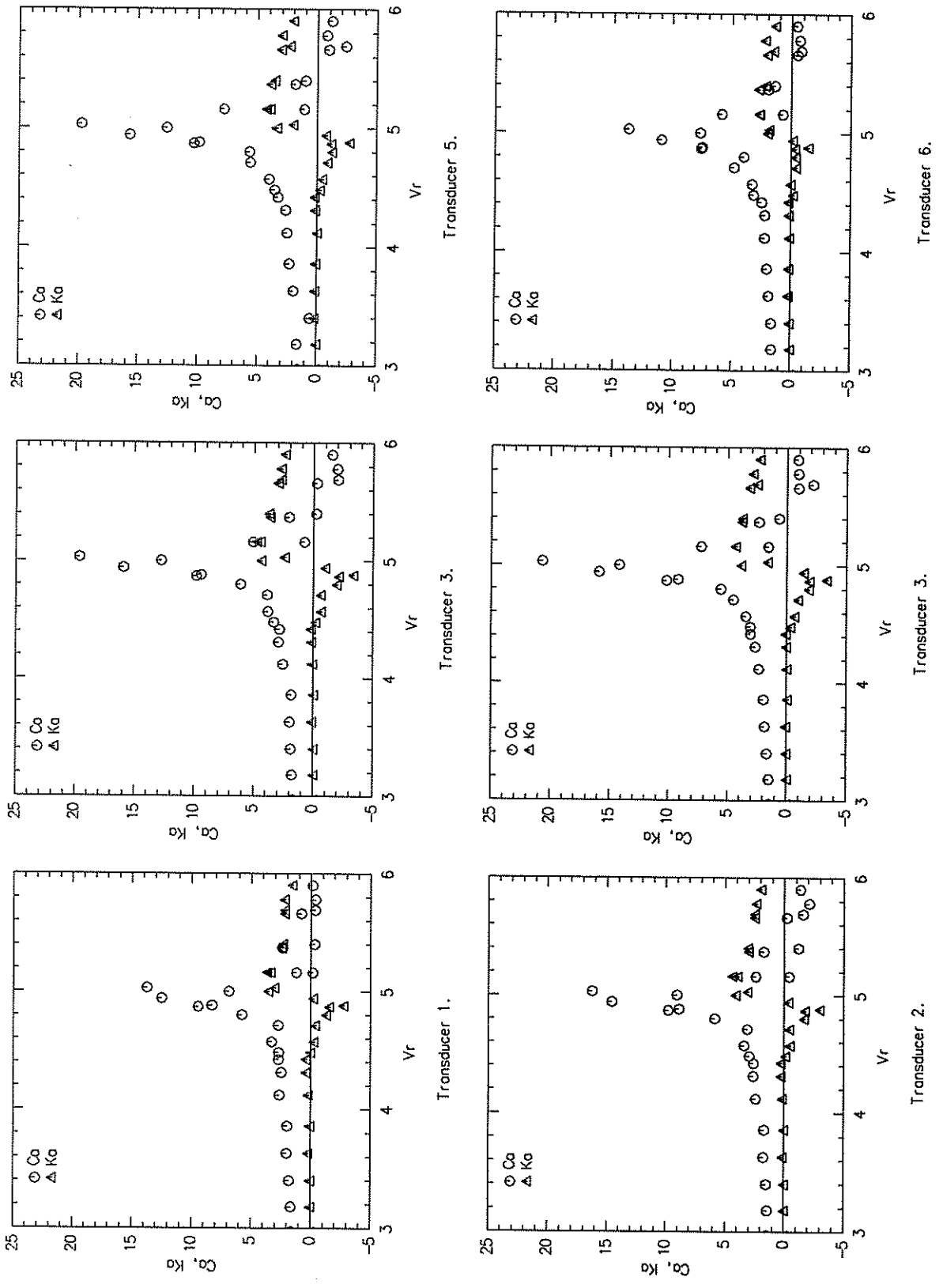

FIGURE 6.19: $\alpha_{\text{nom}} = 2\%$ Values of motion-correlated force parameters C_a and K_a as functions of reduced velocity in smooth subcritical flow. $Re = 1.6 \times 10^5$.

Smooth subcritical flow; $\alpha_{\text{nom}} = 3\%$

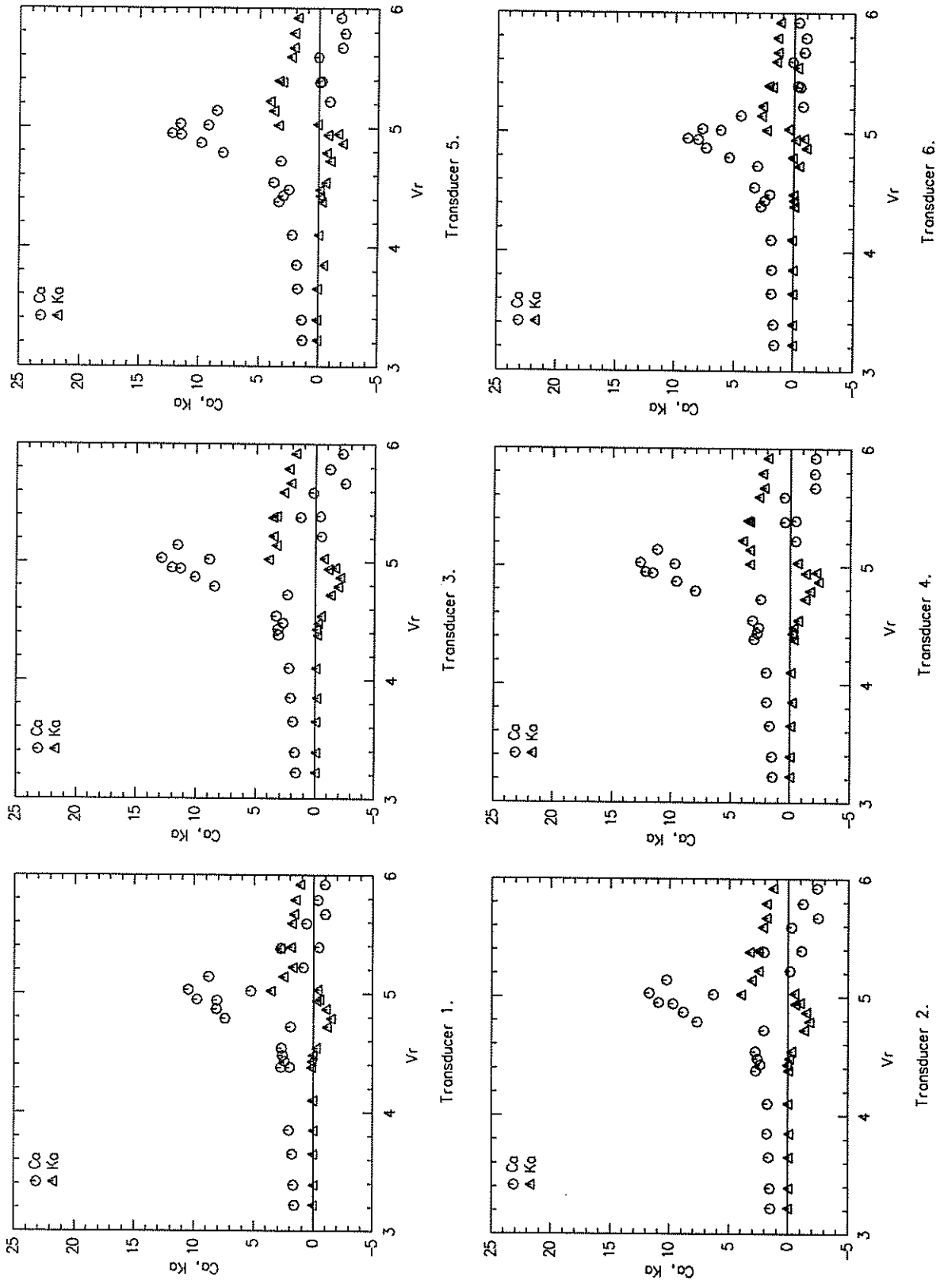

FIGURE 6.20: $\alpha_{\text{nom}} = 3\%$ Values of motion-correlated force parameters C_a and K_a as functions of reduced velocity in smooth subcritical flow. $Re = 1.6 \times 10^5$.

Turbulence configuration 1, $Re = 1.5 \times 10^5$, $\alpha_{\text{nom}} = 1\%$

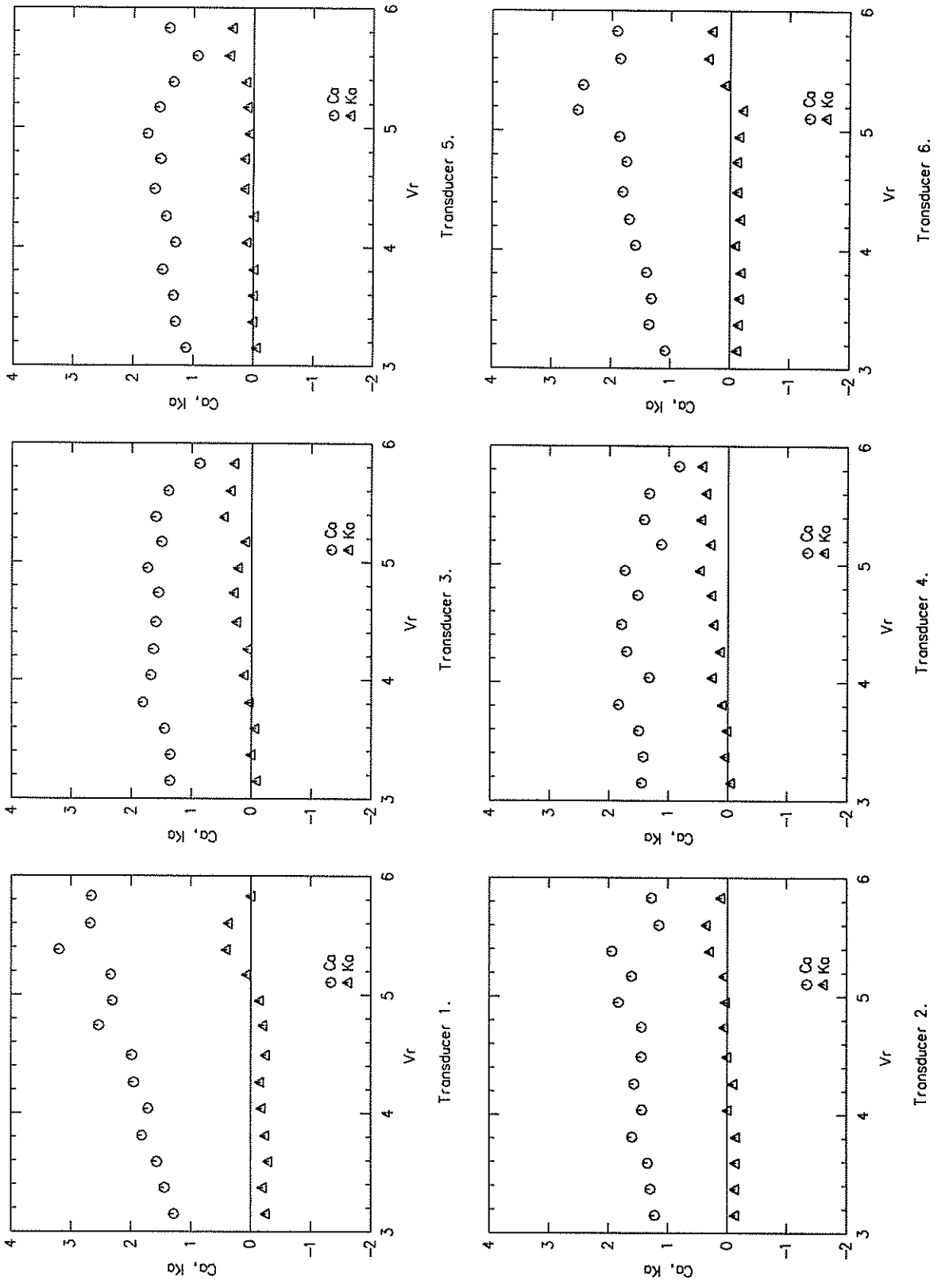

FIGURE 6.21: $\alpha_{\text{nom}} = 1\%$ Values of motion-correlated force parameters C_a and K_a as functions of reduced velocity in turbulence config. 1. $Re = 1.5 \times 10^5$.

Turbulence configuration 1, $Re = 1.5 \times 10^5$, $\alpha_{\text{nom}} = 2\%$

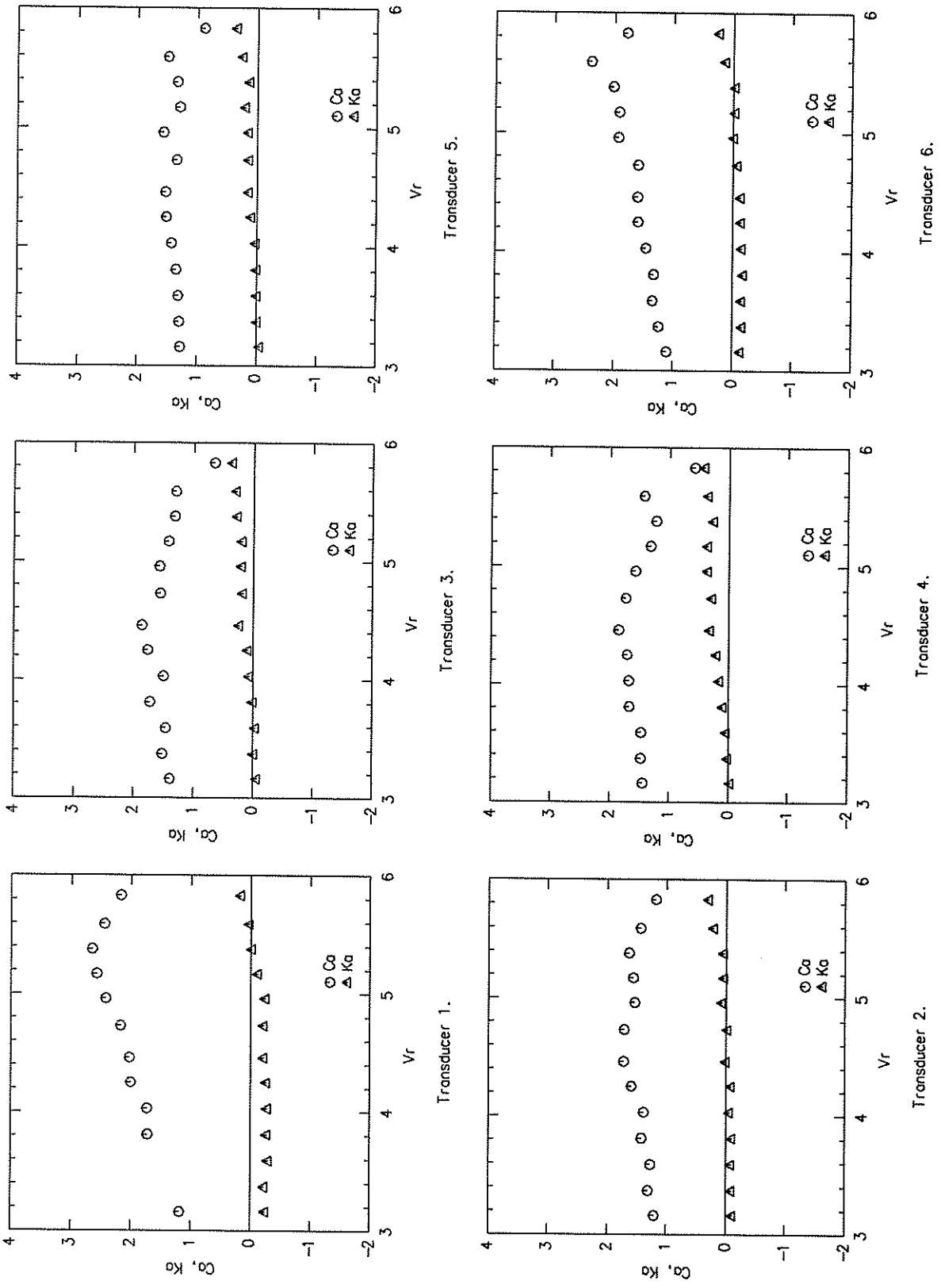

FIGURE 6.22: $\alpha_{\text{nom}} = 2\%$ Values of motion-correlated force parameters C_a and K_a as functions of reduced velocity in turbulence config. 1. $Re = 1.5 \times 10^5$.

Turbulence configuration 1, $Re = 1.5 \times 10^5$, $\alpha_{\text{nom}} = 3\%$

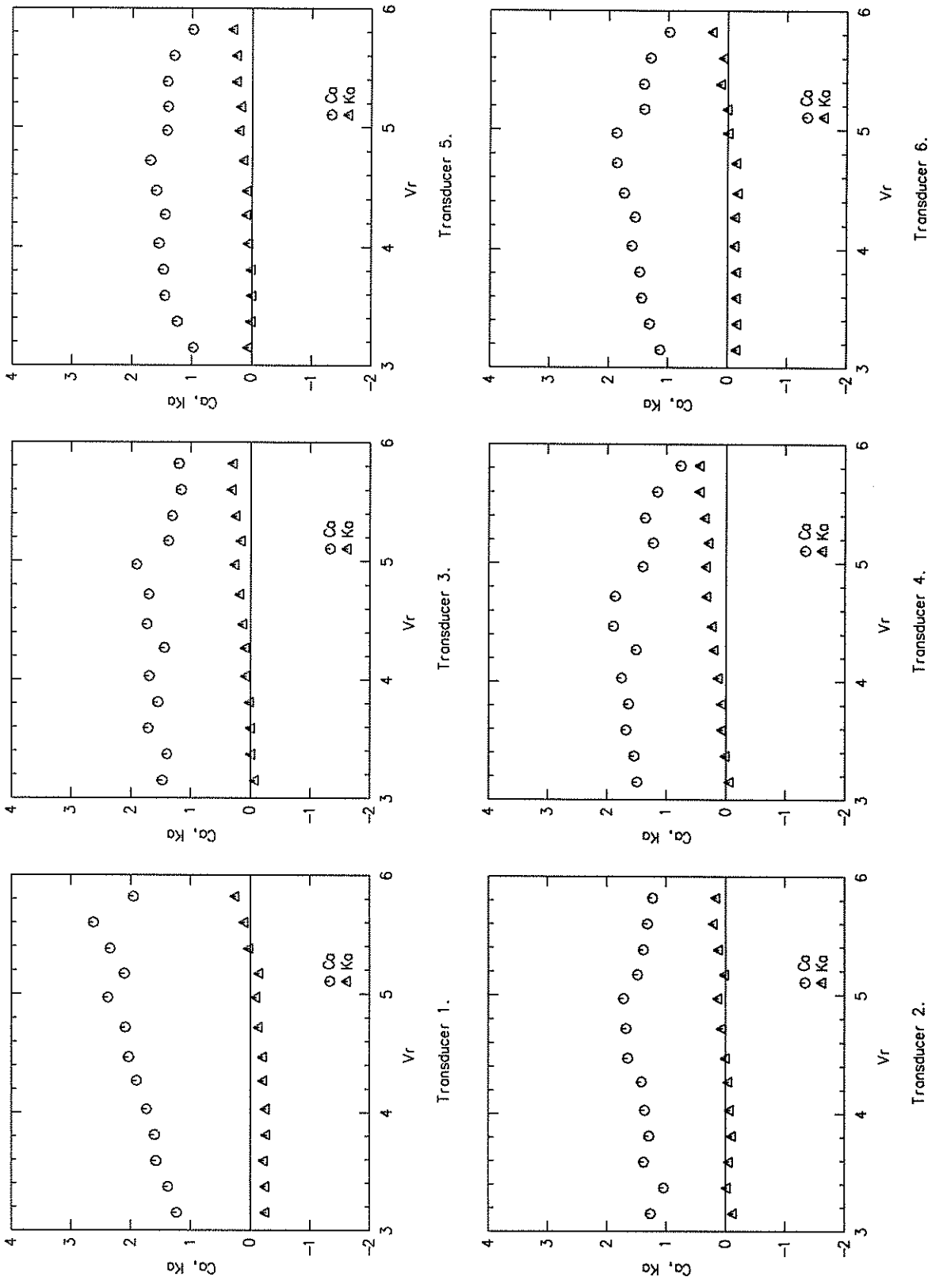

FIGURE 6.23: $\underline{\alpha_{\text{nom}} = 3\%}$ Values of motion-correlated force parameters C_a and K_a as functions of reduced velocity in turbulence config. 1. $Re = 1.5 \times 10^5$.

Turbulence configuration 2, $Re = 1.6 \times 10^5$, $\alpha_{\text{nom}} = 1\%$

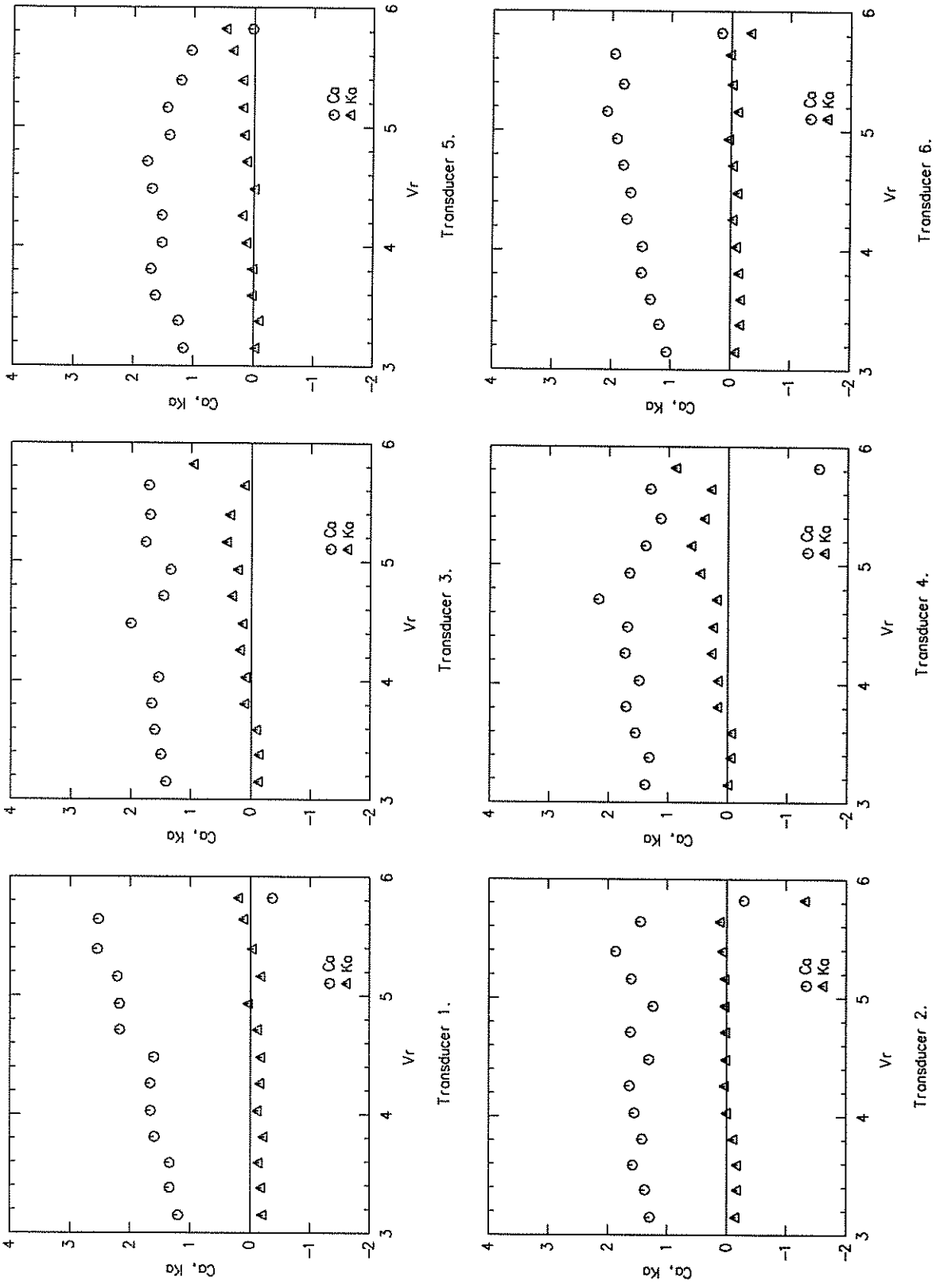

FIGURE 6.24: $\alpha_{\text{nom}} = 1\%$ Values of motion-correlated force parameters C_a and K_a as functions of reduced velocity in turbulence config. 2. $Re = 1.6 \times 10^5$.

Turbulence configuration 2, $Re = 1.6 \times 10^5$, $\alpha_{\text{nom}} = 2\%$

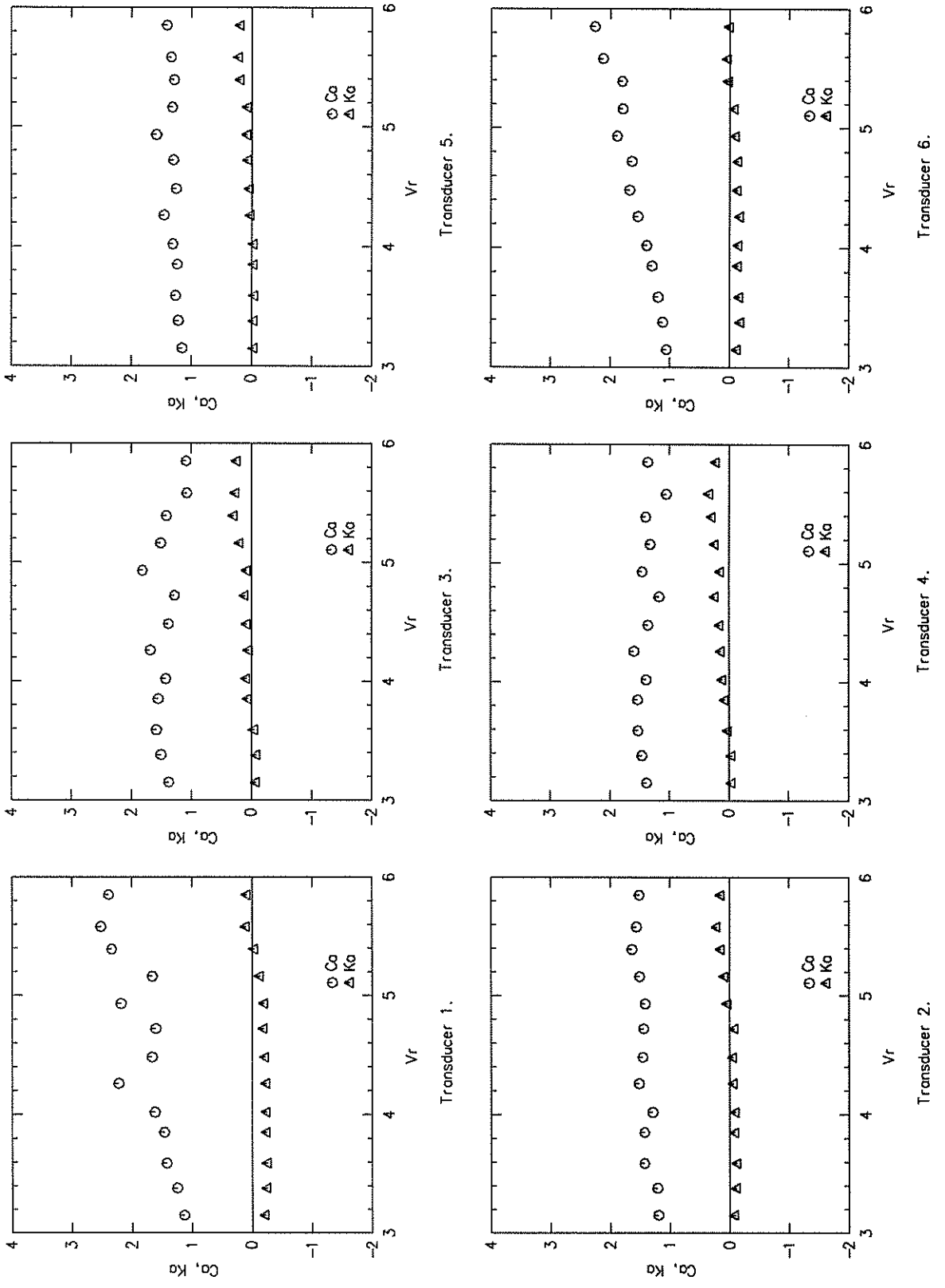

FIGURE 6.25: $\alpha_{\text{nom}} = 2\%$ Values of motion-correlated force parameters C_a and K_a as functions of reduced velocity in turbulence config. 2. $Re = 1.6 \times 10^5$.

Turbulence configuration 2, $Re = 1.6 \times 10^5$, $\alpha_{\text{nom}} = 3\%$

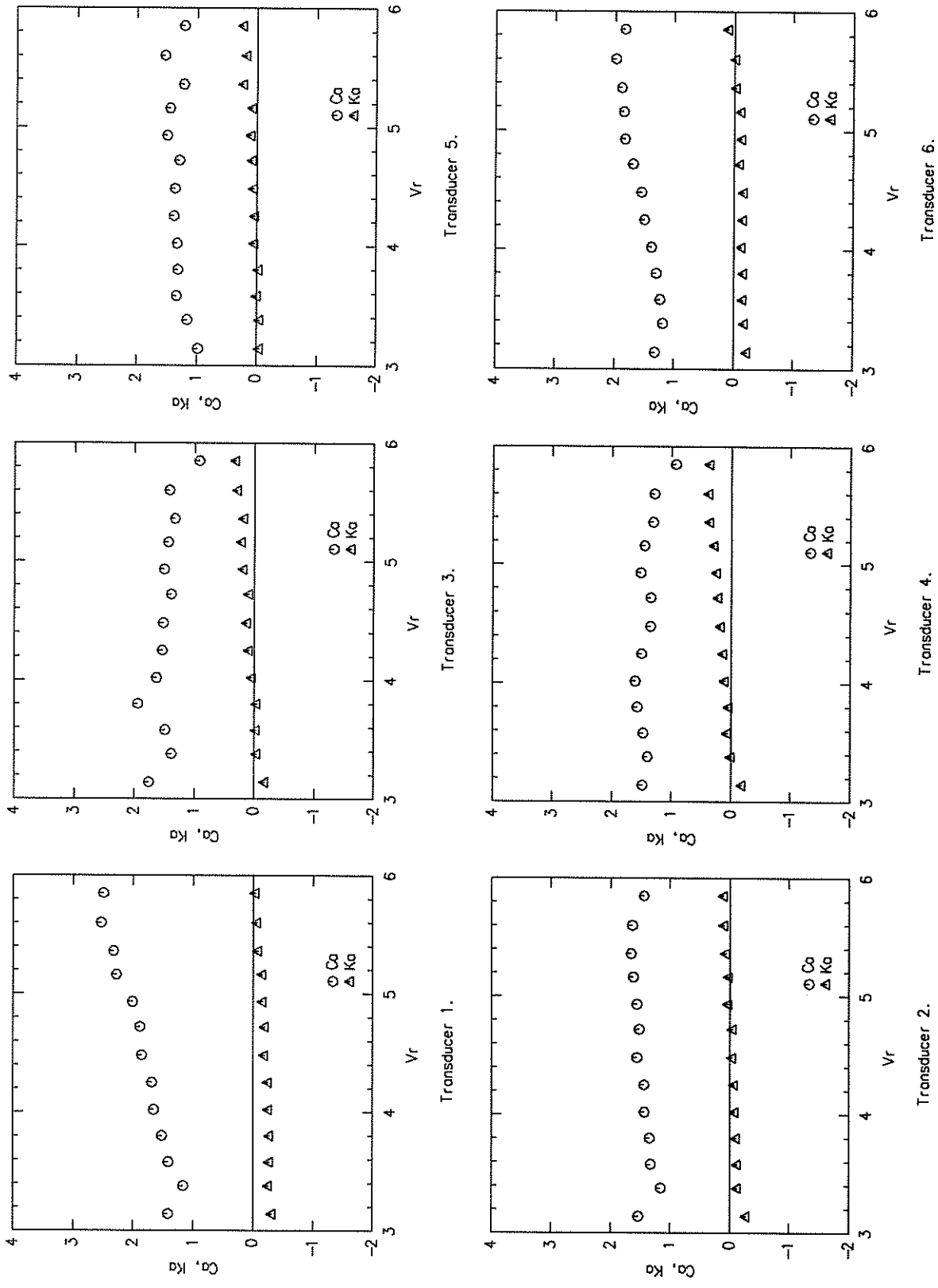

FIGURE 6.26: $\underline{\alpha_{\text{nom}} = 3\%}$ Values of motion-correlated force parameters C_a and K_a as functions of reduced velocity in turbulence config. 2. $Re = 1.6 \times 10^5$.

Turbulence configuration 3, $Re = 1.5 \times 10^5$, $\alpha_{\text{nom}} = 1\%$

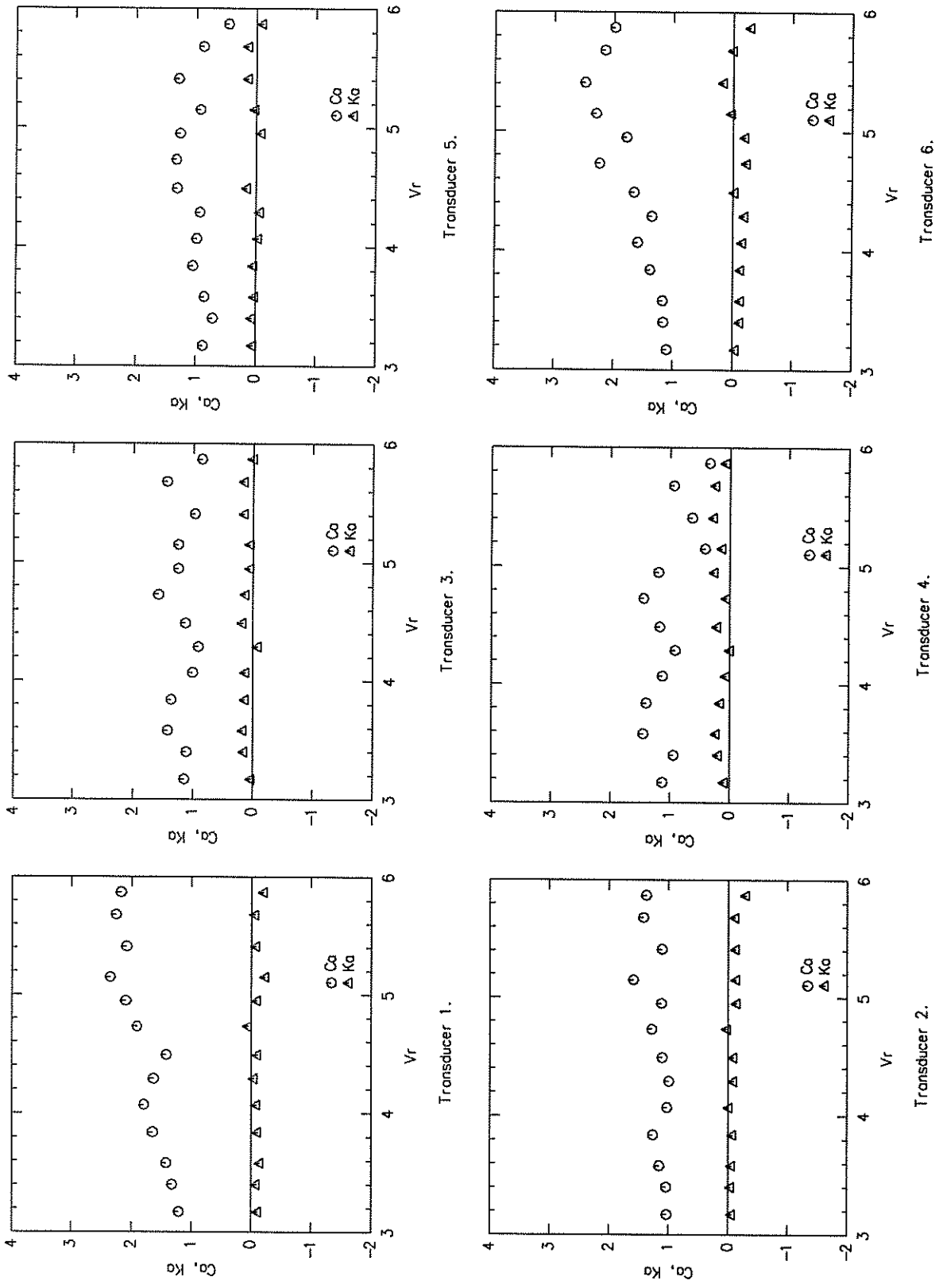

FIGURE 6.27: $\alpha_{\text{nom}} = 1\%$ Values of motion-correlated force parameters C_a and K_a as functions of reduced velocity in turbulence config. 3. $Re = 1.5 \times 10^5$.

Turbulence configuration 3, $Re = 1.5 \times 10^5$, $\alpha_{\text{nom}} = 2\%$

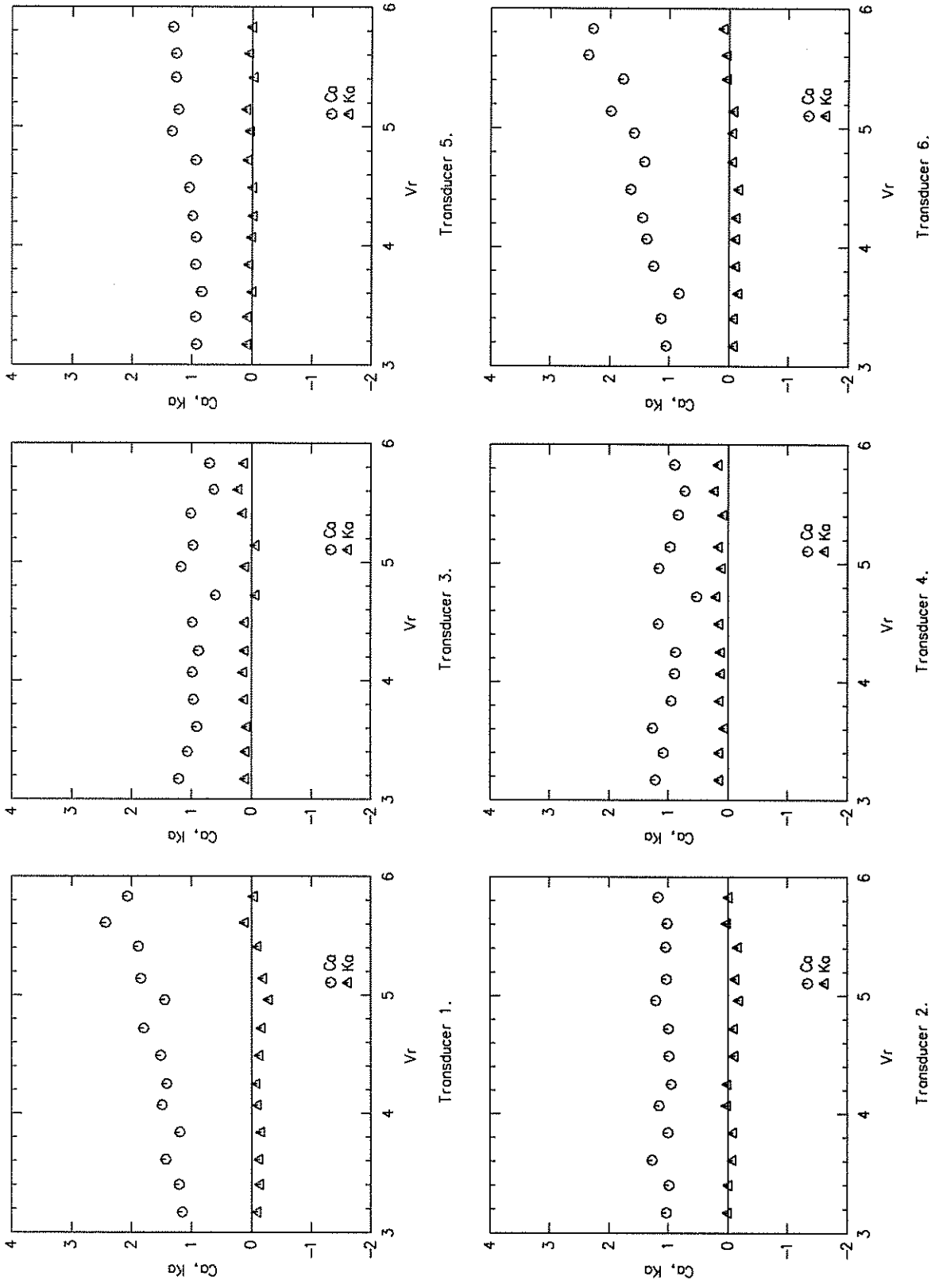

FIGURE 6.28: $\alpha_{\text{nom}} = 2\%$ Values of motion-correlated force parameters C_a and K_a as functions of reduced velocity in turbulence config. 3. $Re = 1.5 \times 10^5$.

Turbulence configuration 3, $Re = 1.5 \times 10^5$, $\alpha_{\text{nom}} = 3\%$

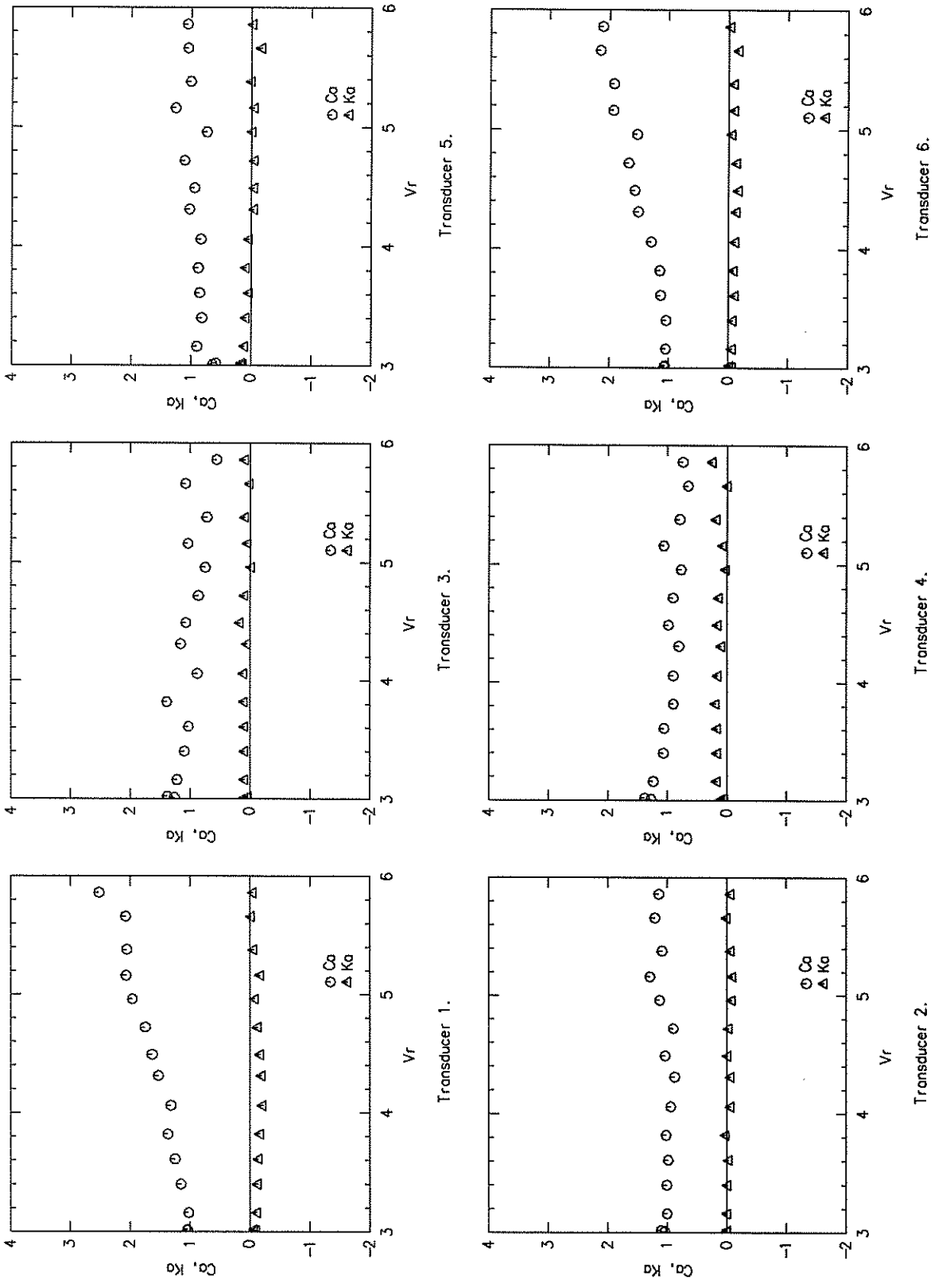

FIGURE 6.29: $\underline{\alpha_{\text{nom}} = 3\%}$ Values of motion-correlated force parameters C_a and K_a as functions of reduced velocity in turbulence config. 3. $Re = 1.5 \times 10^5$.

Turbulence configuration 4, $Re = 1.5 \times 10^5$, $\alpha_{\text{nom}} = 1\%$

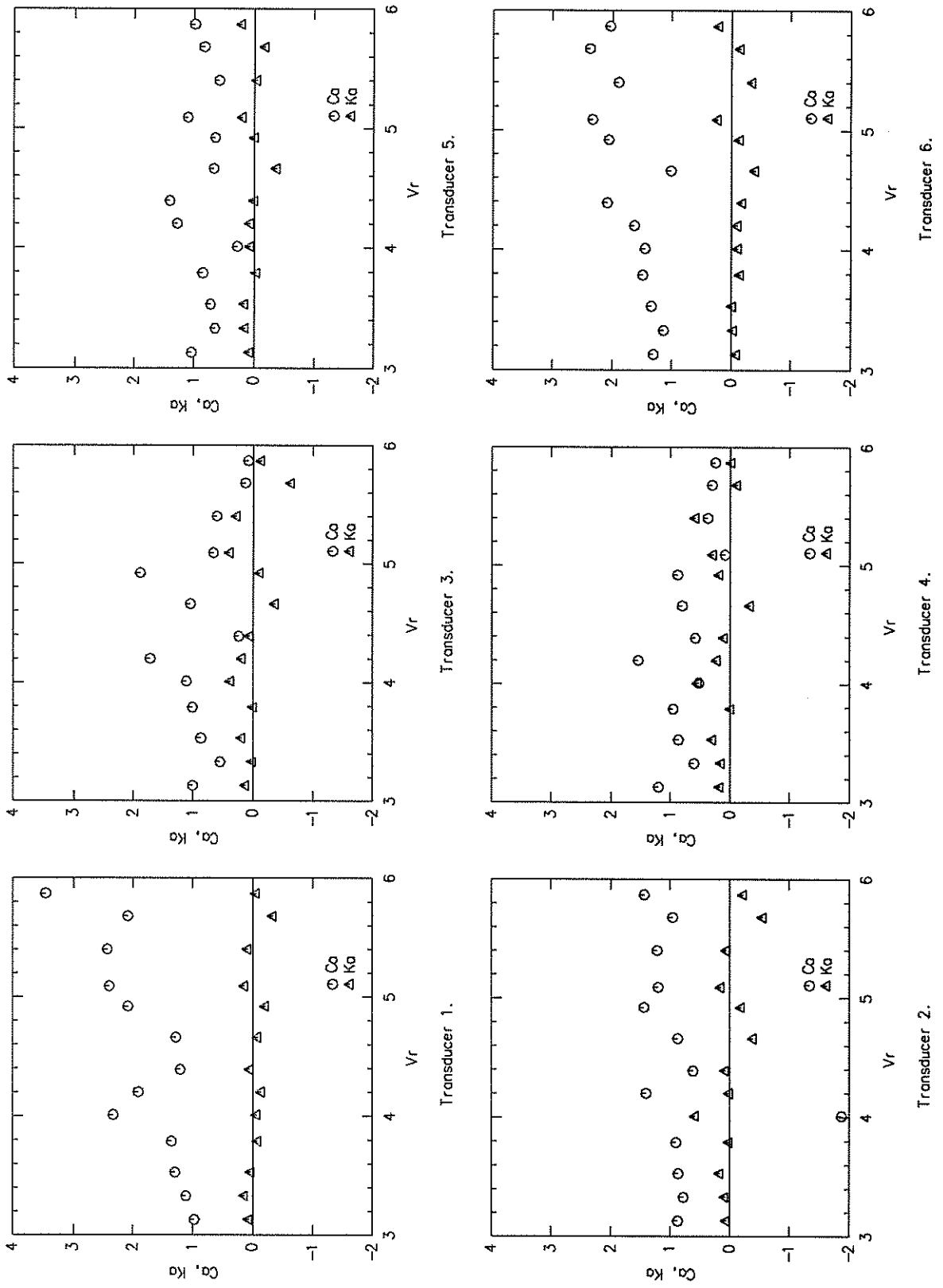

FIGURE 6.30: $\alpha_{\text{nom}} = 1\%$ Values of motion-correlated force parameters C_a and K_a as functions of reduced velocity in turbulence config. 4. $Re = 1.5 \times 10^5$.

Turbulence configuration 4, $Re = 1.5 \times 10^5$, $\alpha_{\text{nom}} = 2\%$

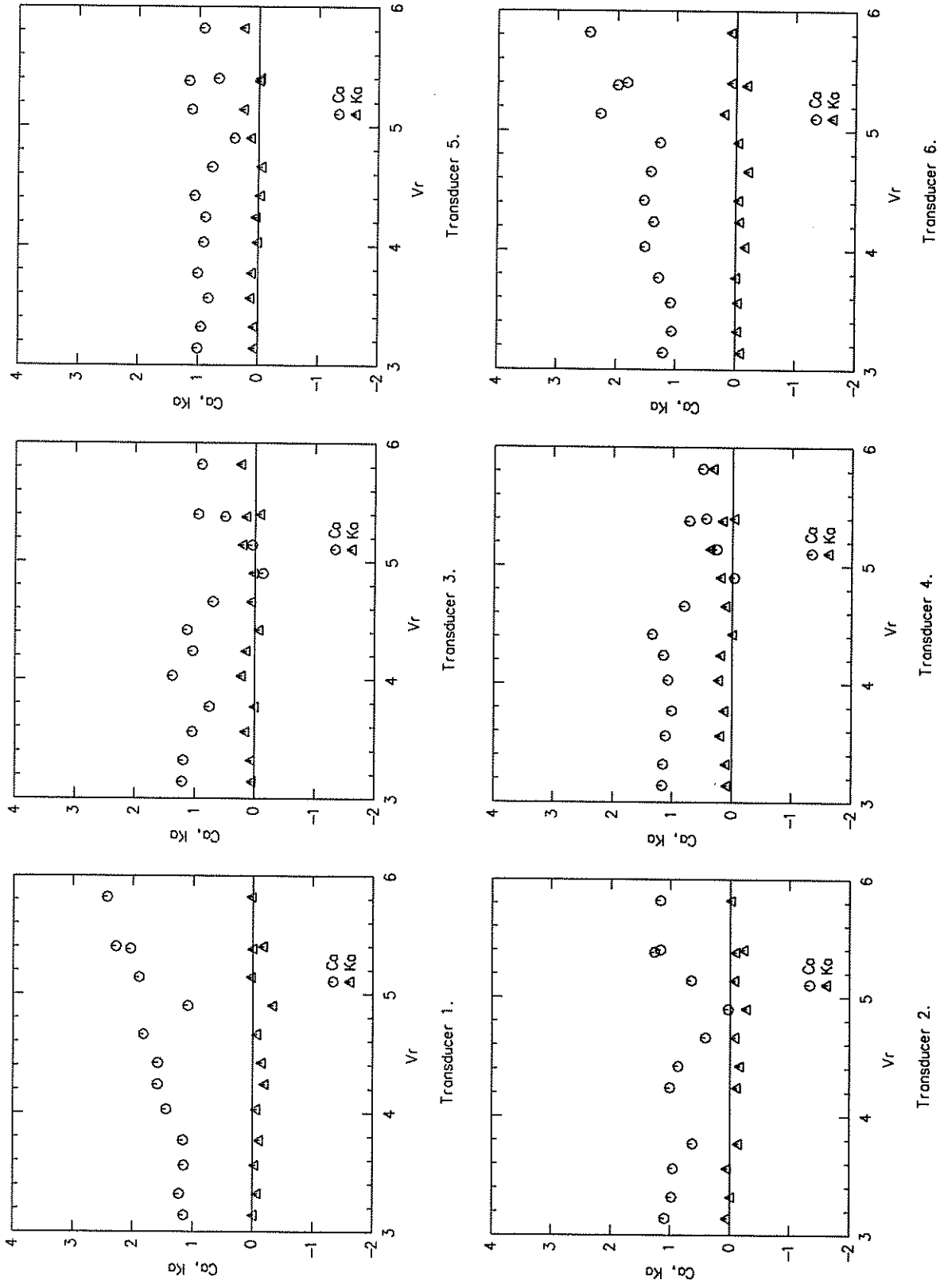

FIGURE 6.31: $\alpha_{\text{nom}} = 2\%$ Values of motion-correlated force parameters C_a and K_a as functions of reduced velocity in turbulence config. 4. $Re = 1.5 \times 10^5$.

Turbulence configuration 4, $Re = 1.5 \times 10^5$, $\alpha_{\text{nom}} = 3\%$

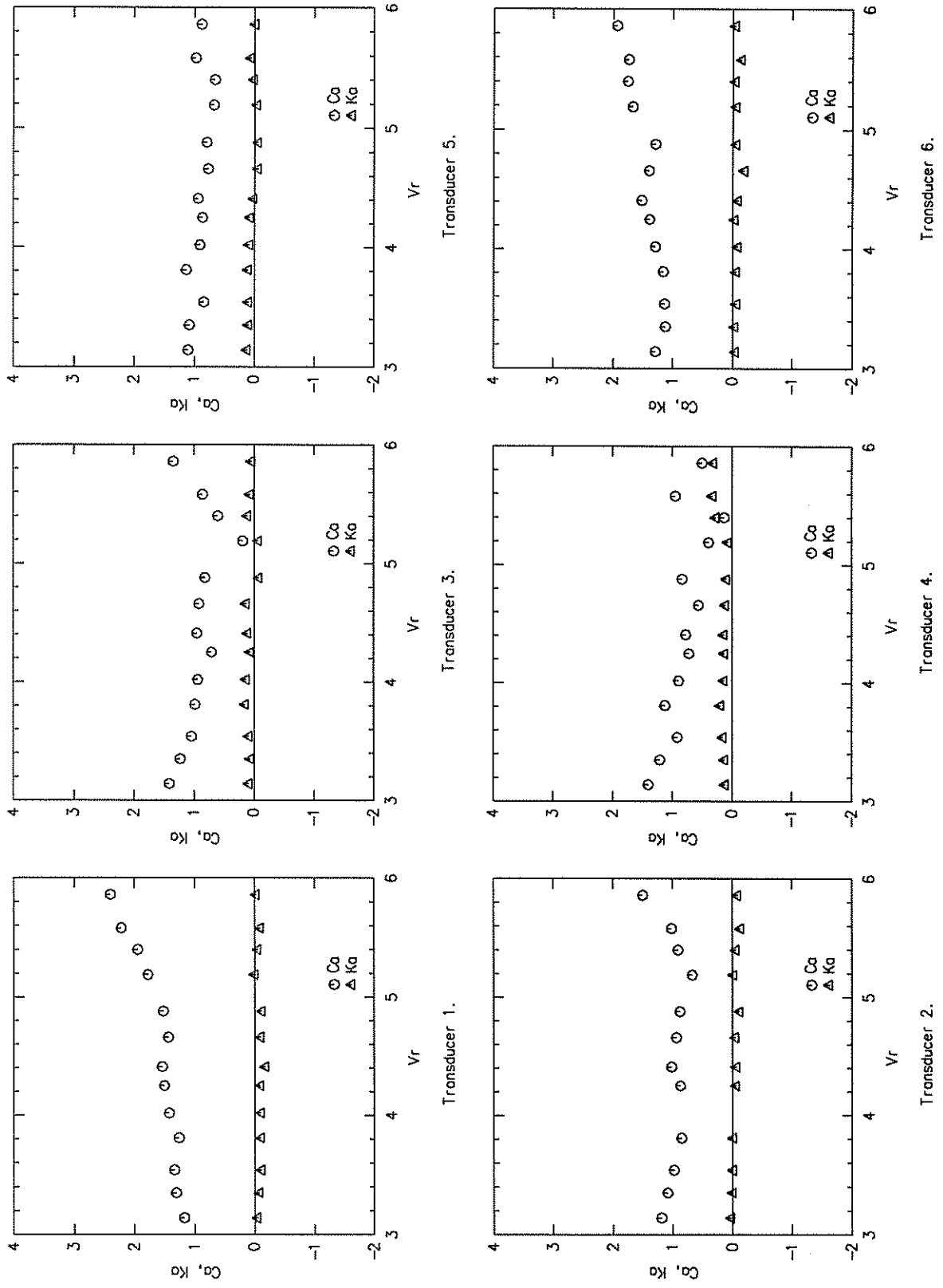

FIGURE 6.32: $\underline{\alpha_{\text{nom}} = 3\%}$ Values of motion-correlated force parameters C_a and K_a as functions of reduced velocity in turbulence config. 4. $Re = 1.5 \times 10^5$.

6.5.3 High Reynolds number results

In this series of tests, the Reynolds number was maintained near 5×10^5. A range of oscillation frequencies from about 35 Hz to 50 Hz was employed to produce a range of reduced velocities from 3.5 to 5.5. In many cases, the highest amplitude that could be achieved was a little over 2% of cylinder diameter due to the limited power capacity of the electromagnetic shaker, particularly at the high end of the frequency range. Consequently only results for $\alpha_{\text{nom}} = 1\%$ and $\alpha_{\text{nom}} = 2\%$ are presented.

Smooth flow, $Re = 4.6 \times 10^5$, $\alpha_{\text{nom}} = 1\%$

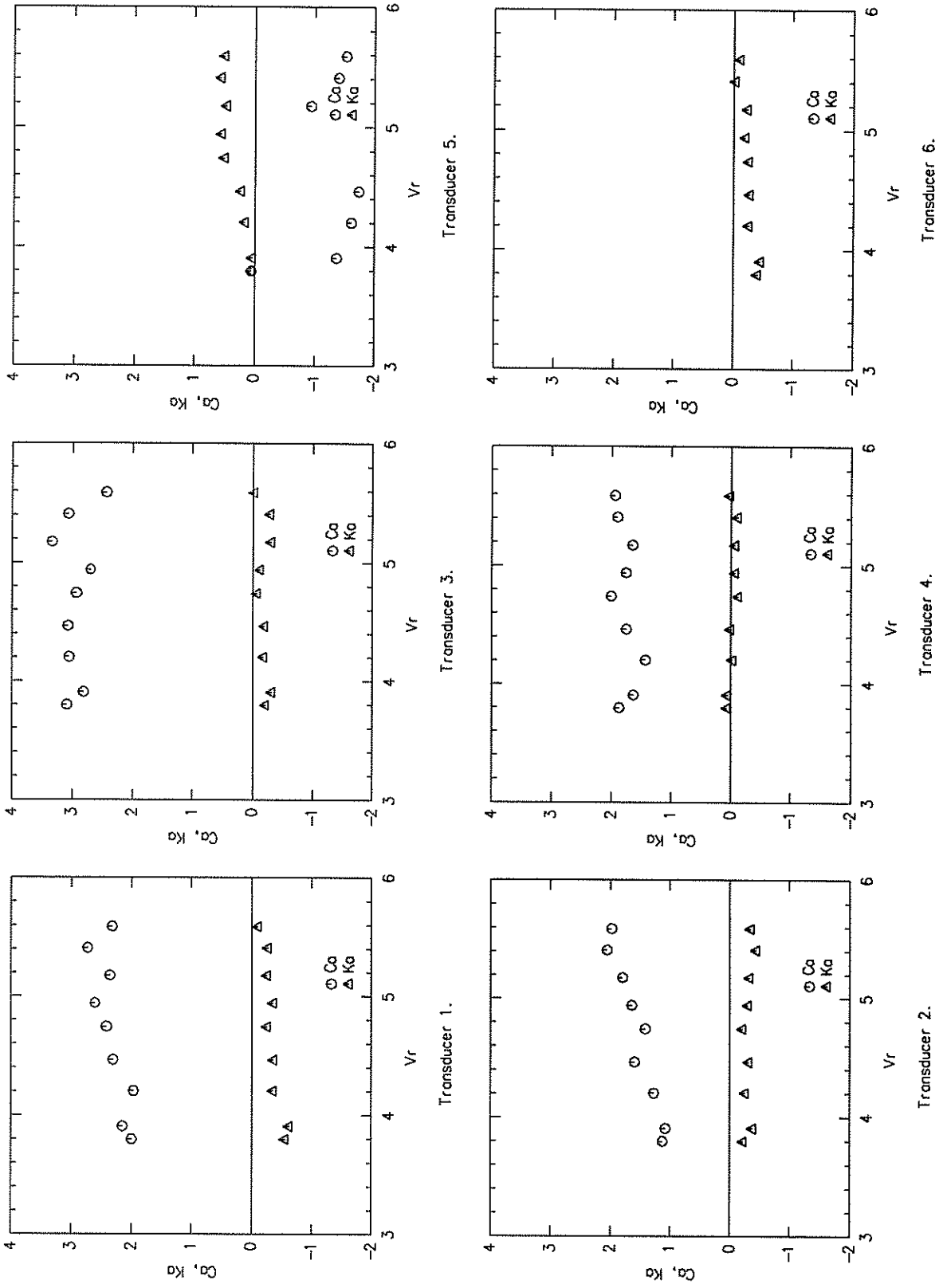

FIGURE 6.33: $\alpha_{\text{nom}} = 1\%$ Values of motion-correlated force parameters C_a and K_a as functions of reduced velocity in smooth flow. $Re = 4.6 \times 10^5$.

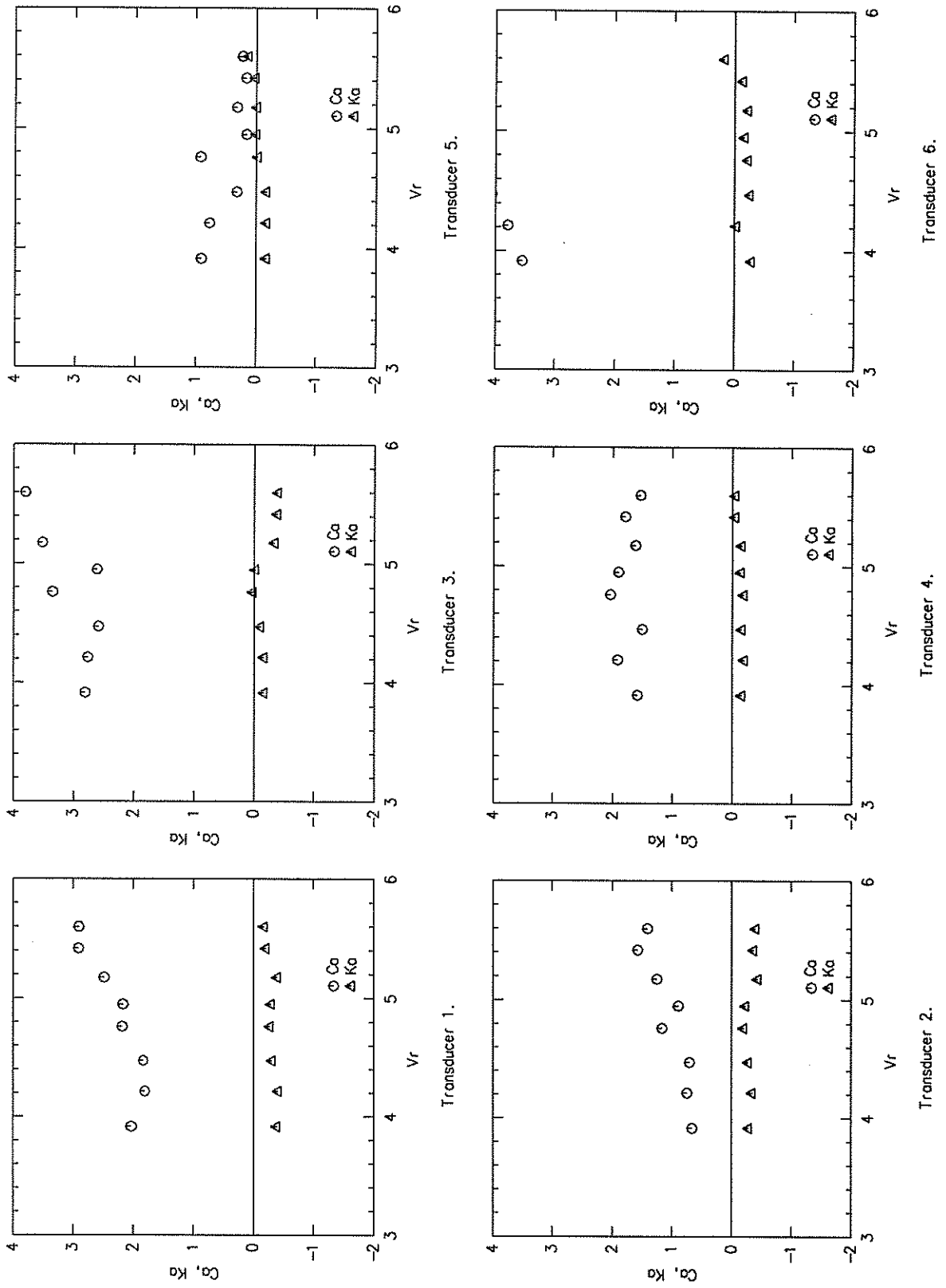

FIGURE 6.34: $\alpha_{nom} = 2\%$ Values of motion-correlated force parameters C_a and K_a as functions of reduced velocity in smooth flow. $Re = 4.6 \times 10^5$.

Configuration 1, $Re = 5.0 \times 10^5$, $\alpha_{\text{nom}} = 1\%$

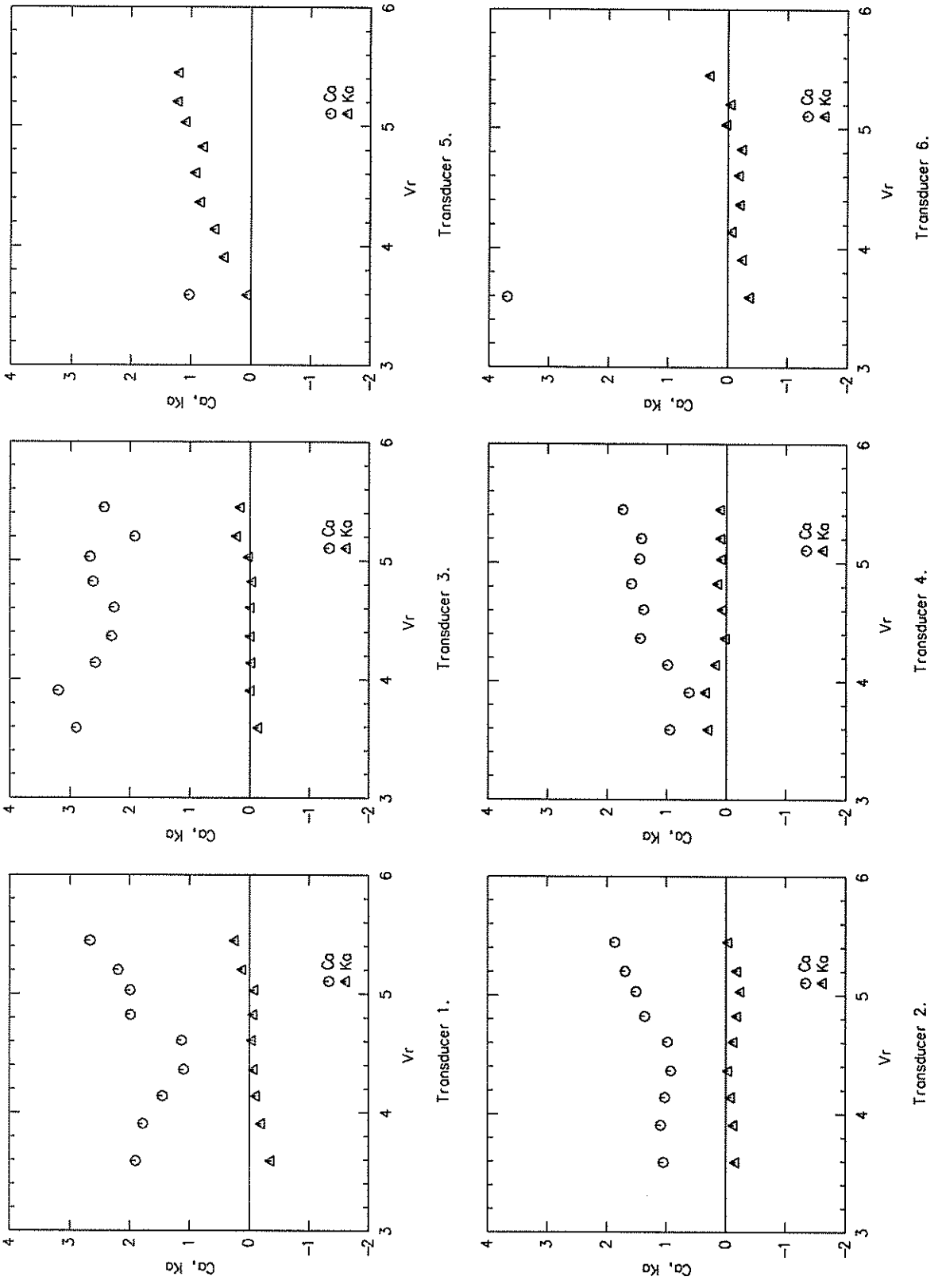

FIGURE 6.35: $\alpha_{\text{nom}} = 1\%$ Values of motion-correlated force parameters C_a and K_a as functions of reduced velocity in turbulence config. 1. $Re = 5.0 \times 10^5$.

Configuration 1, $Re = 5.0 \times 10^5$, $\alpha_{\text{nom}} = 2\%$

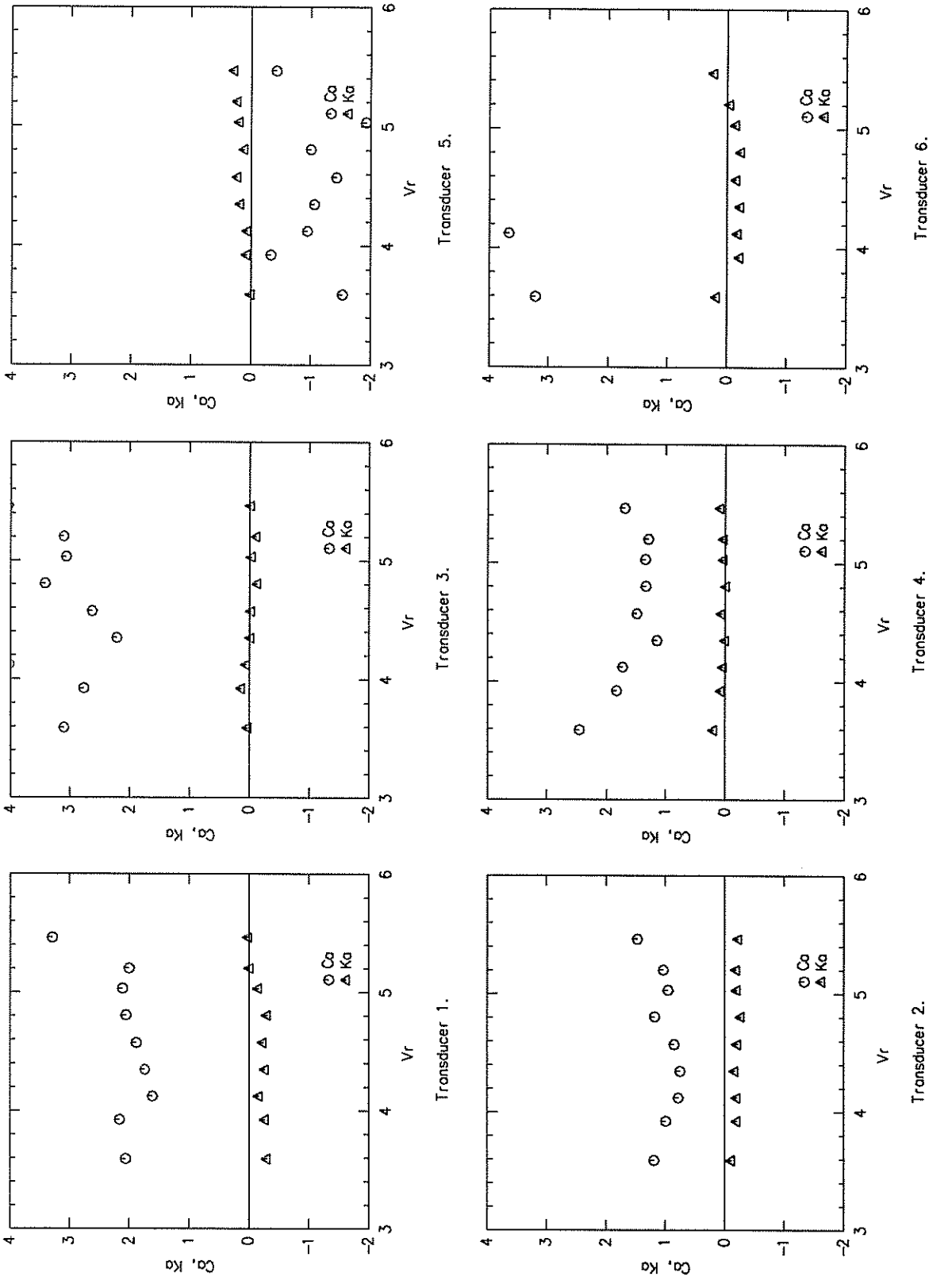

FIGURE 6.36: $\alpha_{\text{nom}} = 2\%$ Values of motion-correlated force parameters C_a and K_a as functions of reduced velocity in turbulence config. 1. $Re = 5.0 \times 10^5$.

Configuration 2, $Re = 4.4 \times 10^5$, $\alpha_{\text{nom}} = 1\%$

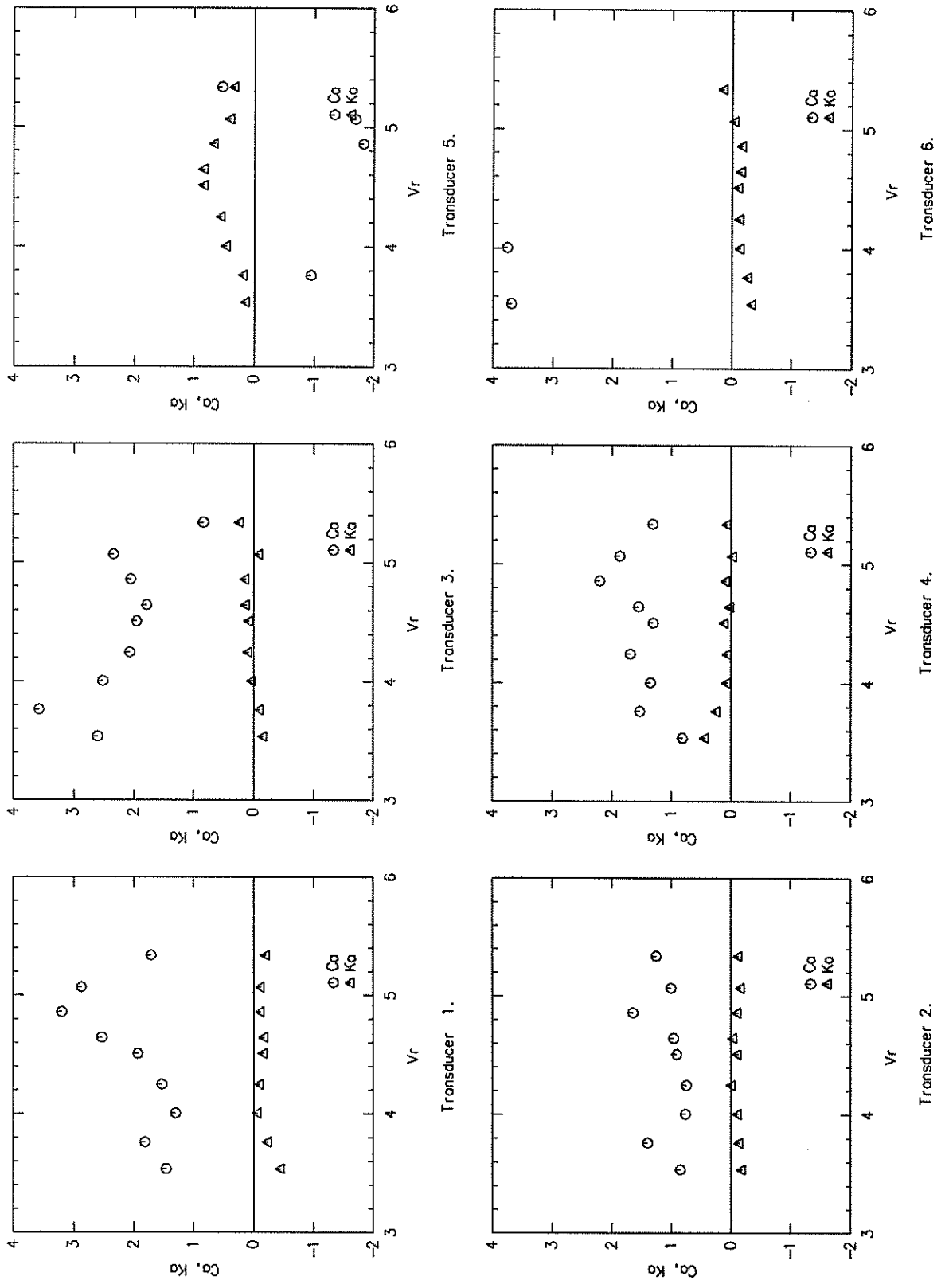

FIGURE 6.37: $\underline{\alpha_{\text{nom}} = 1\%}$ Values of motion-correlated force parameters C_a and K_a as functions of reduced velocity in turbulence config. 2. $Re = 4.4 \times 10^5$.

Configuration 2, $Re = 4.4 \times 10^5$, $\alpha_{\text{nom}} = 2\%$

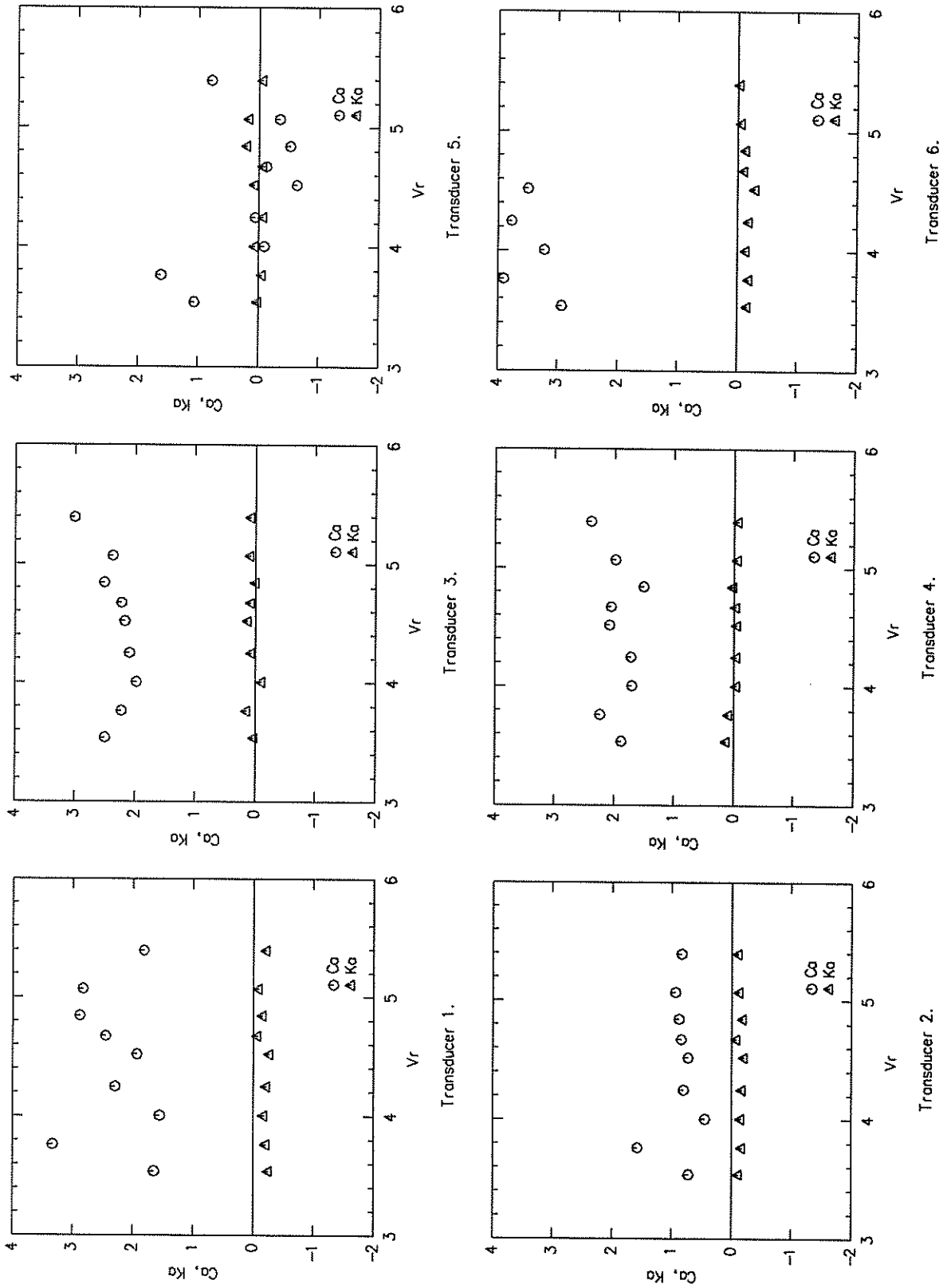

FIGURE 6.38: $\alpha_{\text{nom}} = 2\%$ Values of motion-correlated force parameters C_a and K_a as functions of reduced velocity in turbulence config. 2. $Re = 4.4 \times 10^5$.

Configuration 3, $Re = 4.4 \times 10^5$, $\alpha_{\text{nom}} = 1\%$

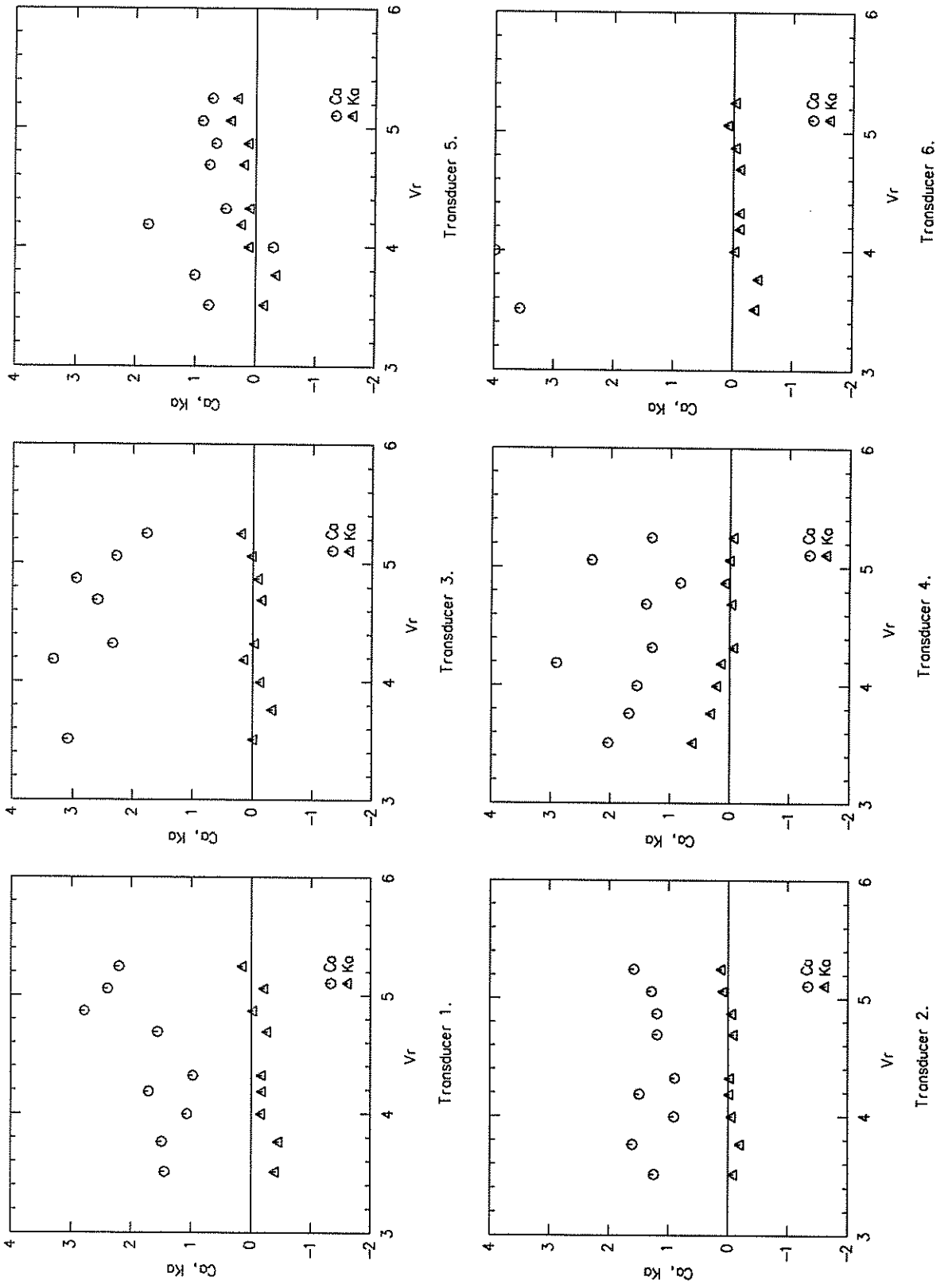

FIGURE 6.39: $\underline{\alpha_{\text{nom}} = 1\%}$ Values of motion-correlated force parameters C_a and K_a as functions of reduced velocity in turbulence config. 3. $Re = 4.4 \times 10^5$.

Configuration 3, $Re = 4.4 \times 10^5$, $\alpha_{\text{nom}} = 2\%$

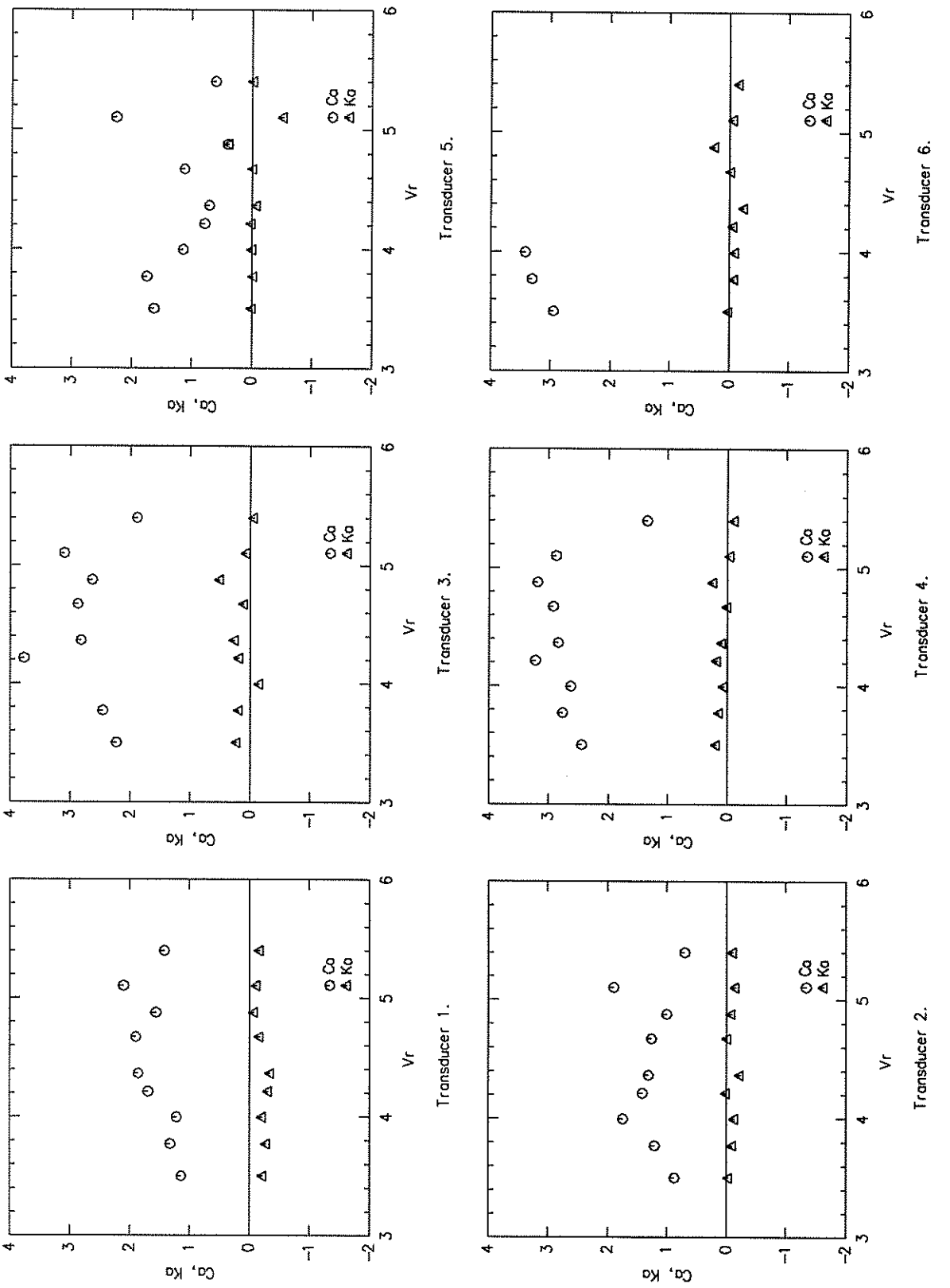

FIGURE 6.40: $\alpha_{\text{nom}} = 2\%$ Values of motion-correlated force parameters C_a and K_a as functions of reduced velocity in turbulence config. 3. $Re = 4.4 \times 10^5$.

Configuration 4, $Re = 4.9 \times 10^5$, $\alpha_{\text{nom}} = 1\%$

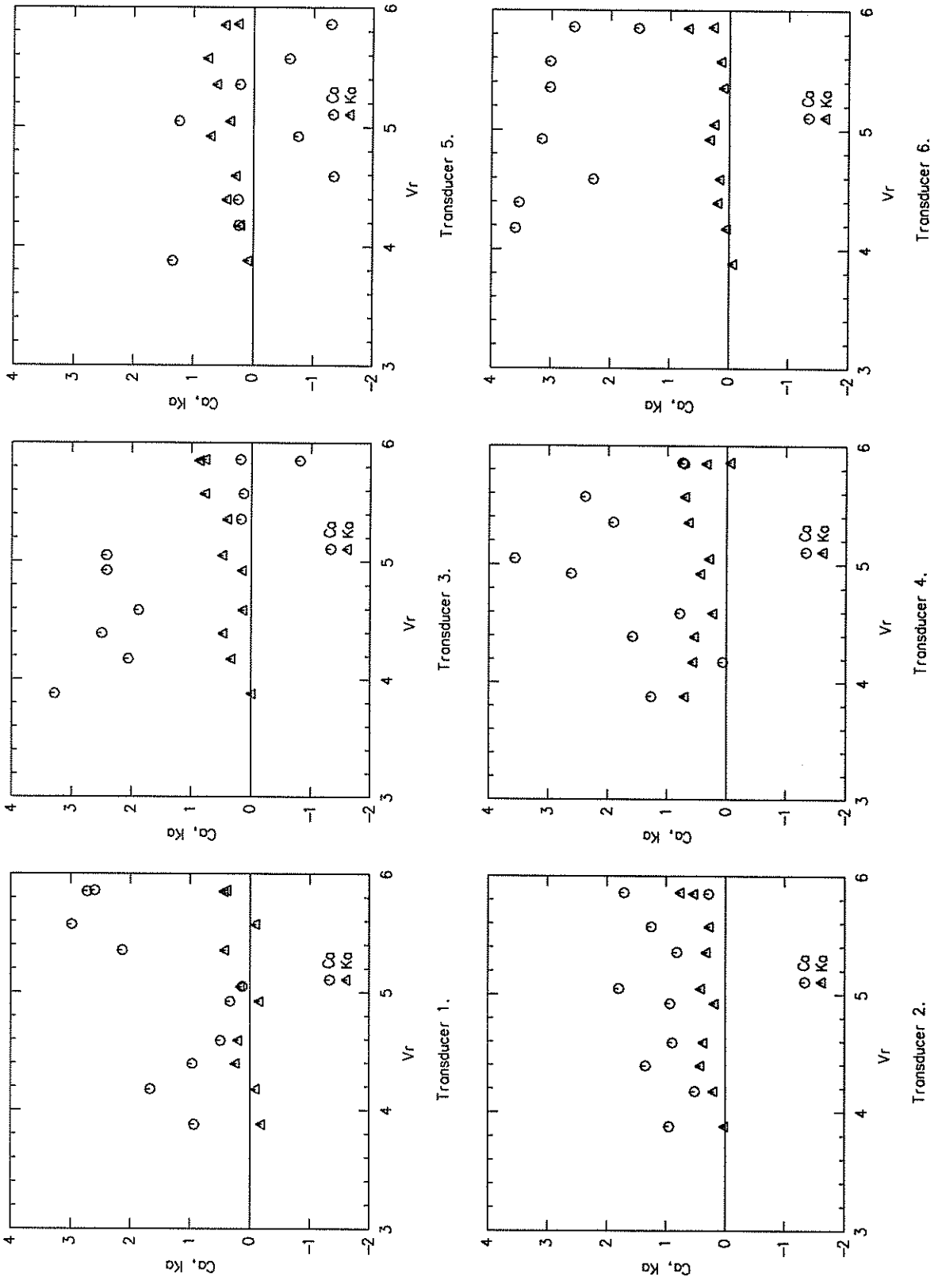

FIGURE 6.41: $\alpha_{\text{nom}} = 1\%$ Values of motion-correlated force parameters C_a and K_a as functions of reduced velocity in turbulence config. 4. $Re = 4.9 \times 10^5$.

Configuration 4, $Re = 4.9 \times 10^5$, $\alpha_{\text{nom}} = 2\%$

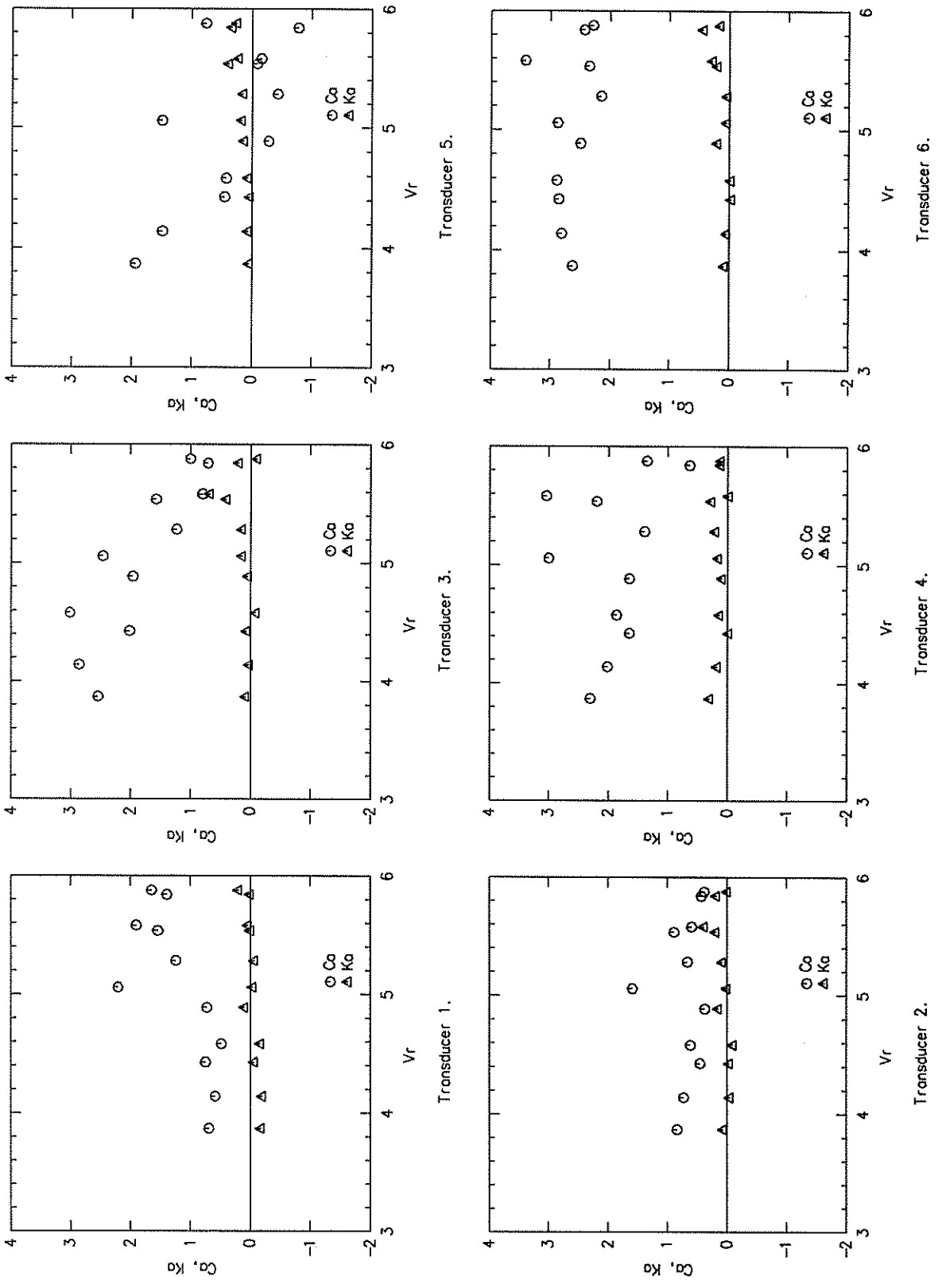

FIGURE 6.42: $\alpha_{\text{nom}} = 2\%$ Values of motion-correlated force parameters C_a and K_a as functions of reduced velocity in turbulence config. 4. $Re = 4.9 \times 10^5$.

6.5.4 Discussion

Smooth subcritical flow

The most distinctive changes of motion-correlated forces with reduced velocity were produced in smooth subcritical flow (figs. 6.18, 6.19, 6.20). In addition, the largest values and greatest spanwise uniformity of the motion-correlated force coefficients occurred in that flow. The average values of the coefficients C_a and K_a obtained at the four most central transducers on the model are presented in figure 6.43. All curves have the same general shape, while the magnitudes of coefficients found at any V_r decreased somewhat as amplitude of oscillation increased. The values of motion-correlated force coefficients near $V_r = 5$ fell as the amplitude of cylinder oscillation was increased, with peak values of the coefficients falling by about a third as the nominal amplitude of oscillation increased from 1% to 3% of diameter. Estimates of the peak positive values of C_a and K_a obtained from figure 6.43 are shown as functions of motion amplitude in figure 6.44. It can be seen that there was an approximately linear drop in both coefficients with amplitude; fitted lines indicate the following values: $C_{a0} = 27.5$, $K_{a0} = 6.5$, $\partial C_a/\partial\alpha = -430$, $\partial K_a/\partial\alpha = -85$.

The changes in C_a and K_a with reduced velocity were in general similar to previously published results, as reviewed in chapter 1 of this thesis. Two experiments in which both C_a and K_a (or their equivalents) were measured in smooth subcritical flows are those of Nakamura, Kaku and Mizota (1971, ch. 1, fig. 1.58) and Sarpkaya (1978, ch. 1, figs. 1.61 & 1.62). The similarity in form of the first of these two sets of results to those presented here is striking, particularly with respect to the sharp peak in the values of C_a at the values of reduced velocity where K_a changed sign.

The magnitudes of the coefficients were amongst the largest of the values observed to date. A comparison of the largest positive values of the coefficient K_a found in the survey carried out in chapter 1 with that observed at $\alpha_{\text{nom}} = 3\%$ in this experimental programme is presented in figure 6.45. While there is a large amount of variation in the peak values of K_a observed in the different experiments, it seems that the variation of K_a with Reynolds number follows the trend in coefficient of lift for a stationary cylinder. One has to bear in mind that K_a may be a function of α as well as V_r and Re, and that this may account for some of the variation in values from experiments at similar Reynolds numbers. It is encouraging to note that the result of Förscher (1968), which was obtained at a similar Reynolds number, provides the closest agreement of any of the other experimental results.

Apart from the possible variations in K_a produced by changes in α and Re, it seems likely that the comparatively high value of K_a (approximately 4 in the present experimental results) may have been partly brought about by the comparatively low cylinder aspect ratio and moderate wind tunnel blockage, as was thought to be the case for measurements of σ_{C_l} obtained with the cylinder fixed (see § 5.3.2). If it can be assumed that values of motion-correlated lift force are approximately proportional to values of sectional σ_{C_l}, then the values of K_a measured here in smooth subcritical flows were larger by a factor of approximately two than those appropriate to a high aspect ratio cylinder in low blockage flow.

The spanwise correlation of the motion-correlated forces is of interest. It is often as-

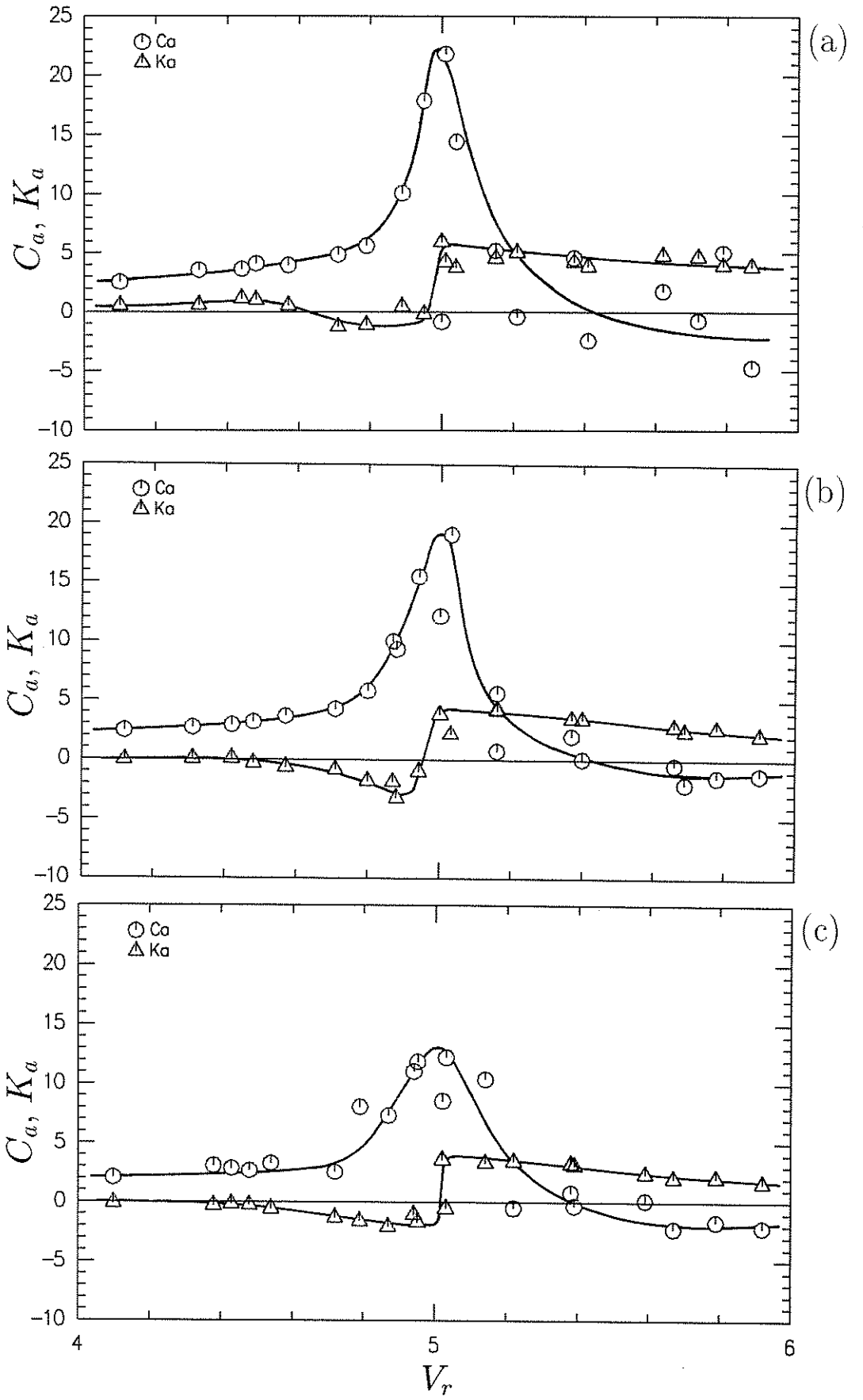

FIGURE 6.43: Averages of the values of C_a and K_a obtained at the model's four most central transducers as functions of V_r. (a); $\alpha \simeq 0.98\%$. (b); $\alpha \simeq 1.89\%$. (c); $\alpha \simeq 2.71\%$.

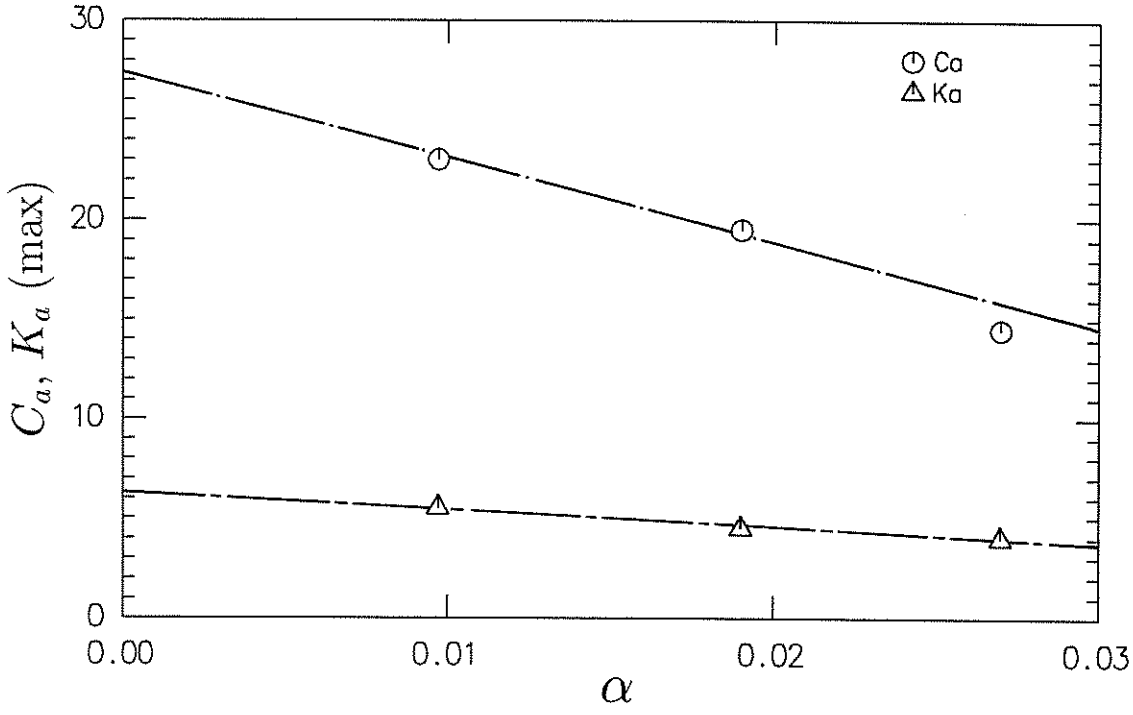

FIGURE 6.44: Peak values of C_a and K_a as functions of amplitude α, with fitted lines.

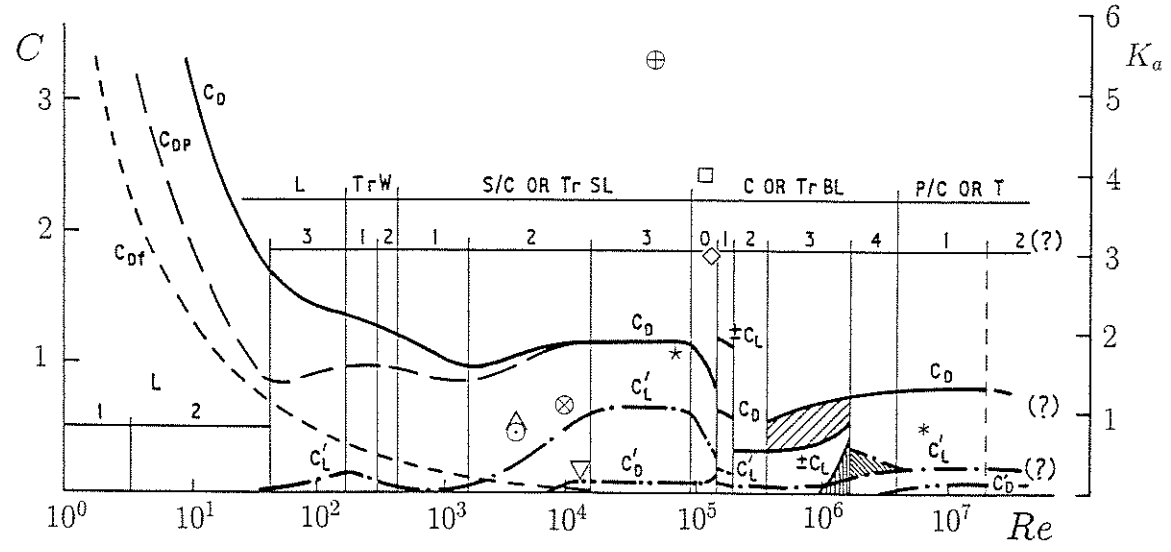

FIGURE 6.45: Comparison of peak values of K_a measured in smooth flow by different experimenters. The diagram of variation of fixed cylinder force coefficients with Reynolds number produced by Zdravkovich (1990) is used as a backdrop. □; Present work; $\alpha_{\text{nom}} = 3\%$. ⊕; Protos, Goldschmidt & Toebes (1968). ◇; Försching (1968). ∗; Jones, Cincotta & Walker (1969). ⊗; Nakamura, Kaku & Mizota (1971). ⋆; Yano & Takahara (1971). ⊙; Tanida, Okajima & Watanabe (1973). ▽; Sarpkaya (1978). △; Middlin & Simmons (1983).

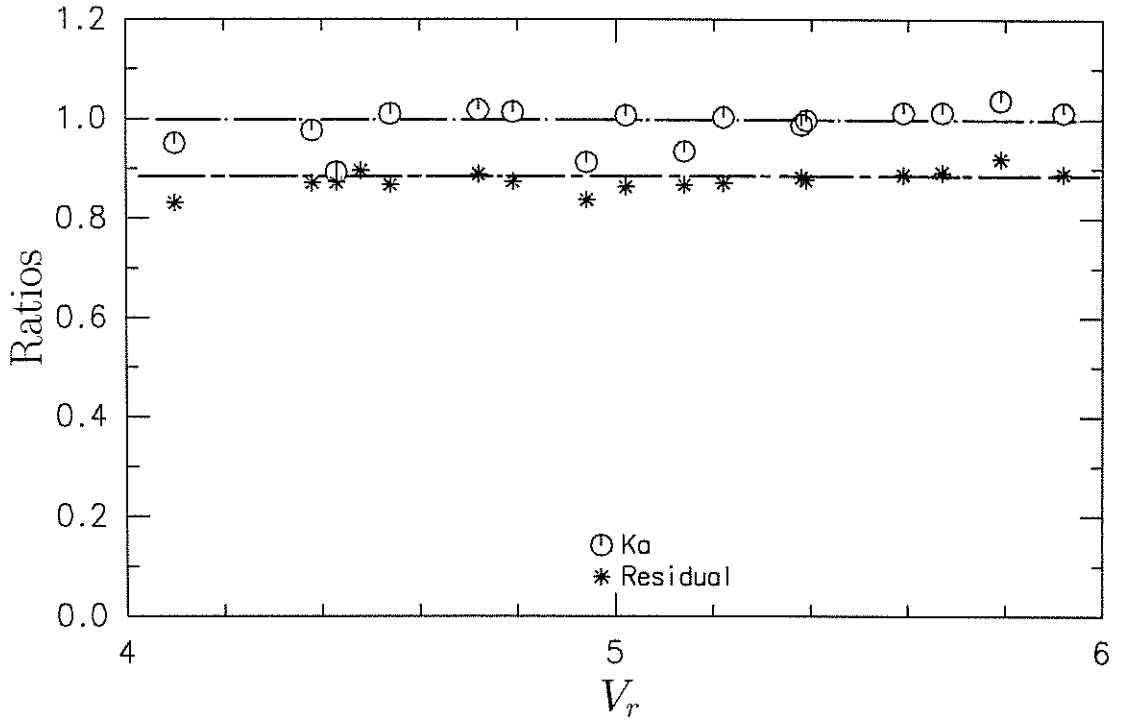

FIGURE 6.46: Comparison of ratio of value of K_a obtained from the average of the timeseries of forces acting on all six transducers to the average value obtained from the six individual measurements with a similar ratio for the residual timeseries which were uncorrelated with motion. $\alpha_{\text{nom}} = 3\%$.

sumed (based on flow-visualization, amongst other things) that motion-correlated forces are well-correlated along the span. The present measurements provide an opportunity to test this assumption. Motion-correlated force coefficients varied from one transducer to the next, and (in the smooth subcritical flows at least) systematically along the span, with magnitudes dropping towards the end of the cylinder (see figs. 6.18, 6.19, 6.20).

It was possible to obtain average values of the coefficients of motion-correlated forces in two ways, and comparison of the results provided information concerning the spanwise correlation of those forces. In the first method, the values of total lift forces obtained at each timestep were averaged over the six transducers to produce a single timeseries of average lift force, from which motion-correlated forces were then prepared. The alternative was to average the values of the motion-correlated forces obtained at each transducer. If the motion-correlated forces were well-correlated along the span at each instant, then the ratios of the coefficients obtained by the two methods should be near unity. These ratios may be compared with the ratios of uncorrelated lift obtained by the two methods; as shown in § 6.4, the residual, uncorrelated forces were imperfectly correlated along the span, in a similar fashion to forces measured on the fixed cylinder. Hence the ratios of the uncorrelated portion of the average forces to the average of the uncorrelated forces at each transducer should be less than unity. Both these expectations are confirmed by the results in figure 6.46. This result, in conjunction with those presented in § 6.4.3, indicates that the observed increase in spanwise correlation lengths on oscillating cylinders can be accounted for by the contribution of motion-correlated forces, as proposed by Vickery (1978).

Finally, the repeatability of the measured coefficients was fair. A measure of this can be gauged from the fact that the results in figures 6.18, 6.19, 6.20 were compiled from experiments conducted on four separate days over the period of a week.

Turbulent flows and supercritical smooth flow

The magnitude of the motion-correlated forces in the remainder of the results was much smaller than was generally the case in smooth subcritical flow; values of C_a rarely exceeded three, while values of K_a rarely exceeded unity.

Low Reynolds numbers The low Reynolds number turbulent flow results (figs. 6.21–6.32) will be discussed first. It is apparent from the results that the motion-correlated force coefficients obtained from the two end-most transducers (nos. 1 & 6) followed a different trend with reduced velocity to the four more central transducers. At lower turbulence intensities (configs. 1 & 2), the general trend for the end transducers was for the value of C_a to increase with reduced velocity, with the value of K_a remaining slightly negative over the range, tending to positive values for the highest reduced velocities. The overall trend for the other transducers was for the values of C_a to remain nearly constant, with a slight fall in magnitude produced by increasing V_r, coupled with small positive values of K_a which, as was the case for the end transducers, showed a tendency to increase with V_r. This lack of uniformity of behaviour along the span is thought to be connected with the lack of spanwise uniformity of the fixed-cylinder results, discussed in chapter 5. As was pointed out there, the results for the two end-most transducers differed from those nearer the centre of the cylinder, a tendency that was more pronounced in turbulence configurations 1 and 2.

Increasing the turbulence intensity (configs. 3 & 4) in general brought about a reduction in the magnitudes of the coefficients C_a and K_a and there was less evidence of a trend in the values with V_r than for configurations 1 & 2. Over the four central transducers, average values of C_a were around unity, while for K_a, average values were slightly positive, near 0.1.

High Reynolds numbers The results for the high end of the Reynolds number range were presented in figures 6.33–6.42. The relative Reynolds-number independence of the fixed-cylinder results for the two highest turbulence intensities (configs. 3 & 4) suggests that the values of motion-correlated force coefficients in these cases should be similar for the two Reynolds numbers used. In general, this was the case, but it is evident that there was more scatter in the values of C_a and K_a than for the low Reynolds number results. In addition, the values of C_a for transducer 6 seem to be consistently in error, in that they were often much larger than for transducer 1. For smooth flow and turbulence configurations 1 and 2, the results for transducer 5 were also incorrect. Taken as a whole, these characteristics suggest that the high Reynolds number results were less reliable than those for low Reynolds numbers, probably due to inaccuracies in the cancellation of inertial force signal. Although, as discussed in § 6.5.1, the errors in cancellation should theoretically have been lower in the high Re flows, it seems that the much higher mechanical stresses in the equipment at the higher Reynolds numbers

produced inconsistencies in the results. These higher stresses would have been brought about by higher dynamic pressures and higher oscillation frequencies, both of which would have produced mechanical stresses which increased roughly as the square of the Reynolds number.

On the basis of the Reynolds number independence of the characteristics of lift on the stationary cylinder in the two highest turbulence intensity cases and on a comparison of the results at the two ends of the Reynolds number range, it may be assumed that the low Reynolds number values of C_a and K_a provide a reasonable guide to what occurred at the high Reynolds number. At the higher turbulence intensities, the value of C_a was near unity, with slight evidence for a drop in value with increased V_r. Overall, K_a took small positive values, near 0.1, although there would be little error in assuming a zero value for K_a.

Comment There are no comparable published measurements of C_a and K_a for these flow regimes. Vickery (1978) produced a prediction of the behaviour of K_a in turbulent flows based on the variation of K_a with V_r observed in smooth flow and using quasi-steady theory (see ch. 1, fig. 1.67). That model predicts that peak values of K_a reduce as turbulence intensity increases, which does not seem to be supported by these results (for example, compare figs. 6.29 & 6.32).

Vickery and Basu (1984, their figure 1) gave a value of $K_a \simeq 0.18$ for transcritical turbulent flows with smooth cylinders; this value apparently derived from a combination of measurements obtained in smooth transcritical flows (Jones, Cincotta & Walker 1969) and Vickery's quasi-steady model for interaction of turbulence with motion-correlated forces (see Vickery and Basu 1983 a). This value of $K_a \simeq 0.18$ is in reasonable agreement with the value of 0.1 obtained in the present experiments. The quasi-steady assumption of Vickery's model is not reasonable for the present experiments though, since the turbulence LSR was approximately 0.5 and the interaction of turbulence with the basic vortex shedding process itself could not be assumed quasi-steady; indeed, as discussed in chapter 5, there was no organized vortex shedding in the smooth and lower-turbulence flows at the higher Reynolds numbers. Since it would seem likely that one of the basic properties of vortex shedding which allows interaction with cylinder motion is the very well-defined frequency, it is not surprising that in the highly turbulent flows the motion-correlated forces were comparatively small, because the vortex shedding was very broad-band.

In addition, the results of Jones, Cincotta & Walker (1969) suggest that in transcritical flows the form of the variations of C_a and K_a with V_r are similar to those found in smooth subcritical flows. The quasi-steady model predicts similar variations C_a and K_a with V_r in turbulent and smooth flows, although the variations with V_r would be "smeared out" in turbulent flow, by convolution with the PDF of the reduced velocity fluctuations in the oncoming flow. The form of variations of C_a and K_a observed in here in turbulent flow were dissimilar to those for smooth subcritical flow, which again suggests that the quasi-steady assumption was not valid in this case.

To properly test Vickery's model for the interaction of large-scale turbulence and motion-correlated forces would require an experiment in which the Reynolds numbers or section properties and turbulence LSRs were such that the interaction could safely be

assumed quasi-steady. For circular cylinders at least, this would imply the use of either moderate (10^4–10^5) or very high transcritical Reynolds numbers, and LSRs of 10:1 or more. The possibility is still open, however, that in transcritical flows of moderate to high turbulence intensity and large LSR, motion-correlated forces will be influenced by the finer scales of turbulence, perhaps in a similar way to fluctuating lift forces on a stationary cylinder, as suggested by Vickery and Daly (1984, see also § 5.3.3). Experimental investigation of this possibility cannot be carried out at low Reynolds numbers since no model for the interaction has yet been proposed.

Taken overall, it would seem that the measurements of motion-correlated forces obtained here in the turbulent flows are not directly applicable to the prediction of full scale structural response to vortex shedding in transcritical flows of similar turbulence intensity. The underlying reason is the mis-match of turbulence LSRs between model and full scale, as was the case for the fixed cylinder results.

6.6 Detailed Examination of Subcritical Flow

6.6.1 Motivation

This section describes a detailed investigation of lift forces which acted on the cylinder in smooth subcritical flow, which is the focus of attention since the size of the motion-correlated forces were greatest in this regime, and showed the greatest influence of reduced velocity of any of the regimes used. An important consideration is that smooth subcritical flow serves as a model for behaviour at transcritical Reynolds numbers in smooth flows, and turbulent flows with large LSRs. Examination of two sets of results obtained with forced cylinder oscillations in smooth transcritical flows (Jones, Cincotta & Walker 1969, smooth cylinder; Szechenyi & Loiseau 1975, roughened cylinder), shows that motion-correlated forces exist in these flows, with characteristics similar to those for subcritical flows; it is presumed that they also exist in turbulent flows with large LSRs.

The examination concentrates on the largest oscillation amplitudes used (3% D), since the results of the previous section indicate that the characteristics of motion-correlated forces were similar over the range of amplitudes used, but that the magnitudes were greatest at the largest amplitude.

Lock-in, as defined by frequency capture of vortex shedding by cylinder oscillation, is examined in § 6.6.2. The phase characteristics of long-time-average motion-correlated forces with respect to cylinder motion are studied in § 6.6.3, while short-time-average phase characteristics are the focus in § 6.6.4.

The work in § 6.6.4 was carried out in a effort to define a conditioning scheme which could discriminate between the two most obvious models for motion-correlated forces at small oscillation amplitudes. These are:

1. Motion-correlated forces exist during each cycle of cylinder motion, with magnitudes and phase angles which are functions of cylinder oscillation amplitude and reduced velocity. The motion-correlated forces magnitudes are determined on the

basis of long time averages, but are presumed to act in each cycle of oscillation, as suggested by figure 6.1 (b).

2. Vortex shedding is influenced by cylinder motion, but the amplitude of the cylinder oscillation is not large enough to maintain control. Vortex shedding drifts in and out of phase maintenance with respect to cylinder motion.

The method employed was to examine the short-time-average properties of the forces which acted on the whole cylinder (obtained by averaging forces along the span at each time-step). While the method was able to provide some additional information about the characteristics of vortex-induced forces on oscillating cylinders, it was unable to provide a basis for discriminating between the two possibilities mentioned above.

Recently it has become possible to obtain computer-graphic visualizations of three-dimensional representations of lift force timeseries, and some work in this direction has been commenced in § 6.6.5. Due to a lack of time, only preliminary investigations have been carried out; while the results indicate that there is additional information to be obtained about the character of vortices shed from oscillating cylinders by consideration of the three-dimensional nature of the vortex-induced forces, comparisons with the short-time average results in § 6.6.4 did not produce any conclusive evidence with regard to the two possibilities listed above.

6.6.2 Frequency Capture

A point of interest was to examine if lock-in, as defined by capture of vortex shedding frequency, occurred at any of the reduced velocities near the coincidence of vortex shedding and cylinder oscillation frequencies. Previous observations, for instance by Stansby (1974) and Koopman (1967), have shown that the range of reduced velocity over which lock-in is observed reduces with amplitude (see ch. 1, figs. 18 & 21). Koopman's results suggested that a critical amplitude of oscillation must be exceeded for lock-in to occur; in his case $\alpha > 10\%$ at Reynolds numbers 100–300. In Stansby's experiments, amplitudes greater than 3% of diameter were needed to achieve lock-in at $Re = 9200$, while at $Re = 3600$ lock-in occurred at $\alpha = 1\%$.

Results presented in the previous parts of this chapter suggest that lock-in was a possibility in the $\alpha_{\text{nom}} = 3\%$ cases near the critical reduced velocity. Indication of this is given by the apparent plateau in figure 6.4, which shows the magnitude of motion-correlated lift as functions of V_r and α. The plateau ($\sigma_{C_{l\text{correlated}}} \simeq 0.6$) occurred for $\alpha_{\text{nom}} = 3\%$ only, over the range of V_r from 4.79 to 5.14. At lower amplitudes of motion, the values of $\sigma_{C_{l\text{correlated}}}$ tended towards a peak of 0.6 at the critical reduced velocity. It was decided to investigate the spectra of (total) lift forces over a range of reduced velocities which spanned the plateau. The results are presented in figure 6.47.

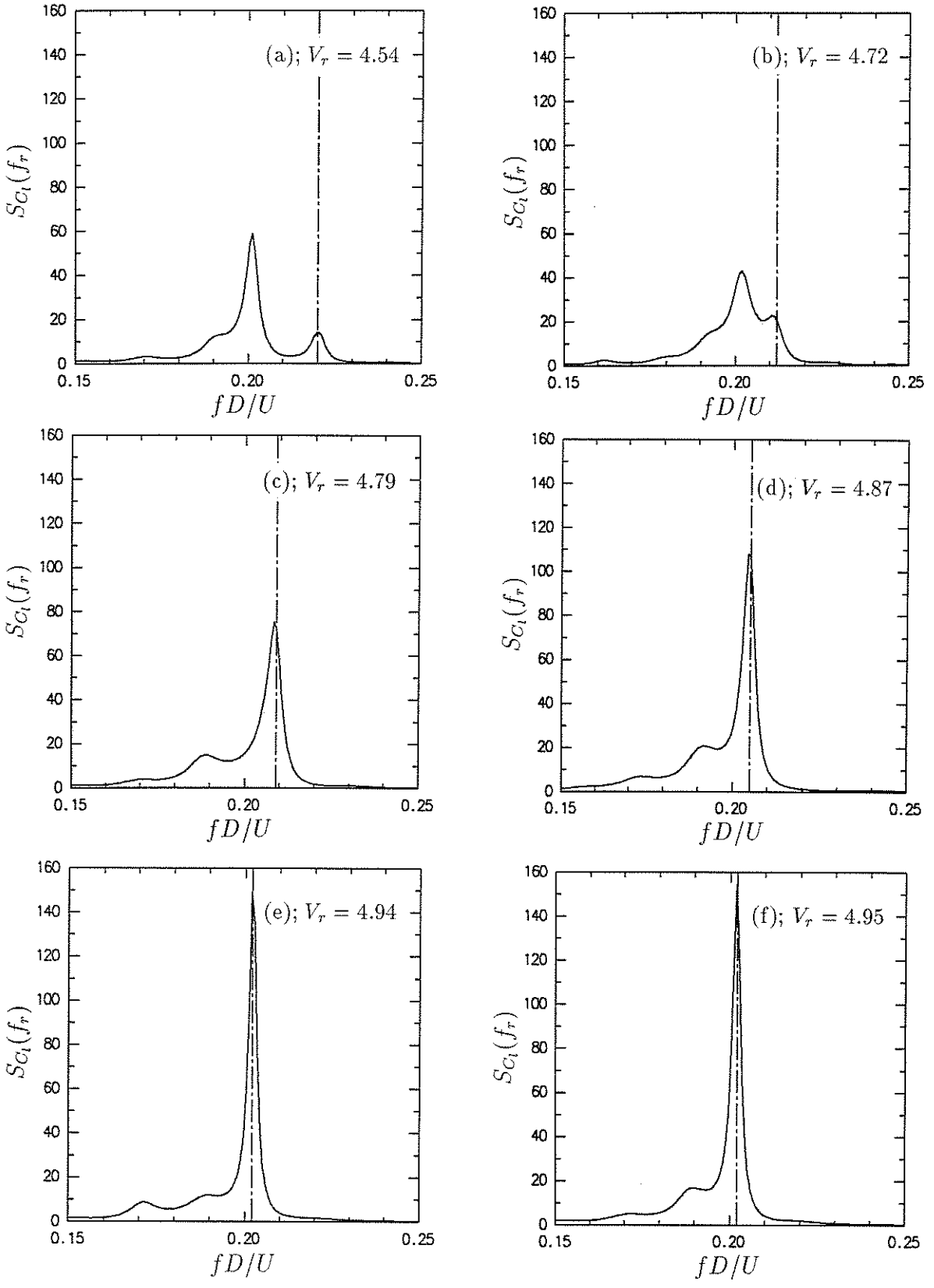
(a); $V_r = 4.54$
(b); $V_r = 4.72$
(c); $V_r = 4.79$
(d); $V_r = 4.87$
(e); $V_r = 4.94$
(f); $V_r = 4.95$
$S_{C_l}(f_r)$
fD/U
0
20
40
60
80
100
120
140
160
0.15
0.20
0.25

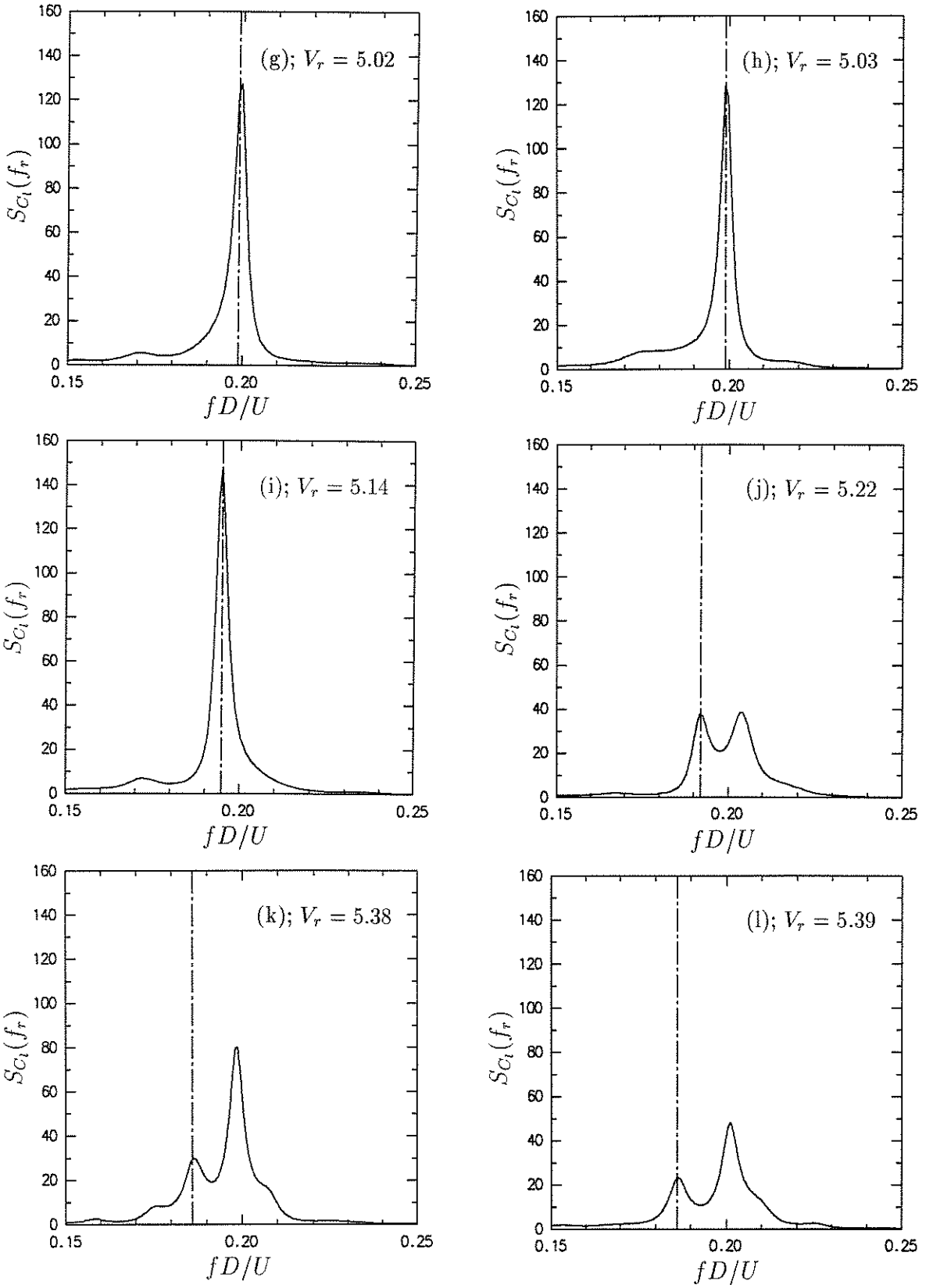

FIGURE 6.47: Spectra showing lock-in in smooth subcritical flow ($Re \simeq 1.6 \times 10^5$, $\alpha_{\text{nom}} = 3\%$). Reduced velocity increased from one plot to the next, corresponding to a decrease in cylinder oscillation frequency, indicated by a dashed vertical line in each plot. (a) & (b); V_r below the plateau in fig. 6.4. (c)–(i); Traversing the plateau. (k)–(l); V_r above the plateau. Maximum Entropy Method spectra obtained with 200 poles.

It was felt that the FFT-based spectral analysis used in the preliminary investigations of lift forces did not provide sufficient frequency resolution for such an investigation; the analysis bandwidth for the spectra previously presented corresponded to about 3% of the Strouhal frequency. Obviously the bandwidth could be reduced, but at the expense of reliability of spectral estimates. In view of this, Maximum Entropy Spectral analysis was used for the more detailed investigations to be described here. This method is better able to fit sharp spectral features in limited runs of data, and has greater ability to resolve closely-spaced spectral peaks than FFT-based methods (see Press et al. 1986, § 12.8, Childers 1978).

Figure 6.47 shows the progression of spectra of total lift force at transducer 3 as reduced velocity increased from 4.54 to 5.39 (produced by reducing the oscillation frequency). Dashed vertical lines in the figure represent the frequency of cylinder oscillation. This range covers the plateau in figure 6.4; figures 6.47 (a) and (b) are for the two reduced velocities below the plateau (4.54 & 4.72), figures 6.47 (c)–(i) traverse the plateau (V_r = 4.79 to 5.14), while figures 6.47 (k), (l) and (m) are for the first three reduced velocities above the plateau (5.22, 5.38 & 5.39). It can be seen that there were two spectral peaks for the cases which lay on either side of the plateau, one peak at the cylinder oscillation frequency, and the other near the Strouhal number for the fixed cylinder ($St \simeq 0.202$). In contrast, for each of the plots which correspond to the plateau of values in figure 6.4 there was only one spectral peak, at the frequency of cylinder oscillation. This indicates that the plateau of lift forces over the range of reduced velocities 4.79 to 5.14 in figure 6.4 corresponded to lock-in (but see the qualification in § 6.6.4 below).

6.6.3 Phase of Motion-Correlated Forces near Lock-In

The evidence presented in figures 6.4, 6.47 and 6.43 suggests that during lock-in, the magnitude of motion-correlated lift remained nearly constant but the phase with respect to cylinder motion varied. This hypothesis is supported by figure 6.48, where the acceleration- and velocity-correlated components of lift (C_{la} & C_{lv}) are plotted against one another with reduced velocity as a parameter. Values are the averages obtained over the four central transducers for $\alpha_{\text{nom}} = 3\%$. The asymptotic values ($C_{la} \to -\infty$, $C_{lv} \to -\infty$ as $V_r \to 0$, and $C_{la} \to 0^+$, $C_{lv} \to 0^-$ as $V_r \to \infty$) were worked out using the asymptotic values for C_a and K_a from chapter 1, § 1.6.6 (and l'Hopital's rule when needed). It can be seen that over the range of V_r which corresponded to lock-in, the values of C_{la} and C_{lv} fitted a circular arc reasonably well.

The change of phase of motion-correlated forces is in agreement with previous flow visualization results, for example those of Ongoren and Rockwell (1988, see fig. 1.27), which show a rapid change of phase of vortex shedding as reduced velocity is changed near the critical value of 5.

Effectively the same data (values of C_a and K_a from fig. 6.43) are replotted in a similar format in figure 6.49. Again, the asymptotic values from § 1.6.6 were used.

Consideration of figure 6.49 lead to the following speculation about the nature of structural vibrations of flexibly-mounted circular cylinders at and near lock-in. Instability, corresponding to positive values of K_a, would be promoted near $V_r = 5$ by

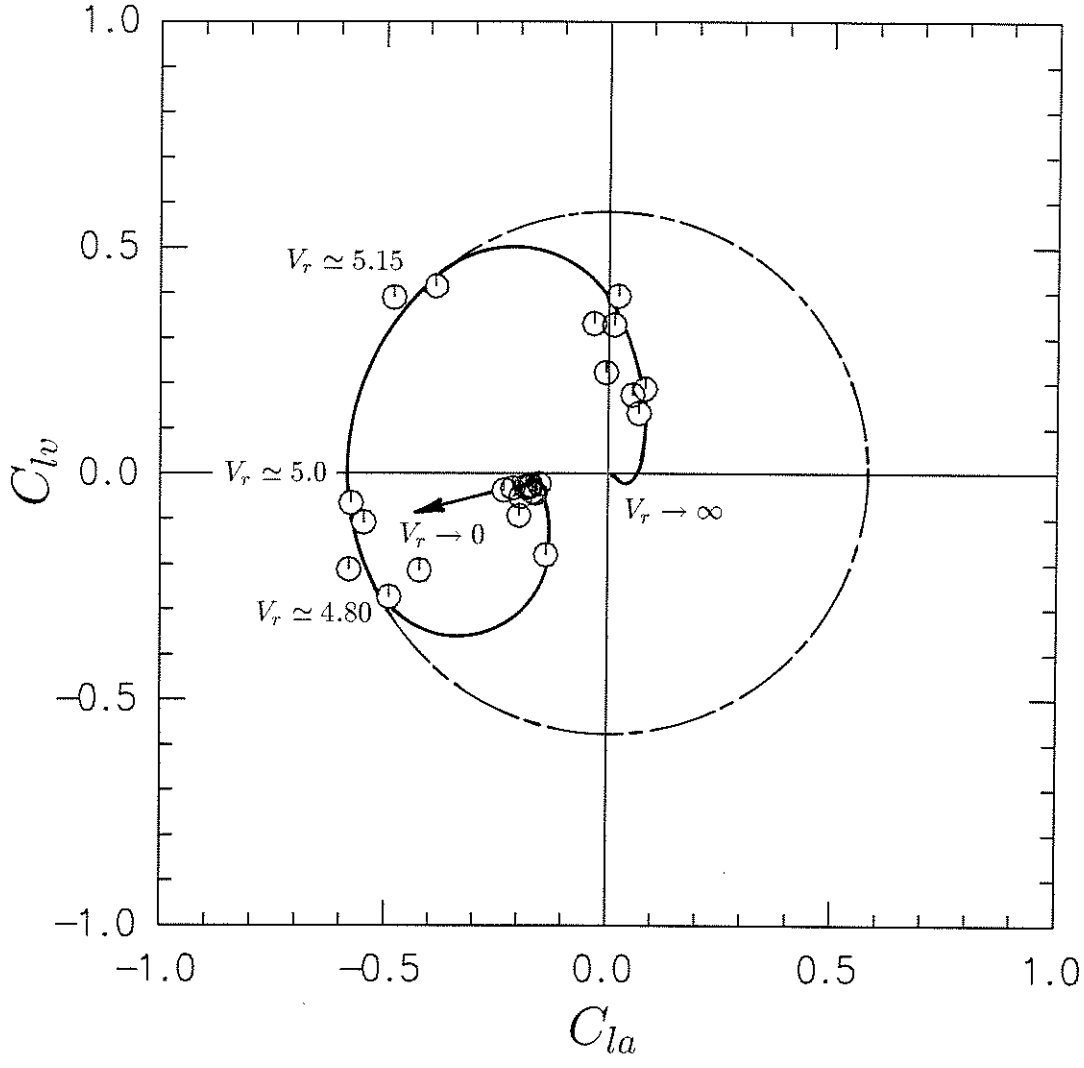

FIGURE 6.48: Coefficients of acceleration- and velocity-correlated lift (C_{la} & C_{lv}) for smooth subcritical flow plotted against one another with V_r as a parameter.

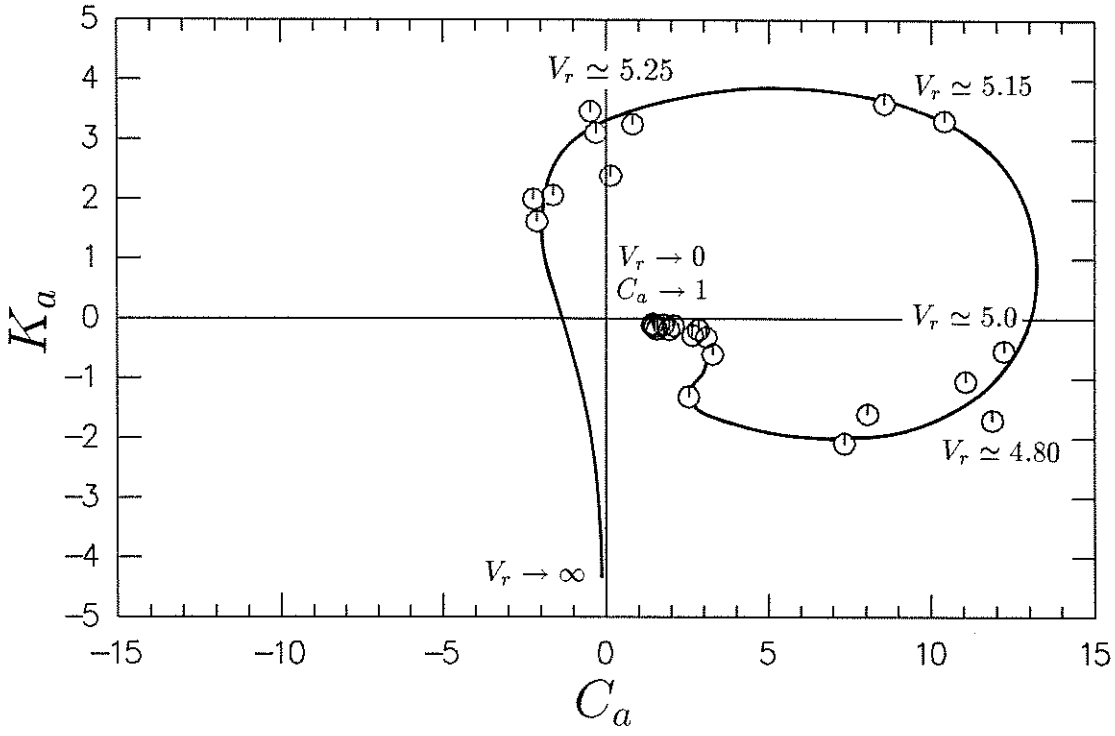

FIGURE 6.49: Values of coefficient of added mass (C_a) and aerodynamic damping parameter (K_a) in smooth subcritical flow, presented in polar form with V_r as a parameter.

variation in the coefficient of added mass. At $V_r > 5.25$, C_a would be negative, tending to increase the frequency of structural oscillation, thus decreasing the reduced velocity. Conversely, at $V_r < 5.25$, C_a would be positive, tending to reduce the frequency of structural oscillation, increasing V_r towards the zone of highest K_a.

Motion-correlated forces would thus tend to maintain instability by frequency regulation of the oscillating structure. As flow velocity is increased past the onset of lock-in, the coefficient of added mass would become negative, tending to increase the frequency of oscillation, "attracting" the structural frequency towards the frequency at which the wake would oscillate if the cylinder were fixed. The importance of this effect would depend on the density ratio $m/\rho D^2$. For most elastic structures in air, the ratio is large (a representative minimum for a lightly-constructed steel stack might be 40:1). The ability of the effect to influence the frequency of structural oscillation would be correspondingly small, and in experiments conducted in flows of air (see e.g. the results of Feng 1968, shown in ch. 1 as fig. 1.16) the frequency of cylinder oscillation remains sensibly constant during lock-in. For flows of water past thin-walled steel tubes, the ratio of $m/\rho D^2$ is typically closer to unity, or less. Results from an experiment conducted in water (Angrilli, Di Silvio & Zanardo 1974, ch. 1, fig. 1.17) show that the frequency of structural oscillation was indeed attracted to the fixed-cylinder Strouhal frequency as V_r was increased past the onset of lock-in.

6.6.4 Power Transfer and Phase Maintenance

The work to be described in this section was conceived in an attempt to better understand the behaviour of vortex shedding during and near lock-in. The first aspect was the computation of signals proportional to the instantaneous power transfer between the fluid and the cylinder, obtained by multiplying timeseries of coefficient of lift by those of cylinder cross flow velocity. The products can also be interpreted as timeseries of instantaneous correlation between lift force and cylinder velocity; C_{lv} is proportional to the sum of such a timeseries. For convenience of discussion, these timeseries will be referred to as timeseries of power transfer in the following, with the understanding that a constant of proportionality has been omitted. Timeseries of the average lift forces and velocities across all the transducers were used in the computation, rather than timeseries from a single transducer, which had the effect of magnifying the motion-correlated forces with respect to the uncorrelated forces (since the motion-correlated forces had better correlation along the span, as shown in § 6.5.4). Since most of the lift, even during lock-in, was uncorrelated with cylinder motion, timeseries of power transfer fluctuated in sign as forces went in and out of phase with cylinder velocity on an almost random basis. The timeseries had positive or negative mean values, according to the sign of C_{lv} (or K_a). Occasionally there were indications of sustained positive or negative power transfer, over periods longer than the timescale for the random fluctuations. These features may all be observed in figure 6.50.

The second aspect of the study involved the fitting of sinusoids of the frequency of cylinder oscillation to the timeseries of average velocities and lift forces. The sinusoids were fitted over times much shorter than the entire data collection time; 60 samples were used, which was typically about four vortex shedding periods. Figure 6.51 gives an example of the results of a least-squares fit to a coefficient of lift timeseries, where in addition to the fitted portion, sixty samples "up and downstream" are shown. The objective was to obtain information about the phase relationship between vortex shedding and cylinder velocity, which could be found by computing the phase difference between the sinusoids fitted to cylinder velocity and lift respectively. The fitting process was passed through the timeseries of velocity and lift, acting as a moving average filter which produced as output timeseries of phase difference and magnitude of the sinusoid fitted to the lift force.

The power transfer and phase information were complementary; when periods of sustained positive or negative power transfer occurred, vortex shedding tended to become phase-locked to cylinder oscillation. This effect is shown in figures 6.52–6.56, where the data correspond to reduced velocities below lock-in (fig. 6.52, $V_r = 4.72$), at the low, mid, and high reduced velocities through the plateau in figure 6.4 (fig. 6.53, $V_r = 4.79$; fig. 6.54, $V_r = 5.02$; fig. 6.55, $V_r = 5.14$), and above lock-in (fig. 6.56, $V_r = 5.22$). Phase information is presented as multiples of π; dotted horizontal lines correspond to multiples of 2π. Also shown in the figures are lines which show the rate at which the phase of vortex shedding would have diverged from that of cylinder oscillation had all the vortex shedding occurred at the Strouhal frequency ($St = 0.202$, on the basis of figure 6.47). It can be seen that the phase-locking which occurred was not complete, in that although there are regions in figures 6.52–6.56 in which the line of phase angle is approximately horizontal, the sections are never completely straight.

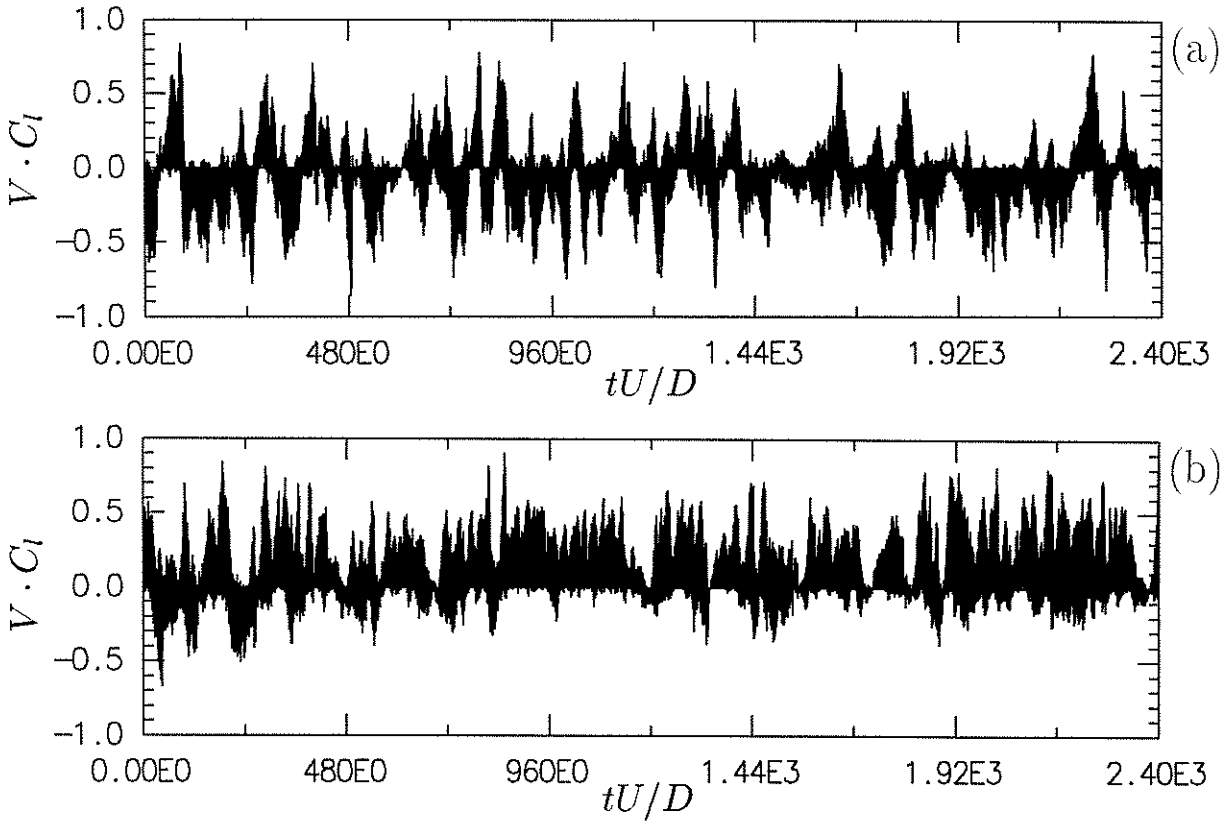

FIGURE 6.50: Timeseries of power transfer from the fluid to the cylinder. In both cases, records for the entire data collections ($\simeq$ 8000 samples) are shown, with a dimensionless timebase tU/D. The cases correspond to the spectra in figure 6.47 (b) and (g). (a) $Vr = 4.72$; below lock-in, K_a negative. (b) $Vr = 5.02$; during lock-in, K_a positive.

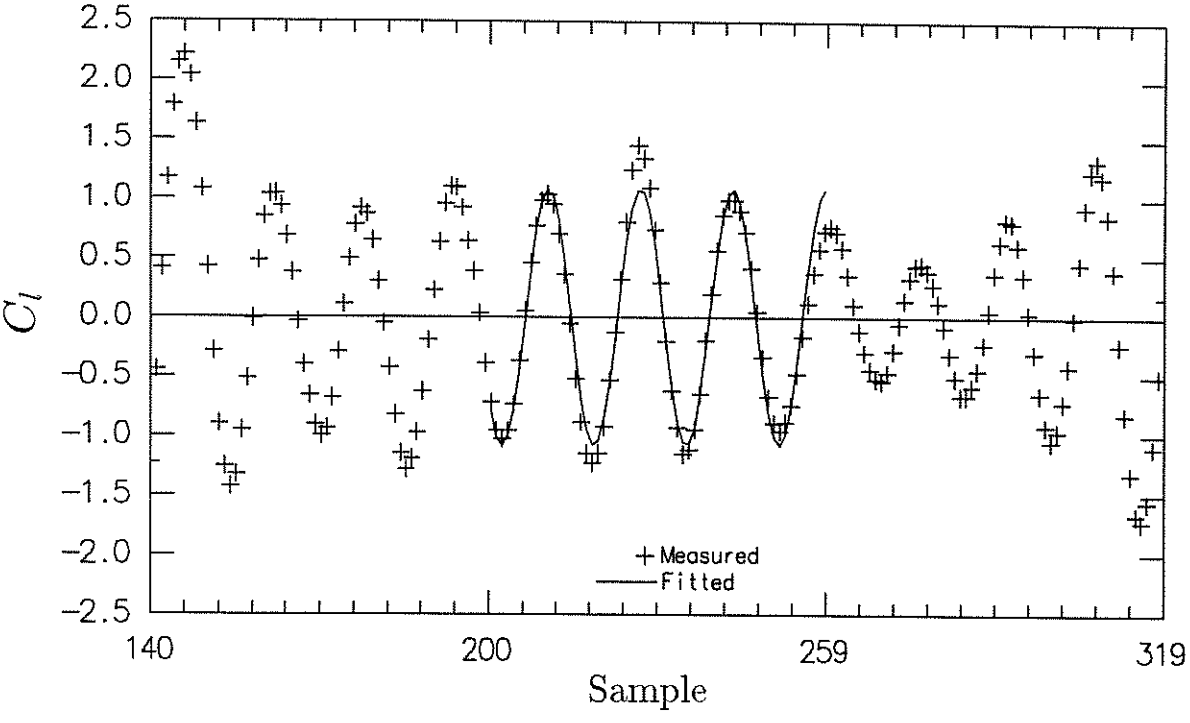

FIGURE 6.51: Average coefficient of lift timeseries and sinusoid fitted over sixty samples.

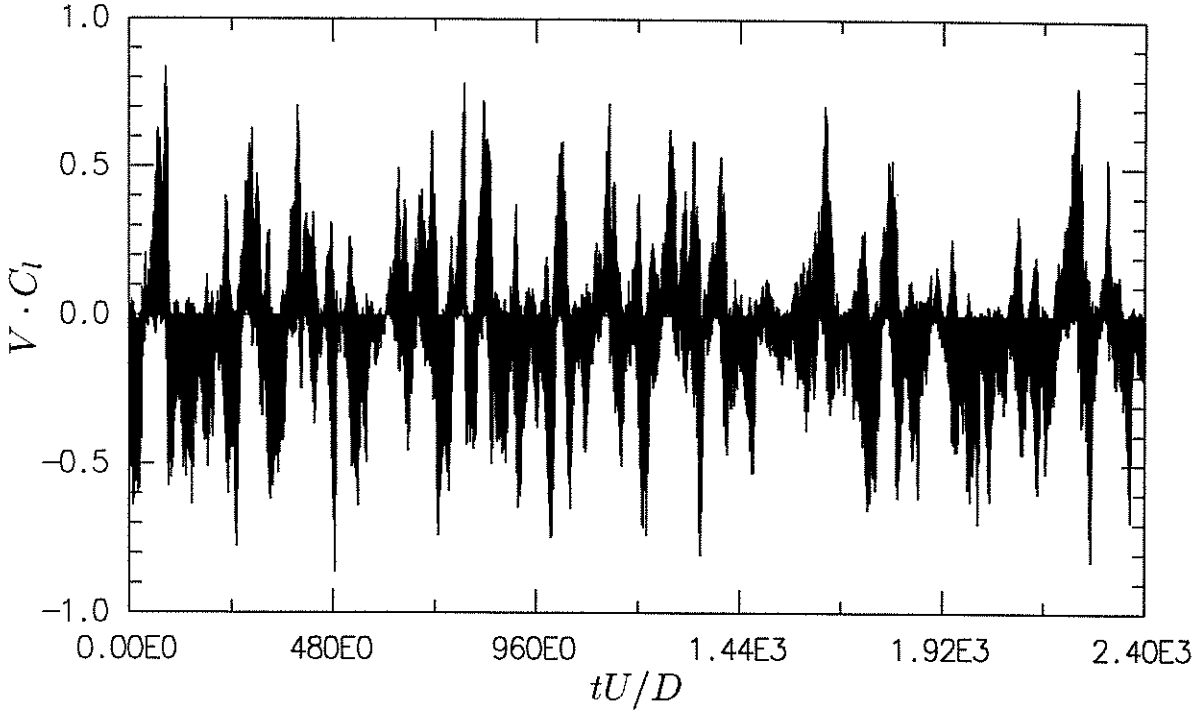

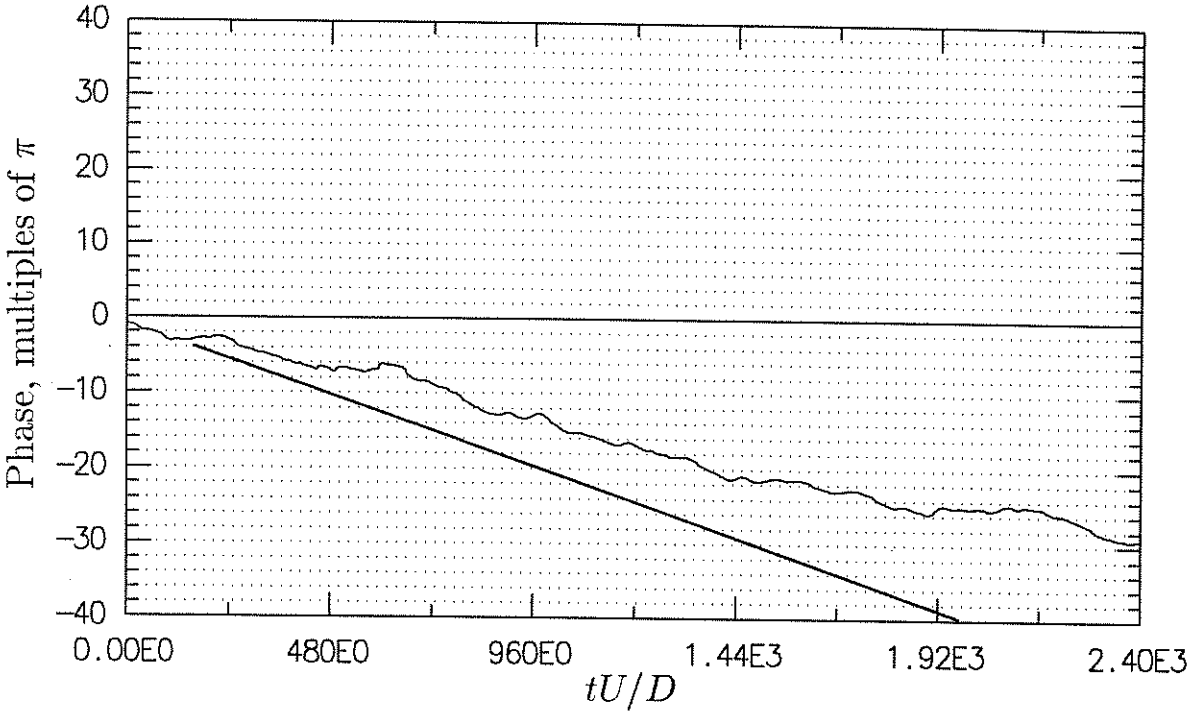

FIGURE 6.52: Power transfer and phase angle timeseries for $V_r = 4.72$, below lock-in. Timebase tU/D is dimensionless. In the presentation of phase angle, dotted horizontal lines correspond to multiples of 2π, while the diagonal solid line shows the rate at which the phase of vortex shedding would have diverged from that of cylinder oscillation if vortex shedding had occurred at $St = 0.202$.

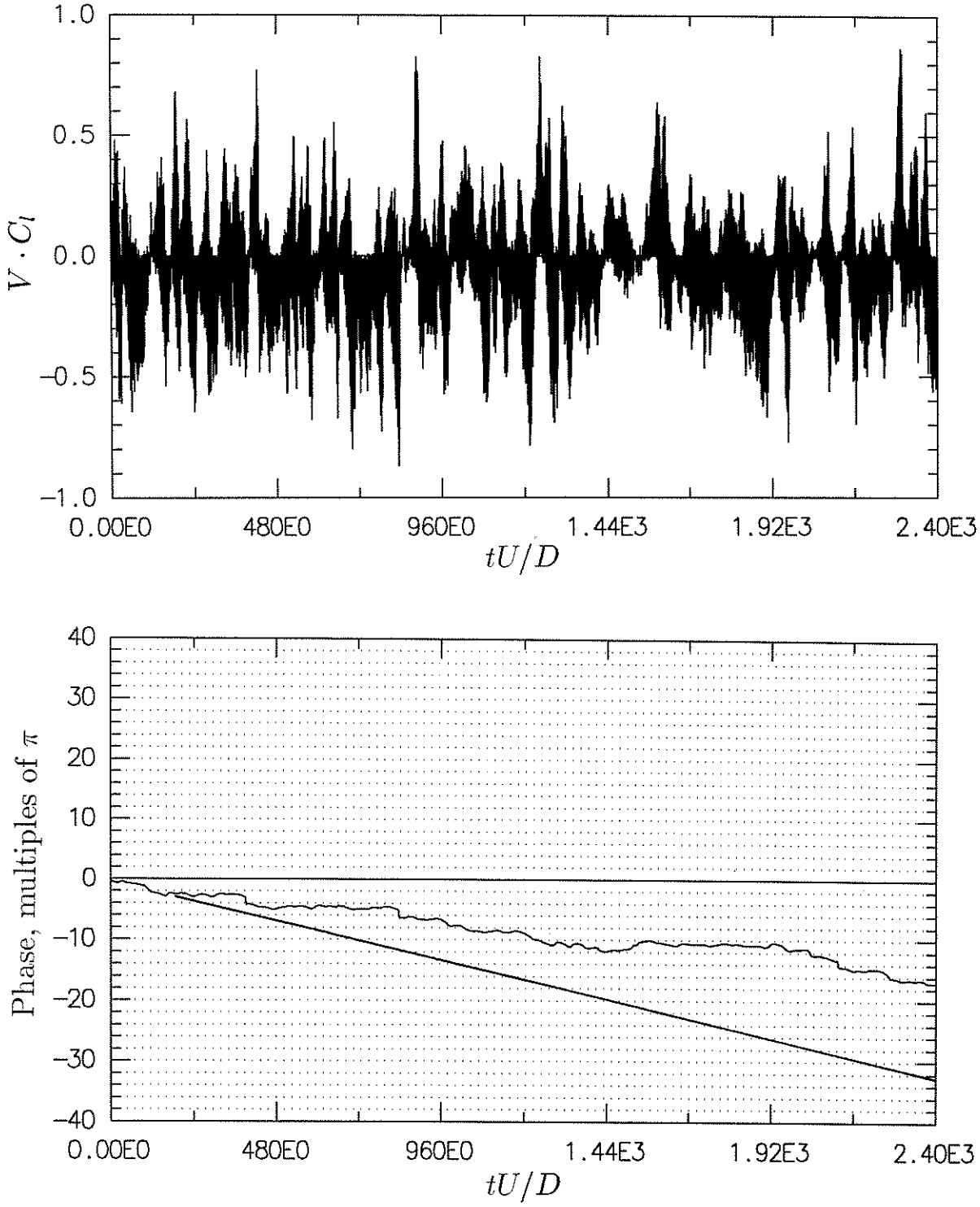

FIGURE 6.53: Power transfer and phase angle timeseries for $V_r = 4.79$, during lock-in. Other information as for fig. 6.52.

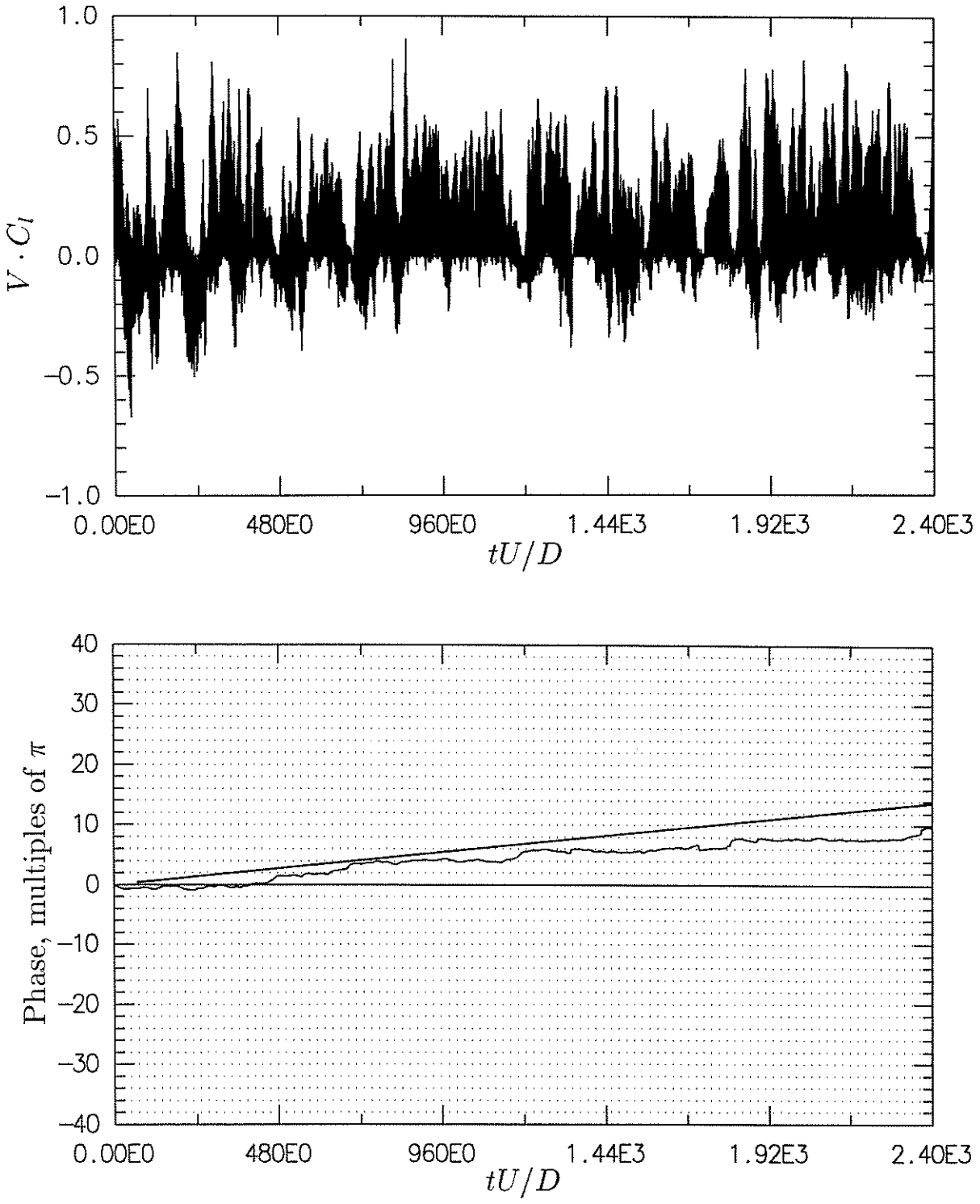

FIGURE 6.54: Power transfer and phase angle timeseries for $V_r = 5.02$, during lock-in. Other information as for fig. 6.52.

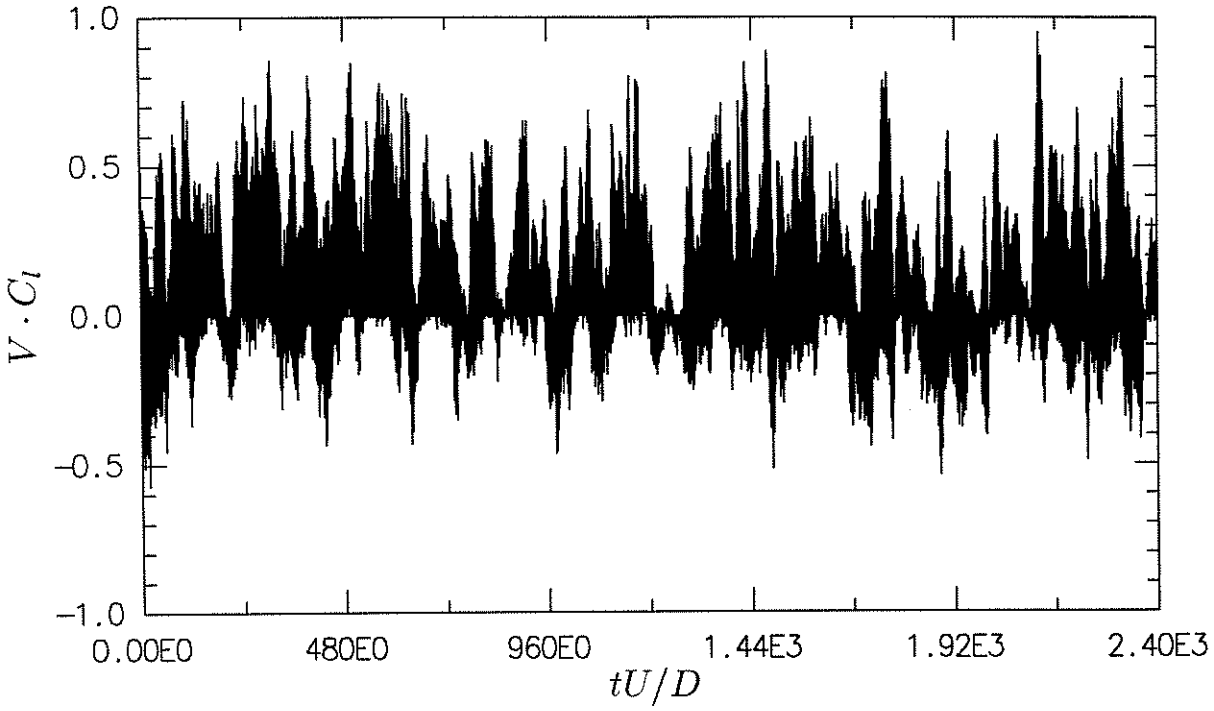

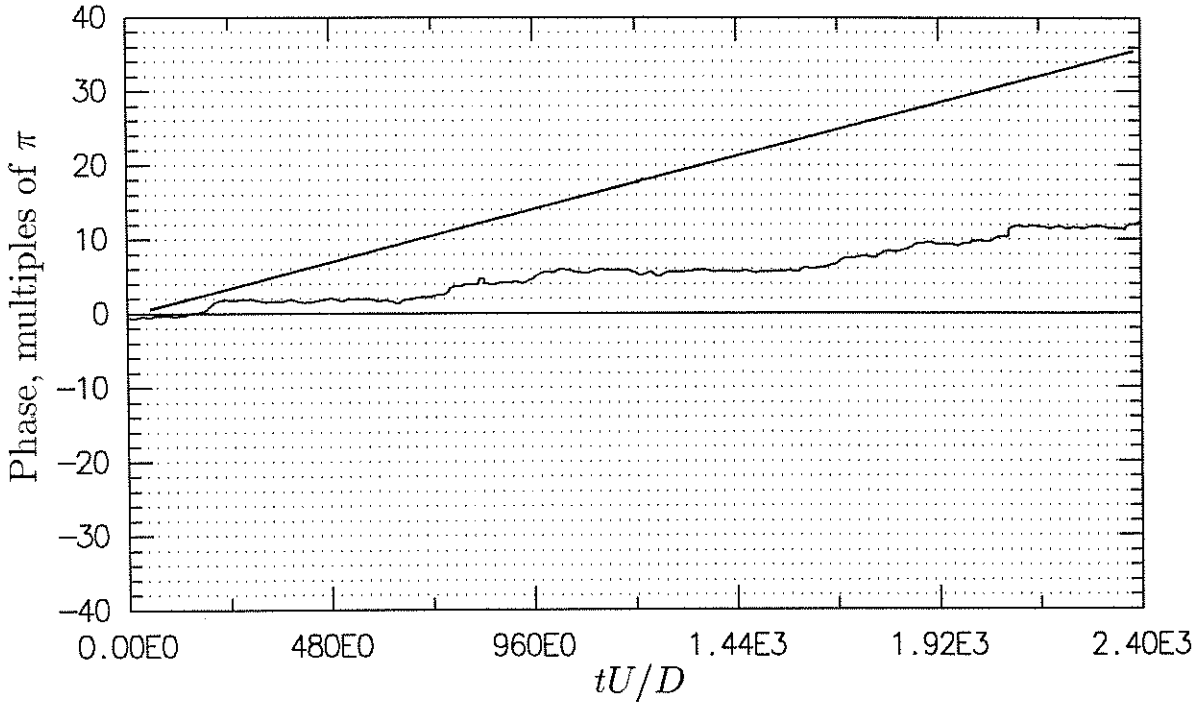

FIGURE 6.55: Power transfer and phase angle timeseries for $V_r = 5.14$, during lock-in. Other information as for fig. 6.52.

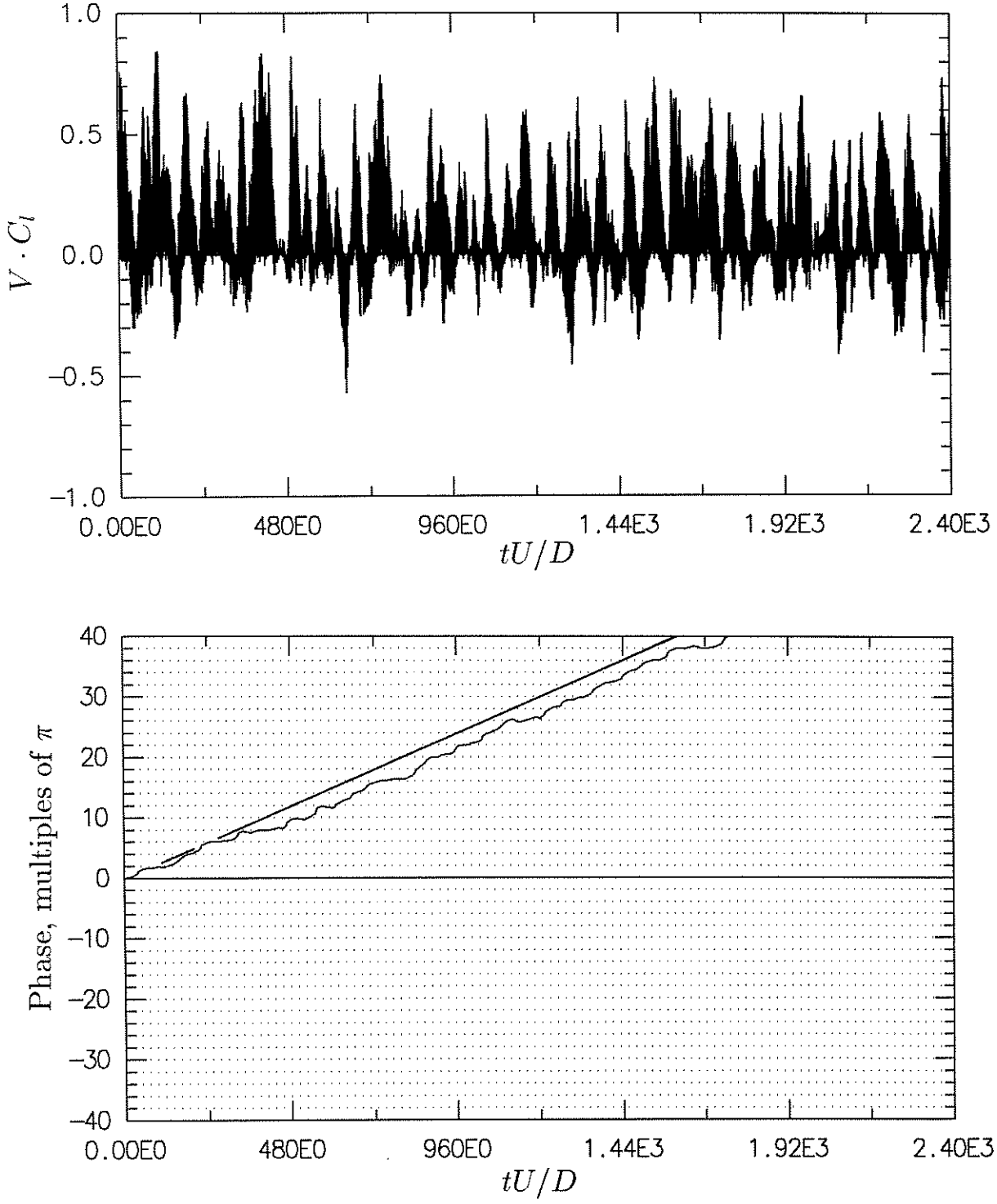

FIGURE 6.56: Power transfer and phase angle timeseries for $V_r = 5.22$, above lock-in. Other information as for fig. 6.52.

When the lines of phase angle were approximately horizontal for many vortex shedding periods (one period corresponds to $tD/U \simeq 5$), the frequency of vortex shedding was the same as the cylinder frequency, while when the lines of phase angle followed parallel to the diagonal lines in the figures, vortex shedding took place at or near the fixed-cylinder Strouhal frequency. An interpretation is that the vortex shedding process was trying to proceed at a different pace to that of the cylinder oscillation, and did so when the mechanism of phase maintenance supplied by cylinder oscillation became ineffective. Thus it can be concluded that *all* the cases examined displayed intermittent lock-in, even the ones in figure 6.47(c)–(i) for which only a single spectral peak could be discerned when the analysis was performed over the whole data record. It seems likely that over extended times, it is the locked-in periods which contribute towards the motion-correlated forces, while the positive and negative contributions to the correlations for the remaining periods tend to cancel one another.

In part, the foregoing investigation was prompted by the following remarks made by Vickery and Basu (1983 a; note that f_o is the frequency of cylinder of oscillation, while f_s is the vortex shedding frequency):

> For values of f_o/f_s differing from unity, two distinct peaks in the spectrum of lift force are apparent; in these regions the assumption that the [vortex shedding and motion-induced] forces are uncorrelated is justified. When $f_o/f_s \simeq 1$, a single peak is visible and it is not possible to distinguish the two forces. In this condition, and when amplitudes are sufficiently large, it has been commonly accepted that a solitary force exists, fluctuating at the frequency of vibration. Nevertheless, the following alternative description does not contradict the observations: two separate fluctuating forces exist at all times, but at large amplitudes the motion-correlated force dominates, and engulfs, the vortex-shedding forces. In the present model both forces are accounted for under all conditions and are assumed to be uncorrelated even for $f_o \simeq f_s$.

It was at first thought that the information of figures 6.52–6.56, particularly that concerning phase-locking, was in conflict with the claim made above, however some further work showed that this is not necessarily the case.

Figure 6.57 shows the results of digital simulation in which a sinusoidal signal was added to Gaussian narrow-band noise with a spectrum of the form given by Vickery and Clark (1972, see ch. 1, eqs. (1.14), (1.15), $B = 0.06$). The total signal was then passed through the same data analysis used to produce figures 6.52–6.56. Frequencies and sampling rates were manipulated to give a format directly comparable to those figures; the sinusoidal frequency was 4.2% lower than the random signal centre-frequency, while the ratio of standard deviation of the sinusoidal signal to the random signal was 1/2, which is comparable with the ratios in figures 6.54 and 6.55. It can be seen that the figure has many characteristics in common with figures 6.52–6.56, including periods of apparent phase-locking and sustained "power transfer".

Changing emphasis slightly, some additional information can be gained by plotting the magnitude of the sinusoids fitted to the coefficient of lift timeseries (as in fig. 6.51) in conjunction with the phase angle. Since the short sections of sinusoids were fitted

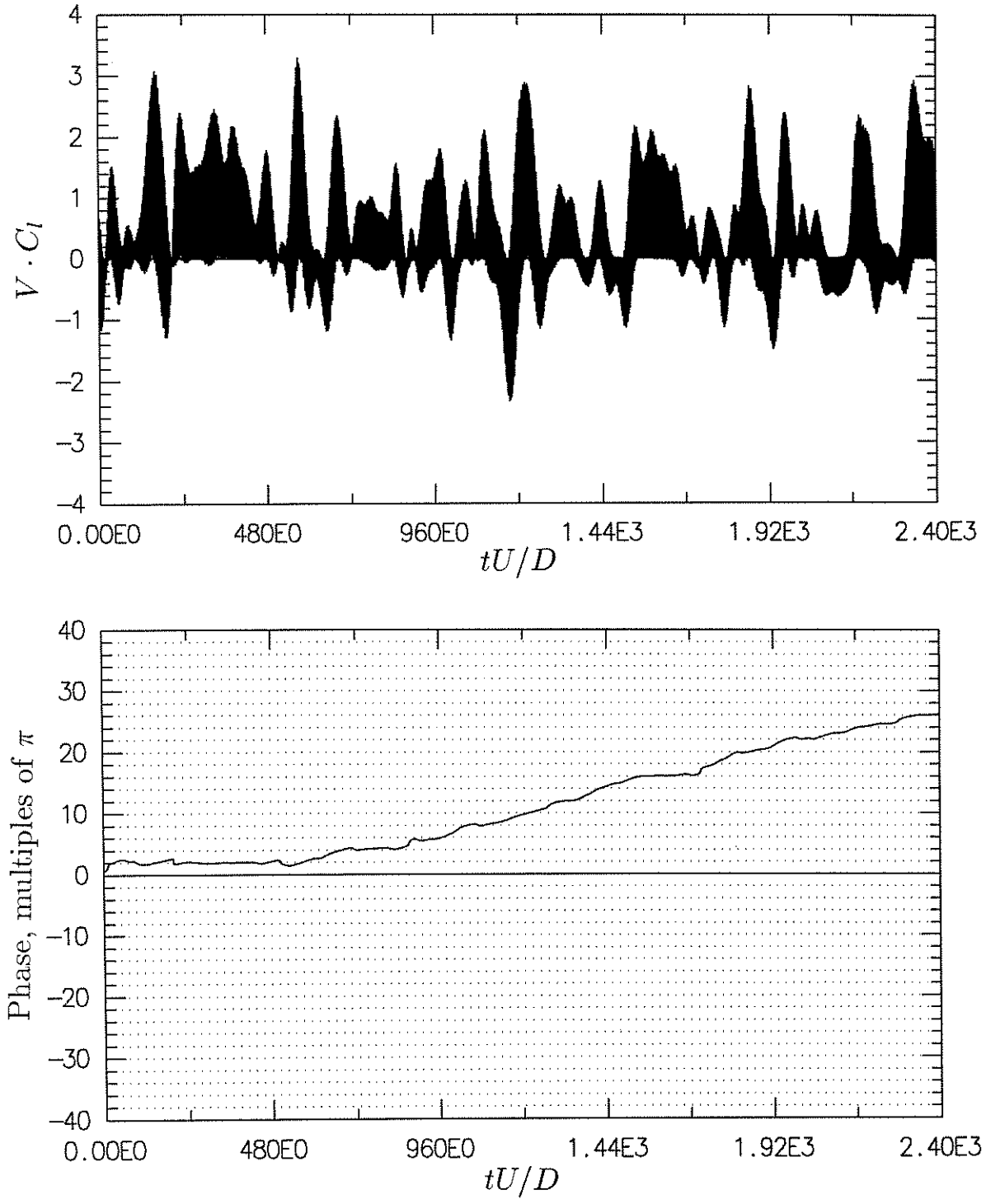

FIGURE 6.57: Timeseries of "power transfer" and phase angle produced by digital simulation. Analysis was the same as applied in figures 6.52–6.56. Input was the sum of a narrow-band random signal and a sinusoid.

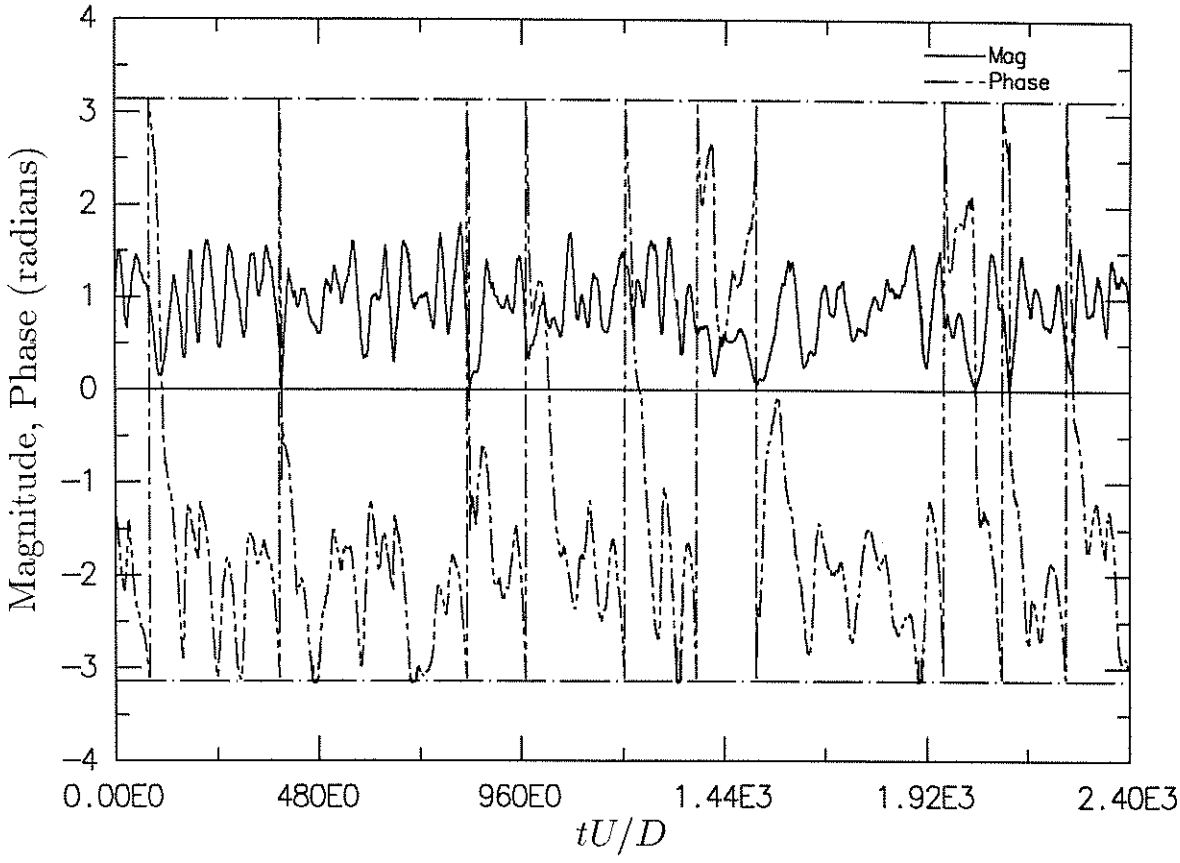

FIGURE 6.58: Timeseries of fitted magnitudes and phases at $V_r = 4.79$.

over about four vortex shedding periods, some smoothing of magnitude (and phase angle) variations must have taken place. Results of this data processing are presented in figures 6.58–6.60, which all come from within the lock-in range suggested by the plateau in figure 6.4. Figure 6.58 is for $V_r = 4.79$, figure 6.59 for $V_r = 5.02$, figure 6.60 for $V_r = 5.14$, which correspond to figures 6.53, 6.54 and 6.55 respectively. In these plots, the phase angle information is presented in a slightly different format to that used in figures 6.52–6.56, since it presented as radians, but not as multiples of π; also the angles have not been "unwrapped", so that they all fall within the range $\pm\pi$, which is indicated by horizontal chained lines.

The first thing to note about the figures is the average phase angles in each case, which were in agreement with the signs of C_{la} and C_{lv} for these sets of data. In figure 6.58, the phase angle lies mostly in the range $-\pi/2$ to $-\pi$, which is correct for negative values of both C_{la} and C_{lv} (C_a positive, K_a negative). In figures 6.59 and 6.60, the average phase angles lay in the range 0 to $-\pi/2$, which corresponds with C_{la} negative and C_{lv} positive (C_a and K_a both positive).

The second point of note is the apparent correlation between changes in phase and changes in magnitude of fitted sinusoids, where retardation in phase angle tended to correlate with decreased magnitudes of lift, while advancement in phase tended to correlate with increased magnitudes.

Third, large and sustained changes in phase angle (typically associated with transi-

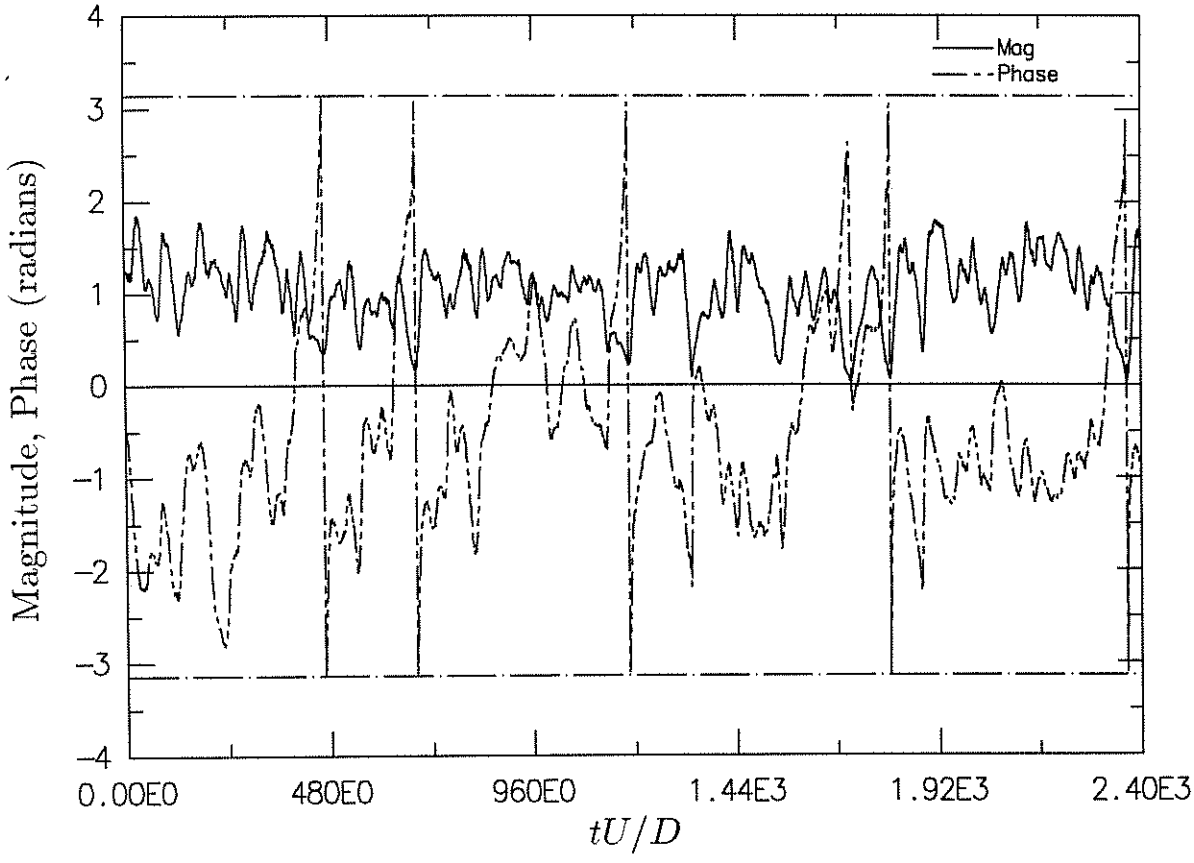

FIGURE 6.59: Timeseries of fitted magnitudes and phases at $V_r = 5.02$.

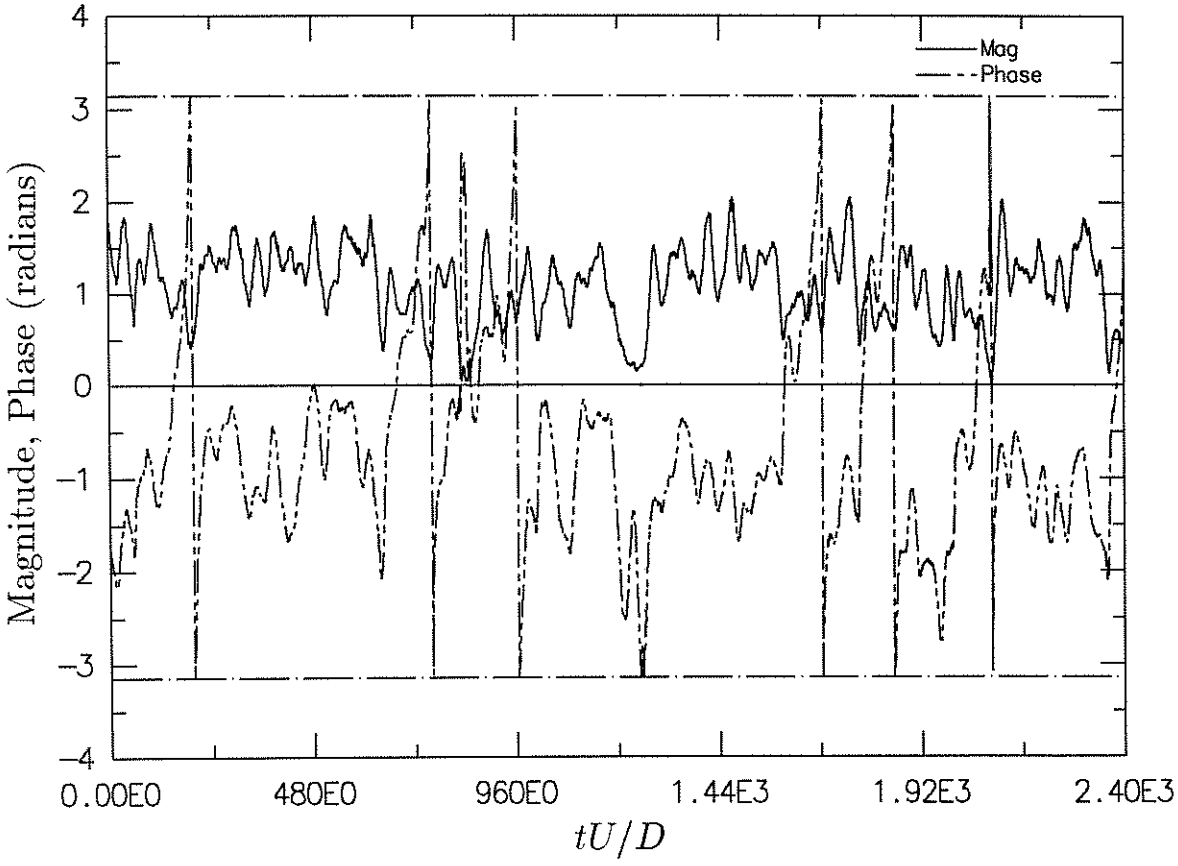

FIGURE 6.60: Timeseries of fitted magnitudes and phases at $V_r = 5.14$.

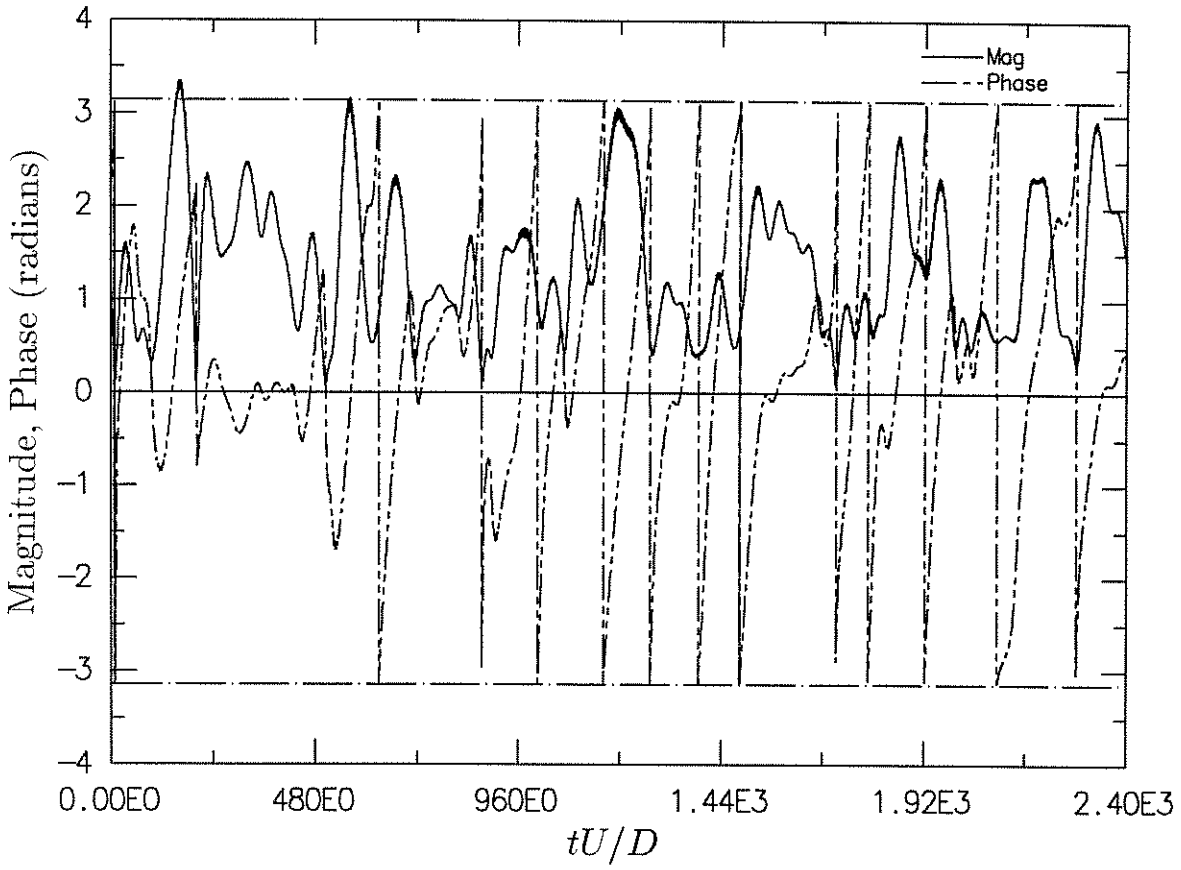

FIGURE 6.61: Timeseries of fitted phases and magnitudes produced by digital simulation.

tions between $+\pi$ and $-\pi$) tended to be accompanied by suppression of vortex shedding, where the fitted magnitudes often dropped to zero. The significance of these observed relationships between suppression of vortex shedding and phase transitions is unclear, but seems likely to be connected in some way to the experiments dealing with the active control of vortex shedding conducted by Ffowcs-Williams and Zhao (1989), mentioned briefly in chapter 1, § 1.2.

The same treatment, applied to the simulated timeseries used to produce figure 6.57, produced the results shown in figure 6.61. In many ways, they are similar to those of figures 6.58–6.60, with rapid phase transitions again associated with minima, if not complete suppression of "vortex shedding", while maxima were associated with an agreement in phase between the sinusoidal signal and the timeseries composed of a scaled version of that signal and a narrow-band random process. This behaviour is not surprising, since one would expect that when the signals which made up the "force timeseries" came in phase, they would reinforce one another to produce maxima, and when they went out of phase, to produce minima.

It would seem that it is not easy to present experimental evidence which directly conflicts with the model used by Vickery and Basu, however, the physically-based argument, first advanced in § 1.6.4 and repeated at the beginning of § 6.3, suggests that the model is incorrect. The formation of vortices, deterministically related to the motion of the cylinder (perhaps similar to those observed by Williamson & Roshko 1988, see

§ 1.4.3) could produce lift forces deterministically related to cylinder motion. However, they could not remain uncorrelated with vortices formed in a random fashion (as suggested by Vickery & Basu's model), even if it were possible to create two distinct sets of vortices this way, because the two sets would interact while convecting downstream.

On this basis, the phenomena such as phase-locking described above would be accounted for by periods in which the perturbations produced by cylinder motion controlled the timing of vortex formation, while at other times this mechanism was ineffective and the process of vortex formation proceeded in much the same way as for a fixed cylinder. In other words, the phenomena can be explained by intermittent lock-in, the degree of intermittency depending on reduced velocity and oscillation amplitude. This suggests that the wake structures produced by the two mechanisms may be *topologically* incompatible, and mutually exclusive. Intermittent lock-in has been reported by both Stansby (1976) and Woo, Peterka and Cermak (1983), see § 1.4.1. Philosophically, there is a good deal of difference between this proposal and that of Vickery and Basu; how much difference in practical terms for the problem of predicting cross flow vibration response amplitudes of flexible circular-cylindrical structures is unclear.

6.6.5 3-D visualization of lift force timeseries

Since in each data recording, parallel timeseries of lift from the six transducer segments were available, it was decided to carry out some visualization to examine the three-dimensional nature of lift forces, again with the aim of understanding the lock-in process.

The visualizations to be presented were prepared with the aid of the *Mathematica* computer programme (Wolfram 1991). Prior to processing, coefficient of lift force data files were split into sub-files of 500-record-long blocks each of six subrecords (one for each transducer). Since the original data files were 8192 samples long, each file was split into 16 such sub-files which could subsequently be plotted. *Mathematica* allowed visualization by patching a series of sub-surfaces of given diffuse and specular reflectance onto the pointwise (500×6 points) coefficient of lift data. A combination of ambient and point light-sources were simulated. The overall result of the simulation was a wavy surface which could be viewed from nominated positions; the two positions used here were one directly above the surface (central along the cylinder span and midway through the timeseries) and one central in time and above the surface but displaced along the spanwise direction. In each of the figures to be presented, the first view is positioned at the top of the figure and the second in the lower part.

The first example (fig. 6.62) shows results for smooth subcritical flow with the cylinder held fixed. In the upper part of the figure, four horizontal lines of discontinuity may be seen; these represent the timeseries from the central four transducers on the cylinder; the outer two lie on the horizontal edges of the surrounding box. All the remaining surface has been interpolated by *Mathematica*. For most of the time, the lift was comparatively well-organized along the span. At about the middle of the record, it can be seen that the organization broke down, with the vortex shedding drifting out of phase along the span to the extent that lift could be positive at one end of the cylinder and negative at the other. At times near two-thirds of the duration of the record, there was a brief period in which "vortex dislocations" can be seen, with for example

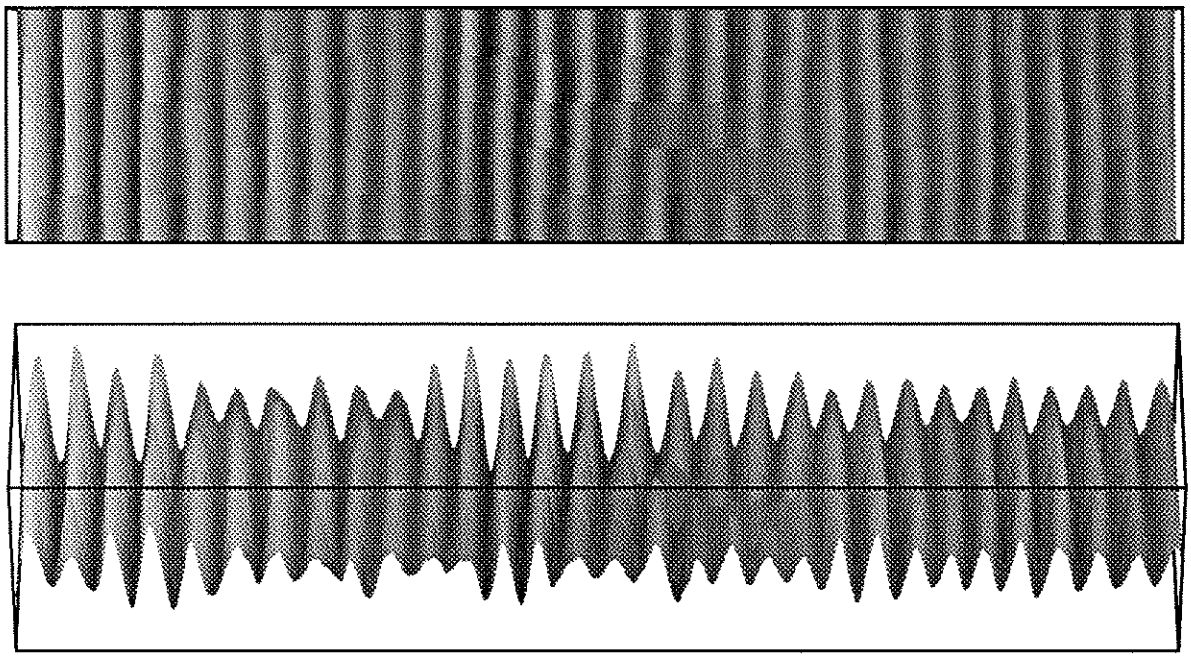

FIGURE 6.62: Visualized lift-timeseries surface; smooth subcritical flow, fixed cylinder.

comparatively strongly positive lift at one end of the cylinder, dying away to zero near mid-span, then becoming negative. In this way an "extra vortex" was produced, as may be seen most easily in the lower view of the figure: 30 peaks can be counted on the lift force trace at the side of the box furthest from the viewer, with 31 on the closer side.

The next example is for the cylinder oscillating at amplitude $\alpha_{\text{nom}} = 3\%$, at a reduced velocity of 4.72 (as for fig. 6.47(b)). In this case, lock-in was not observed, and the spectra of lift force showed two peaks. The lift-timeseries surface is shown in figure 6.63. Again, a vortex dislocation may be observed, a little before half way through the record; a count of peaks in the lower part of the figure gives 32 on the far side of the surface and 31 on the side nearer the observer. In this case, production of a vortex dislocation coincided with a rapid change in phase of lift force with respect to cylinder motion, but this was not always the case in the rest of the record; other dislocations appeared, but without a corresponding marked change in phase of lift.

The final set of results to be presented are for a flow with lock-in, at a reduced velocity of 5.02, corresponding to figure 6.47(g). During lock-in, vortex dislocations were found to be very rare, and there are none in figure 6.64. A detailed comparison of the timeseries of power transfer and lift force phase (fig. 6.59) was made with the plots of lift for this reduced velocity, but without conclusive results. Over most of the duration of figure 6.64, the average power transfer from the flow to the cylinder was positive, except at about one-third duration, where in the upper part of the figure it can be seen that the lift forces started to drift out of phase along the span, before recovering. One feature that did appear from this detailed study was that the times of high sustained power transfer (phase maintenance) and large lift forces tended to coincide with times at which the lift forces were well in-phase along the span.

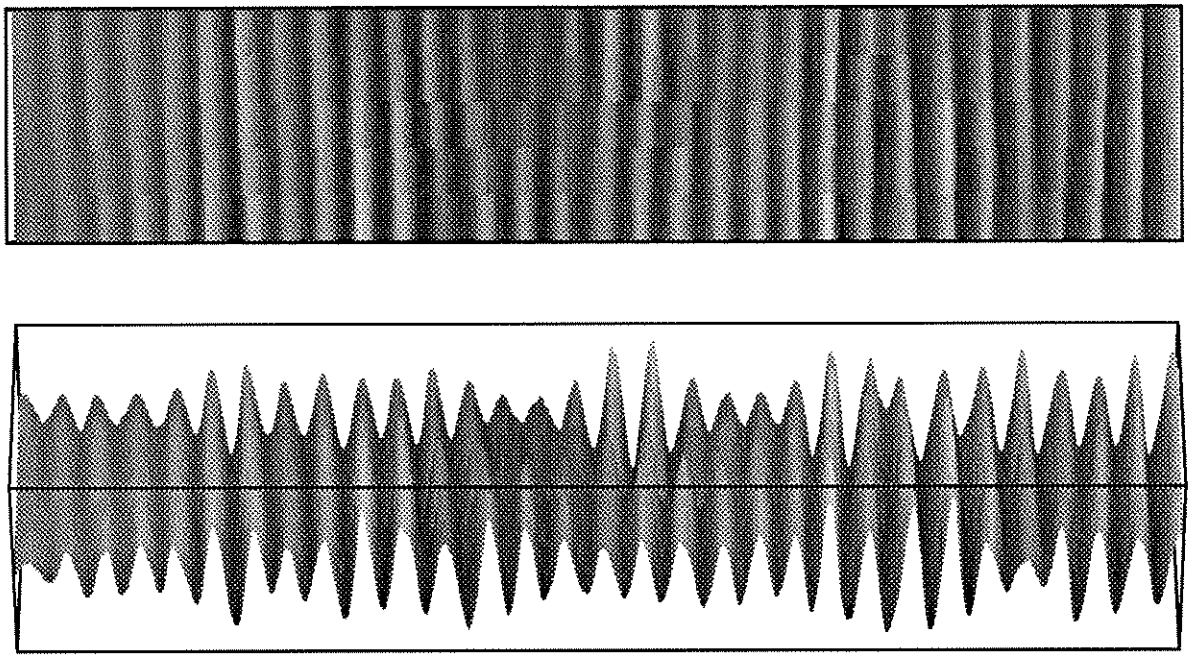

FIGURE 6.63: Visualized lift-timeseries surface; smooth subcritical flow, reduced velocity=4.72, below lock-in. $\alpha_{\text{nom}} = 3\%$.

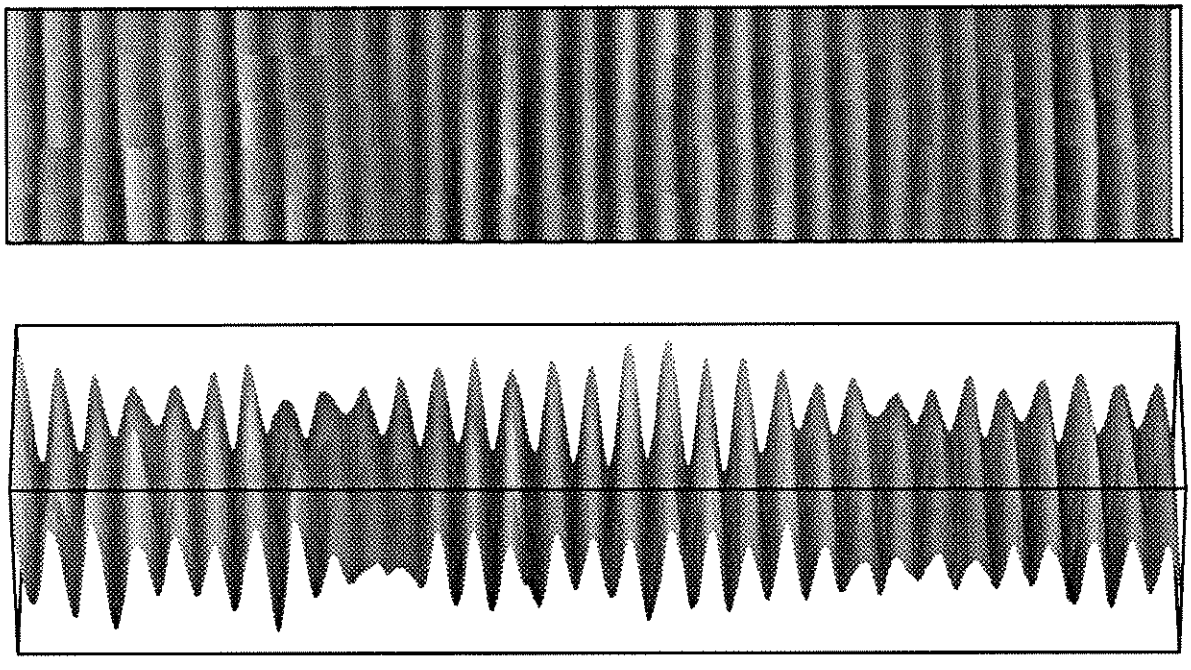

FIGURE 6.64: Visualized lift-timeseries surface; smooth subcritical flow, reduced velocity=5.02, during lock-in. $\alpha_{\text{nom}} = 3\%$.

Overall, the results of this investigation were interesting but inconclusive, and point to the need for a more fundamental examination of the fluid-mechanical processes involved, probably with the aid of flow-visualization, in a similar vein to the investigations by Ongoren and Rockwell (1988), Williamson and Roshko (1988), or the computational work by Eaton (1987), discussed in §§ 1.4.3 and 1.2.1. The work does however add to the comprehension of the three-dimensional nature of the flows and helps bring a visual interpretation to the concept of the spanwise correlation of vortices.

6.7 Conclusions

The decomposition of lift forces into motion-correlated and residual parts showed that the residual components of lift were very similar to those for the fixed cylinder presented in chapter 5. Increases in spanwise correlation of lift forces on the oscillating cylinder were shown to be accounted for by the contribution of motion-correlated forces, which were well-correlated along the span.

Before the tests were carried out, it was thought that cylinder oscillation might be able to re-establish organized vortex shedding in the low turbulence supercritical flows, at least. This possibility was suggested by Wootton (1968, 1969, as discussed in § 1.4.1), who deduced that vortex shedding, with $St \simeq 0.21$, was re-established in the supercritical regime for a smooth-surfaced stack model when tip amplitudes reached about $0.12\,D$. The lower amplitudes achieved in the current series of tests ($\alpha \simeq 3\%$) did not produce a return to organized (narrow-band) vortex shedding at supercritical Reynolds numbers ($Re \simeq 5 \times 10^5$) in any of the turbulence configurations used.

Smooth Subcritical Flow

In the smooth subcritical flow regime, motion-correlated forces were largest and showed substantial and rapid variation near the critical reduced velocity, as has been observed in previous experiments (e.g. Nakamura, Yano & Mizota 1971, Sarpkaya 1978). At the largest amplitudes of motion used (nominally 3% of diameter) and near the critical reduced velocity, motion-correlated forces formed a large proportion of the total lift in smooth subcritical flow, and values of the aerodynamic damping parameter K_a fell within the range of previous observations at similar Reynolds numbers. At the nominal motion amplitude of $3\%\,D$, motion-correlated lift reached an approximately constant value ($\sigma_{C_{l\text{correlated}}} \simeq 0.6$) over the reduced velocity range $4.79 < V_r < 5.14$. It was shown that spectra of total lift forces prepared from timeseries about 500 vortex-shedding periods in duration exhibited only single peaks at the cylinder oscillation frequency through this plateau of values of motion-correlated lift, while outside the range, two spectral peaks were observed, one centred at the cylinder oscillation frequency and one at the fixed-cylinder Strouhal frequency. On this basis, it was decided that lock-in, as defined in the conventional sense of frequency capture, also coincided with relatively constant magnitudes of motion-correlated lift forces, with only the phase of these forces with respect to cylinder motion changing with reduced velocity. Even when the centre frequency of lift force coincided with the cylinder motion frequency, the larger part of the lift was not correlated with motion on a long-time-average basis.

When velocity-correlated forces were expressed in the form of an aerodynamic damping parameter, K_a, it was found that the maximum positive value fell as amplitude of motion increased, with an extrapolated zero-amplitude value $K_{a0} = 6.5$ and $\partial K_a/\partial\alpha = -85$. Similar treatment of acceleration-correlated forces returned an extrapolated zero-amplitude maximum value of 27.5 for the coefficient of added mass, C_{a0}, and $\partial C_a/\partial\alpha = -430$. The maxima both occurred near the critical reduced velocity $V_r = 5$. It is expected that the values for the maxima were larger by a factor of approximately two than the values which would be found on a high aspect ratio cylinder in low-blockage flow, on the basis that the sectional values of σ_{C_l} reported in chapter 5 were higher than for such a cylinder. The comparatively high negative values of $\partial C_a/\partial\alpha$ and $\partial K_a/\partial\alpha$ are significant in that one of the principal models for predicting the cross flow vortex-induced vibration response of flexible circular cylinders (that of Vickery and Basu 1983 a) assumes that these parameters have value zero in the zero-amplitude limit. This suggests that their model would tend to predict higher response amplitudes as the mass-damping parameter K_s drops than would be expected on the basis of the experimental results.

A comparison of values of K_a obtained from an average of the lift timeseries from all six transducers with the average of the values of K_a obtained from each of the six transducers individually indicated that the motion-correlated forces were well-correlated along the span. This is important since it implies that observed increases in spanwise correlation of lift forces with increased amplitude of cross flow motion can be accounted for by motion-correlated forces, as proposed by Vickery (1978), Vickery and Basu (1983 a).

Detailed study of lift forces in smooth subcritical flow indicated that, even for the cases in which there was nominal lock-in, cylinder motion did not completely control the phase of vortex shedding and there were occasions on which vortex shedding unlocked from the cylinder oscillations and tended to proceed at the same frequency as for the fixed cylinder. Within the nominal lock-in boundaries, these occasions were sufficiently rare and short that they did not perceptibly influence the overall long-term average frequencies, which were the same as the cylinder oscillation frequencies. The unlocking events were associated with temporary suppression of vortex shedding. The results of this detailed study were compared with those for simulated vortex shedding forces composed of the sum of a narrow-band Gaussian process and a sinusoid, and it was found that there were many characteristics in common. The comparison was performed because of the proposal by Vickery and Basu (1983 a) that lift forces could be modelled in this way. It does not seem possible, on the basis of the data presented here, to distinguish between this description and one in which the motion-correlated forces were only intermittently present; it may be that this question can only be conclusively decided using flow visualization and examination of flow topology.

Smooth Supercritical and Turbulent Flows

For all other flow regimes, motion-correlated forces were in general smaller in magnitude and showed less variation with reduced velocity than for smooth subcritical flow. In addition, the characteristics of the variation with reduced velocity of the motion-correlated forces in turbulent flows showed little relation to those found in the smooth subcritical

flow. The acceleration-correlated forces, expressed in terms of an added-mass parameter C_a, in general remained within the range 1–2, falling as reduced velocity increased. The aerodynamic damping parameter, K_a, was smaller in magnitude and tended to increase as reduced velocity increased, but rarely exceeded values of about 0.2 and more typically was approximately 0.1. Comparison of results obtained at low and high Reynolds numbers ($Re \simeq 1.6 \times 10^5$ and 4.5×10^5 respectively) showed similar magnitudes and trends with reduced velocity, as might have been expected from the similarity over Reynolds number of the results obtained on the fixed cylinder in the turbulent flows. The results for the higher Reynolds numbers exhibited more scatter however, which is thought to be a result of increased measurement errors at higher frequencies, even though analysis of errors conducted on the basis of cancellation of transducer inertial signal obtained in the absence of flow suggested that the errors in coefficients of motion-correlated forces would be smaller at the higher Reynolds numbers.

It is probable that the results for turbulent flows obtained here cannot be directly extrapolated to values appropriate to full-scale structures, for basically the same reason as for the results obtained for the fixed cylinder in chapter 5. Although the high turbulence intensities of turbulence used were able to promote vortex shedding at comparatively low Reynolds numbers, the turbulence LSRs were smaller than those typically found in full scale ($\sim$ 0.5:1 as opposed to $\sim$ 10:1). This has two related effects which would both affect motion-correlated forces. The first is that the vortex shedding was more broad-band than would be likely to be the case at similar turbulence intensities, but higher Reynolds numbers and LSRs in full scale. It would seem that a prerequisite for interaction of vortex shedding and cylinder motion is a comparatively well-defined Strouhal frequency with narrow-band shedding. Secondly, because of the small LSRs in these experiments, turbulent velocity fluctuations at the scale of the cylinder diameter were comparatively large. These would tend to swamp any flow-boundary velocity fluctuations by which an oscillating cylinder could interact with the flow.